Exploring main group radicals using an isotope of hydrogen

by

Lalangi Asha Chandrasena

MSc., Sheffield Hallam University, 2011

BSc., University of Colombo, 2009

Thesis Submitted in Partial Fulfillment of the
Requirements for the Degree of
Doctor of Philosophy

in the
Department of Chemistry
Faculty of Science

SIMON FRASER UNIVERSITY

Fall 2019

Approval

Name:	**Lalangi Chandrasena**
Degree:	**Doctor of Philosophy (Chemistry)**
Title:	**Exploring main group radicals using an isotope of hydrogen**
Examining Committee:	**Chair: Robert Britton** Professor
	Paul Percival Senior Supervisor Professor
	Charles Walsby Supervisor Associate Professor
	Iain McKenzie Supervisor Adjunct Professor
	Jeffrey Warren Internal Examiner Associate Professor
	Stephen Mezyk External Examiner Professor Department of Chemistry and Biochemistry California State University at Long Beach
Date Defended/Approved:	October 7, 2019

Abstract

Muonium, which is considered a light isotope of the H atom, is a radioactive atom with a lifetime of 2.197 μs. Muonium adds to unsaturated molecules to form muoniated radicals. The collection of spectroscopic techniques that are used to observe muoniated radicals are known as μSR. To determine the identity of the muoniated radicals, experimental hyperfine coupling constants (hfcs) of the muoniated radicals obtained from μSR techniques were compared with hfcs of the muoniated radicals calculated using Density Functional Theory (DFT) methods available in the Gaussian 09 software package. μSR studies help us understand the reactivity of molecules towards the H atom and the configuration and conformation of the radicals formed. The polyether ether ketone (PEEK) polymer was tested for suitability in μSR sample cell fabrication. Muoniated radicals formed from monomers of PEEK, 4,4-dihydroxybenzophenone and para-dimethoxybenzene were detected. Since similar radicals expected in PEEK could interfere with sample signals it is concluded that PEEK is unsuitable for μSR sample cells. Phosphaalkene reactions with muonium were studied to understand their behaviour in radical polymerization. The model compound mesPC(Me)$_2$ was studied and two muoniated free radicals, mesP-MuC•(Me)$_2$ and mesP•-C(Mu)Me$_2$ were detected. The mesP•-C(Mu)Me$_2$ radical was compared with its isotopologue mesPH-C•(Me)CH$_2$Mu formed from mesPH(CMe=CH$_2$). A number of phosphaalkenes that differ from each other with respect to electronegativity and the bulkiness of the attached substituent groups were studied. Adamantyl phosphaalkene (AdP=CtBuH) produced only the AdMuP-C•(tBuH) radical while a sample of (CF$_3$)$_2$-mesP=C(Me)$_2$ showed muoniation at both the P and C centers of the P=C bond. Muoniated radicals formed by mesP=CPh$_2$ were identified. This helped to resolve ambiguity in identifying the initiation products of the radical polymerization pathway of mesP=CPh$_2$. The reaction of Mu with 2,4,6-tri-tert-butyl-1,3,5-triphosphosphabenzene (TPB) resulted in two muoniated radicals. Mu addition to the C atoms of the ring resulted in rearrangement to form a bicyclic product. TPB undergoes hydrogenation via a cationic route forming a bicyclic product. In this thesis I propose a radical route for this hydrogenation pathway.In summary we have utilized μSR techniques to broaden the understanding of neutral radical formation from phospha-organic compounds.

Keywords: Muonium; radical; PEEK; phosphaalkene; triphosphabenzene; DFT calculations

Dedication

For Chandra and Ananda my parents, your love and support are the guiding stars of my life.

Acknowledgements

I would like to extend my deepest gratitude to my senior supervisor, Dr. Percival for his guidance, leadership, support and patience throughout this project.

I would like to thank Dr. Brodovitch whose extensive technical knowledge helped in the detailed set up of μSR experiments in TRIUMF and his guidance on μ-LCR fits and field calibrations.

My great appreciation goes to Dr. McKenzie for his advice on μSR theory, computational calculations and for taking shifts at TRIUMF during the experiments. My sincere gratitude goes to Dr. Samedov and Dr West for their invaluable support in synthesizing and procuring the samples for this study, and without whose invaluable support this project would not have come to fruition. The advice of my committee members, Dr. Walsby and Dr. McKenzie is greatly appreciated.

Special thanks go to the Gates group in UBC for introducing me to phosphaalkenes and facilitating the synthesis of phosphaalkenes for this project. Also, to the TRIUMF facility staff for their assistance in conducting these experiments.

I would also like to thank Jim Shoults from SFU machine shop who made the μSR cells on time for the beamtime at TRIUMF.

My special thanks go to my family and my dear friends whose love and support carried me through challenging times. Without your support this work would not be possible.

Table of Contents

List of Tables

List of Figures

List of Acronyms and Symbols

ALC-μSR	Avoided Level Crossing muon spin resonance
B3LYP	Becke 3, Lee, Yang and Parr
CI	Correlation interaction
CSF	Configuration state functions
DFT	Density functional theory
e^+	Positron
e_{aq}	Hydrated electron
EPR	Electron paramagnetic resonance
hfc	Hyperfine coupling constant
HF	Hartree Fock
HOMO	Highest occupied molecular orbital
IRC	Intrinsic reaction coordinates
J-PARC	Japan Proton Accelerator Research Complex
m_{red}	Reduced mass
Mu	Muonium
μSR	Muon spin spectroscopy
NBO	Natural bonding orbital
π+	Positive pion
PEEK	Polyether ether ketone
SOMO	Singly occupied molecular orbital
TF-μSR	Transverse field muon spin rotation
THF	Tetrahydrofuran
TPB	2,4,6-tri-tert-butyl-1,3,5-triphosphabenzene
TRIUMF	Tri-University Meson Facility

Chapter 1.

Introduction

1.1. Free radicals

The modern day meaning of “radical” came to pass through a series of advances and setbacks in the field of chemistry. The term radical was first coined by Lavoisier to describe his oxygen theory of acids, where he designated the radical as elements or group of elements which combine with acids.[1] Even though the oxygen–acid theory has been discarded a long time ago, the term radical has persisted. The official beginning of free radical chemistry is usually ascribed to Gomberg’s classic research paper on triphenylmethyl radical isolation in 1900.[2]

1.2. The role of radicals

A majority of chemical processes occur through reaction pathways involving multiple reaction steps, and often these steps include radical intermediates. Hydrocarbon cracking, radical polymerization, and hydrogen transfer catalysis in hydrocarbon pyrolysis are a few economically important processes involving radical intermediates that have had a significant impact on the modern world.[3] Accordingly, it is of paramount importance that we understand these reaction steps and the intermediates involved so that we can optimize processes to our desired outcomes and predict results of new chemical processes.

1.3. Reactions of a hydrogen atom

One of the probes to study radical chemistry is the H atom. The H atom undergoes a number of well-known reactions with molecules as follows:[4]

Abstraction

$$H^{\bullet} + RX \rightarrow HX + R^{\bullet} \qquad (1.1a)$$

Electron Transfer

$$H^{\bullet} + M^{n+} \rightarrow H^{+} + M^{(n-1)+} \quad (1.1b)$$

Radical Recombination

$$H^{\bullet} + {}^{\bullet}OH \rightarrow HOH \quad (1.1c)$$

Spin Exchange

$$H^{\bullet}(\downarrow) + Ni^{\bullet}(\uparrow) \rightarrow H^{\bullet}(\uparrow) + Ni^{\bullet}(\downarrow) \quad (1.1d)$$

Addition

$$H^{\bullet} + C_6H_6 \rightarrow C_6H_7^{\bullet} \quad (1.1e)$$

The electron paramagnetic resonance (EPR) technique is frequently used to study radical structures, reaction rates, and reaction mechanisms.[5] H atoms can be generated using photolysis or radiolysis processes. However, there are major drawbacks in these methods. For example, in addition to H atoms, the radiolysis of water produces side products $^{\bullet}OH$, e_{aq}, H^{+}_{aq} and H_2. Both radiolysis and photolysis produce side products that can interfere with the EPR spectra of radicals.[6]

However, there is an alternative approach to EPR, using a collection of techniques known as muon spin rotation, relaxation and resonance, or μSR.[7] These techniques employ the positive muon, a short-lived radioactive particle. It might be helpful to give the reader a brief description of this particle before we progress in this thesis.

1.4. Muons

Muons were first observed in 1937 by Neddermeyer and Anderson, as traces left on photographic emulsion by cosmic rays.[8] Muons are generated by the interaction of cosmic rays with gas molecules in the upper atmosphere. Muons exist in both μ^+ and μ^- forms and both have a mass 1/9th that of a proton, or 207 times the mass of an electron. The μ^- can replace an electron in atoms. However, the higher mass leads to energetically low-lying atomic orbits and significantly changes the properties of the atom.[9] Therefore, we restrict our studies to the μ^+ form. For μSR experiments muons are produced as spin-polarized beams in higher intensity than cosmic muons. Only four facilities in the world have the capability to produce such high-intensity beams, namely

TRIUMF (Canada), Paul Scherrer Institute (Switzerland), ISIS (UK), and J-PARC (Japan). In these facilities a high-energy beam of protons is directed to a pion producing target such as beryllium or carbon. The energy of the beam must be higher than the rest mass of the pion (139.6 MeV/c^2) and the result is emission of pions. The pions are filtered using a dipole magnet to select the desired charge and momentum.

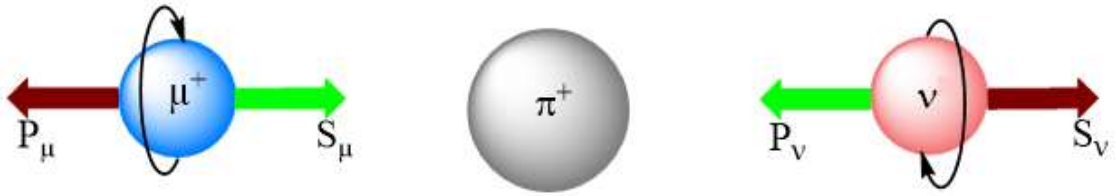

Figure 1-1: Pion decay to form a muon and a neutrino. P_μ, P_ν, S_μ and S_ν indicate the muon and neutrino momenta and their spins.

A positive pion (π^+), has a short lifetime of 26 ns and decays to a positive muon (μ^+) and a muon neutrino (ν). Muons produced by the decay of pions resting on the surface layer of the production target are known as surface muons and are positively charged, and are most frequently used for the spectroscopic techniques. The pion's decay is parity-violating, hence producing muons with momentum anti-parallel to their spin polarization. In the case of surface muons, the polarization is 100%. This gives a significant advantage for μSR techniques over the conventional magnetic resonance techniques, as the μ^+ ensemble's polarization is independent of temperature and magnetic field. This gives a many magnitude larger polarization than conventional techniques and gives the unique capacity to do experiments in lower temperatures and zero magnetic fields. Furthermore, the conventional techniques like NMR or EPR require high frequency electromagnetic radiation (RF or microwave) to create the spin coherence while μSR does not; hence this provides a higher resolution in μSR.[7]

The muon has a short lifetime (2.197134 μs) and undergoes radioactive decay (equations. 1.2, 1.3). Moreover, decay positrons are emitted preferentially along the muon spin direction due to the parity-violating decay. As a result, this provides a convenient way to detect the muon spin direction. The neutrinos are not detected.

$$\mu^+ \rightarrow e^+ + \nu_e + \bar{\nu}_\mu \qquad (1.2)$$

$$\mu^- \rightarrow e^- + \bar{\nu}_e + \nu_\mu \qquad (1.3)$$

1.5. Muons in diamagnetic environment

Muons from a beam are highly versatile and can be embedded in solid, liquid or gas phases. Once inside the sample high-energy muons will undergo rapid thermalization. During this process the polarization of the muon ensemble is conserved. The majority of these muons are incorporated in molecules to produce diamagnetic species. This fraction of muons is collectively known as the diamagnetic muon fraction. Due to the short lifetime of the muon, the highest spectral resolution of muon spectrometers is limited, hence it is not possible to resolve chemical shifts and differentiate between different diamagnetic species.[7]

In molecular gases or liquids, the muon can attract an electron to form a paramagnetic state of the muon known as muonium (Mu). Muonium was first observed by Hughes et al. in 1960,[10] and subsequently in 1963, Brodskii proposed the idea of a muoniated radical species formed using the paramagnetic Mu atom.[11]

1.6. Muonium

The muonium atom, consisting of a muon nucleus and an electron, has a mass of 1/9th of a hydrogen atom. However, the reduced mass of muonium is similar to the reduced mass of a H atom (eq 1.4) and its Bohr radius and ionization potential are within 0.5% of those of the H atom.[12]

$$\frac{1}{m_{\mathrm{red}}} = \frac{1}{m_{\mu}} + \frac{1}{m_{\mathrm{e}}} \simeq \frac{1}{m_{\mathrm{e}}} \qquad (1.4)$$

As a result, the muonium atom behaves chemically as an isotope of the H atom, similar to D and T (table 1-1). Unlike D and T, Mu rapidly decays due to the short muon lifetime and hence is not suitable for stable molecule synthesis. It is a valuable alternative for the study of short-lived radicals. In 1978 the muonium atom made its debut in the area of radical chemistry, with the first observation of an organic radical incorporating muonium.[13]

So why are scientists using this exotic isotope as an H atom substitute? Even though an unconventional option, muon spin spectroscopy (μSR) presents several advantages over conventional techniques.

Table 1-1: Comparison of the properties of hydrogen isotopes

Properties	Isotope			
	H	Muonium (Mu)	Deuterium (D)	Tritium (T)
Mass ratio: (mass/m_H)	1.0000	0.1131	1.9980	2.9930
Reduced mass: (m_r/m_e)	0.9995	0.9952	0.9997	0.9998
Bohr radius (pm)	52.92	53.15	52.90	52.90

In μSR Mu atoms are generated inside the test sample without the complications of multiple by-products typical of EPR methods. Thus, the radical spectra generated by μSR techniques are less complex. In μSR only a few muoniated radicals are present in the sample at a given time and hence the ensuing reactions follow pseudo first-order kinetics, facilitating the study of reaction kinetics. The Mu atom's short lifetime guarantees that the observed muoniated radicals are predominantly primary radicals. Hence, this makes μSR an ideal tool to study transient radicals and the radical initiation steps in polymerization reactions that are too difficult to monitor using EPR and NMR.[12,14]

In addition, Mu presents an excellent opportunity to study isotope effects in H isotopes. We can approximate a bond between two atoms to a harmonic oscillator and the vibrational energy levels can be determined from equation (1.5)

$$E = h\nu(n + \frac{1}{2}) \tag{1.5}$$

where h is the Planck constant, v is the vibrational frequency and = 0, 1, 2…n is the vibrational quantum number. We can determine the vibrational frequency via equation (1.6).

$$\nu = \frac{1}{2\pi}\sqrt{\frac{k}{m_{red}}} \tag{1.6}$$

where k is the force constant of the bond and m_{red} is the reduced mass. Compared to a bond between the H atom and a heavy atom to a bond between Mu and a heavy atom, the reduced mass of the latter will be 1/9th of the diatomic system with the H atom. Therefore, the vibrational frequency with Mu should be 3 times that for the H atom.[3] In addition to being the light isotope of the H atom Mu's unique nature has contributed to

ground-breaking research which would have otherwise not been possible. For example, experimental proof of the existence of vibrational bonding was discovered using Mu in 2014,[15] something previously only theorized as a quantum-mechanical phenomenon.

1.7. Muonium in a magnetic field

The muonium atom consists of two spin ½ particles. The spin Hamiltonian of this system is described by equation (1.7) as follows[14]

$$\hat{H} = \omega_e \hat{S}_z^e - \omega_\mu \hat{I}_z^\mu + \omega_0 \hat{S}_z^e . \hat{I}_z^\mu \tag{1.7}$$

where ω_e and ω_μ are electron and muon Zeeman angular frequencies and $\hat{S}_z^e$ and $\hat{I}_z^\mu$ are electron and muon spin operators, respectively. ω_0 is the muon hyperfine coupling constant (hfc) in angular frequency units. The isotropic muon hfc is directly proportional to the unpaired electron density on the muon nucleus (the Fermi contact interaction). Therefore, with any changes in the local molecular environment the unpaired electron density on the muon nucleus changes and results in changes in muon hfc. Conventionally in μSR, muon hfcs are reported in frequency units and ω_0 values are converted to MHz using the equation

$$A_\mu / \mathrm{MHz} = \frac{\omega_0}{2\pi} \times 10^{-6} \mathrm{s}^{-1} \tag{1.8}$$

There are four eigenstates resulting from a two-spin system:

$$|1\rangle = |\alpha_\mu \alpha_e\rangle \tag{1.9}$$

$$|2\rangle = s|\alpha_\mu \beta_e\rangle + c|\beta_\mu \alpha_e\rangle \tag{1.10}$$

$$|3\rangle = |\beta_\mu \beta_e\rangle \tag{1.11}$$

$$|4\rangle = c|\alpha_\mu \beta_e\rangle - s|\beta_\mu \alpha_e\rangle \tag{1.12}$$

where constants c and s are defined as

$$c = \frac{1}{\sqrt{2}}\left[1 + \frac{x}{\sqrt{1+x^2}}\right]^{\frac{1}{2}} \tag{1.13}$$

$$s = \frac{1}{\sqrt{2}}\left[1 - \frac{x}{\sqrt{1+x^2}}\right]^{\frac{1}{2}} \tag{1.14}$$

and x is defined as $x = \frac{\omega_e + \omega_\mu}{\omega_0}$

Applying the spin Hamiltonian to these eigenstates gives the energy levels

$$E_1 = \frac{1}{4}\omega_0 + \omega_- \tag{1.15}$$

$$E_2 = \frac{1}{4}\omega_0 + \left[\omega_+^2 + \frac{1}{4}\omega_0^2\right]^{\frac{1}{2}} \tag{1.16}$$

$$E_3 = \frac{1}{4}\omega_0 - \omega_- \tag{1.17}$$

$$E_4 = -\frac{1}{4}\omega_0 - \left[\omega_+^2 + \frac{1}{4}\omega_0^2\right]^{\frac{1}{2}} \tag{1.18}$$

where $$\omega_\pm = \frac{\omega_e \pm \omega_\mu}{2} \tag{1.19}$$

The transitions between these energy levels are governed by the selection rules $\Delta m_\mu = \pm 1$ and $\Delta m_s = 0$ hence there are four allowed transitions

$$\omega_{12} = \omega_- - \Omega_+ \tag{1.20}$$

$$\omega_{23} = \omega_- + \Omega \tag{1.21}$$

$$\omega_{14} = \omega_- + \Omega + \omega_0 \tag{1.22}$$

$$\omega_{43} = \omega_{-} - \Omega - \omega_0 \tag{1.23}$$

Energy level E_4 is well separated from the rest of the energy levels due to the large ω_0. Hence, the ω_{14} and ω_{43} transitions have a larger energy gap and the transitions are in the range of 2.8×10^{10} rad s^{-1}. Therefore, signals due to these transitions cannot be resolved by μSR instruments with detector response times typically 2 ns.**Error! Reference source not found.**

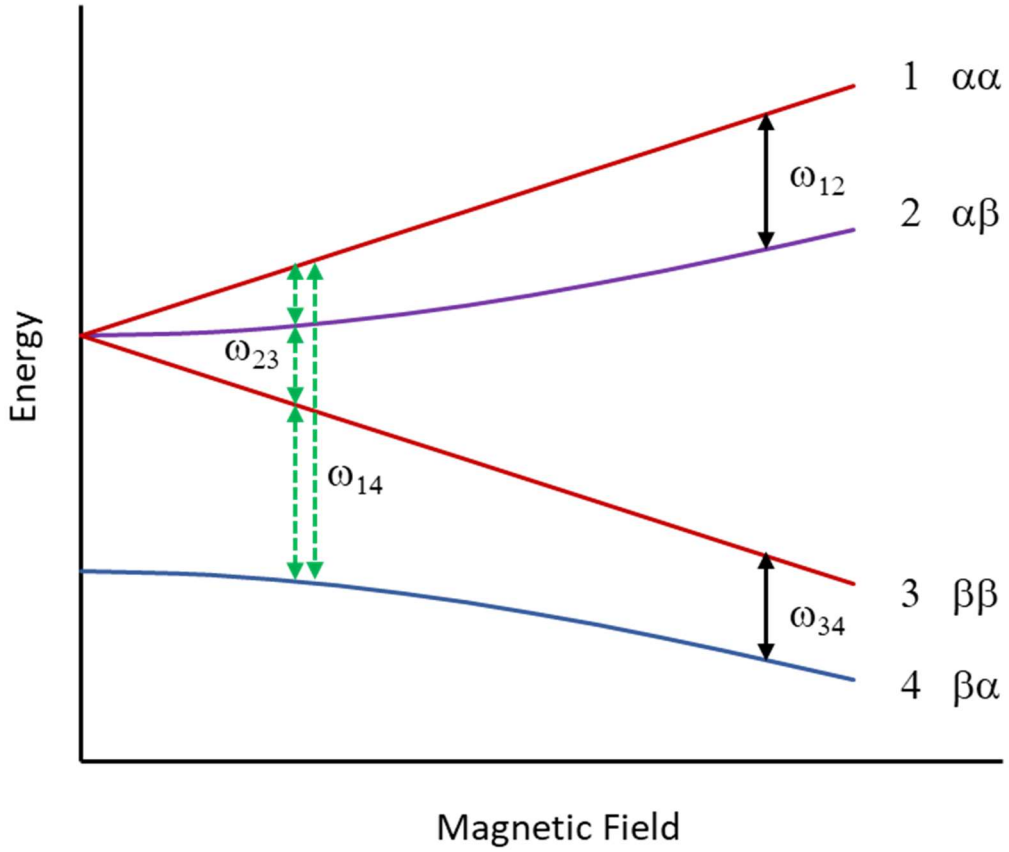

Figure 1-2: Breit-Rabi diagram of the muonium two spin-1/2 system. The solid vertical lines indicate the allowed transitions in high transverse field. The green dotted lines are the transitions allowed at low field.

At lower magnetic field the isotropic Fermi contact dominates and $\omega_0 >> \omega_e, \omega_\mu$. Therefore, ω_{12} and ω_{23} become degenerate and can be approximated by

$$\omega_{12} = \omega_{23} = \frac{\omega_e - \omega_\mu}{2} \tag{1.24}$$

Increasing magnetic field lifts the degeneracy of the ω_{12} and ω_{23} transitions.

The muonium atom exists in a singlet and a triplet form in the absence of a magnetic field. When the muonium atom is placed in a transverse magnetic field both the muon and the electron spin interact with the external magnetic field and the triplet muonium state is split into three energy levels, creating a total of four energy levels as shown in the Breit-Rabi diagram in figure 1-2.

1.8. Muoniated radicals in a magnetic field

Muonium, being a light isotope of hydrogen, is a highly reactive neutral atom. When injected into samples containing unsaturated molecules the Mu atom reacts with these molecules to produce muoniated radicals. Inside the muoniated radical the unpaired electron density on the muon nucleus is determined by the molecular orbitals, which are determined by the structure and the dynamics of the radical molecule. The spins of the muon and other spin active nuclei each interact with the unpaired electron through respective hyperfine interactions (figure 1.3).

The spin Hamiltonian of the radical system is given by[14]

$$\hat{H} = \omega_e \hat{S}_z^e - \omega_\mu \hat{I}_z^\mu + \omega_0^\mu S \cdot \hat{I}^\mu - \sum \omega_k \hat{I}_z^k + \sum \omega_0^k \cdot \hat{S}_z^e \cdot \hat{I}^k \qquad (1.25)$$

where ω_e, ω_μ and ω_k are Zeeman angular frequencies of the electron, the muon and the spin-active nuclei *k*. The isotropic Fermi contact coupling constants of the muon and other nuclei are ω_0^μ and ω_0^k.

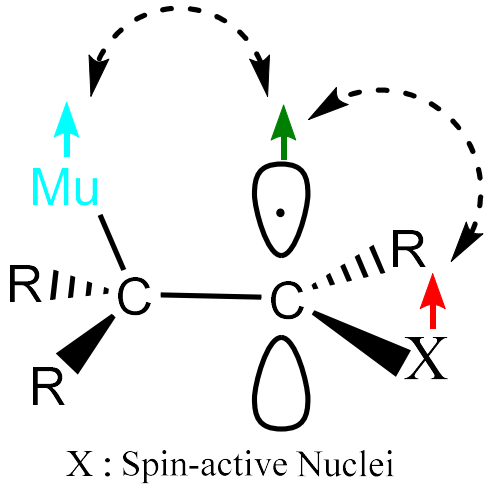

Figure 1-3: Interaction of the unpaired electron with the muon and another spin-active nucleus in a muoniated radical.

A number N of nuclei in the system with spin quantum number I_k results in $4\prod_k(2I_k+1)$ eigenstates. Therefore, the muon polarization will be distributed between multiple frequencies and at low and mid fields detection of muoniated radicals is not feasible. However, at larger magnetic field the electron Zeeman frequency dominates, satisfying the condition $\omega_e >> \omega_0^{\mu}, \omega_0^{k}$. This significantly simplifies the energy levels and creates two degenerate groups of transitions with ω_{12} and ω_{34}.[17]

1.9. Muoniated radicals in a longitudinal magnetic field

An alternative technique makes use of a longitudinal field. When muons are injected into a sample with their muon polarization parallel to the external magnetic field, muoniated radicals are formed in pure Zeeman states; hence there is no precession of the muon spin with time. The muon nuclei undergo radioactive decay and positrons are emitted preferentially along the muon spin direction. The total number of positrons emitted along the spin directions are counted by two detectors in the forward (F) and backward directions (B) with respect to the external magnetic field.

When considering a muoniated radical containing a three-spin system (muon, electron and one other spin-active nucleus) at high magnetic field, different spin states can have near degenerate energies leading to mixing of the states. The importance of this situation was recognized by Abragam[18] in 1984 and led to the development of avoided level-crossing muon spin spectroscopy (ALC-μSR).[19,20]

In these near degenerate states muon polarization can oscillate between two mixing energy levels leading to a resonance-like signal in the muon polarization curve. The muon polarization is proportional to the experimental asymmetry (A), which is given by the normalized difference of positron counts in forward and backward detectors:

$$A = \frac{(N_B - N_F)}{(N_B + N_F)} \tag{1.26}$$

According to the selection rules there are three types of allowed transitions for these resonances. The selection rules are $\Delta M = 0,1,2$, where ΔM is the change in the sum of

the quantum numbers of muon and nuclear spin *z*-components. The transitions that occur are respectively known as Δ_0, Δ_1 and Δ_2 according to the quantum number. The Δ_2 transitions are quite weak and seldom observed. The Δ_1 transitions occur due to anisotropic interactions and are observed in solids and other situations where there is slow reorientation.[21]

The Δ_0 transition, which is crucial to our studies, is observed for muoniated radicals in solid, liquid and gas states.[22] This transition, also known as the muon-nucleus spin flip-flop transition, happens between spin states having the same electron spin but opposite muon and nuclear spins. For each spin-active nucleus at a specific magnetic field the spin states are near degenerate and mixing leads to muon polarization oscillation between the two states, resulting in a resonance-like change in muon polarization. In principle all the spin-active nuclei in the vicinity of the muon nucleus give rise to a Δ_0 resonance but the resonance amplitude can be negligibly small for small hfcs. This resonance is used to measure the hfcs of spin-active nuclei and is vital in muoniated radical characterization. The hfc of spin-active nucleus can be calculated using

$$B_{\mathrm{res}}^{\Delta_0} = \frac{1}{2}\left[\frac{A_\mu - A_x}{\gamma_\mu - \gamma_x} - \frac{A_\mu + A_x}{\gamma_e}\right] \qquad (1.27)$$

where B_{res} is the magnetic field at resonance, γ_μ , γ_e , γ_k are gyromagnetic ratios, and A_μ and A_k are muon and nuclear hfcs, respectively.[22]

1.10. Study of muoniated radicals of main group elements

Since the initial development of μSR it has been used in the study of main group element chemistry. Even though it is a somewhat more exotic technique compared to routinely used techniques such as EPR, μSR has provided a wealth of information on the conformation, configuration, intramolecular motion and kinetics of alkyl and aromatic radicals. In addition, μSR provides information that cannot be obtained by conventional methods and under extreme conditions that cannot be accessed with conventional spectroscopic methods. A majority of the radicals observed are β-muoniated radicals where Mu is attached to the β position of the SOMO.[23]

The compounds extensively studied by this technique were simple organic molecules such as alkenes, alkynes and aromatic compounds. The initial comprehensive study of β-muoniated radicals was done by Roduner et al. on alkenes.[24] In this study 44 muoniated radicals were generated from olefins and conjugated dienes. Detection of the simplest β-muoniated radical (muoniated ethyl radical) by Ramos et al.[25] complemented existing data obtained by EPR methods. A study done by Percival et al.[26] on the muoniated *tert*-butyl radical established that the muon hfc is the average of muon hfcs of multiple conformations of muoniated radical rotation around the C-C backbone. The muon hfcs of ethyl and *tert*-butyl muoniated radicals were found to fall with temperature, the opposite to the trend observed for proton hfcs. Yu et al. pioneered the study of the muoniated cyclohexadienyl radical (figure 1-4).[27] The study shows that, unlike the previously held idea of ring distortion, the negative temperature gradient measured for both proton and muon hfcs is due to bending modes in the methylene group.[27]

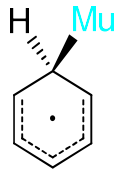

Figure 1-4: Muoniated cyclohexadienyl

α-muoniated radicals are not as prevalent as their β-muoniated counterparts.[28] The smallest α-muoniated methyl radical was formed by McKenzie et al. in 2007,[2929] by muonium addition to ketene followed by rapid decomposition of the intermediate acyl radical. This study gave insight into the temperature dependence of the methyl radical hfcs and the effect of isotopic substitution. A notable study by McKenzie et al. in 2003 reported the muonium adduct of an ylidene, its geometry, spin distribution and hfcs.[30] This shed light on the radical chemistry of the Arduengo carbene, which plays a vital role as a stable ligand in transition metal chemistry.[31] The successful use of μSR in the study of carbon-based compounds prompted the investigation of the radical chemistry of other main group elements.[32-34]

A collaboration of the Percival group at SFU and Robert West's group at the University of Wisconsin investigated stable silylenes and germylenes using μSR.[35]

Silylenes and germylenes are carbene analogues and react with muonium to form muoniated radicals. Both families of compounds are highly important in synthetic chemistry as intermediates in numerous reactions and ligands with catalytic properties. However, there was a lack of information on their radical properties before the above-mentioned studies were conducted. The study of silylenes led to the discovery of the disilanyl radical formed by fast coupling reactions.[36] This had never previously been observed via conventional spectroscopic techniques. This highlights the capability of μSR to identify unique reactions that are not observable by conventional methods. In addition, silene compounds (Si=C) have been studied by μSR and the corresponding muoniated radical structures and hfc constants have been determined.[37]

An example of utilizing μSR in conditions that are not compatible with conventional techniques is the study by Percival et al. of muoniated radicals in superheated water.[38] This study characterized the behaviour of transient radicals under hydrothermal conditions. There are multiple industries concerned with chemistry under hydrothermal conditions, e.g., corrosion of pressurized water in nuclear reactors, geochemical production of fossil fuels and biology of sub-marine volcanic vents.[39]

Therefore, with the application of μSR, a new frontier in the study of main group radical chemistry has opened. We have the opportunity to study the radical chemistry of multiple-bonded and unsaturated compounds of main group elements B, N, P, S, As, Sn etc. Hence our study on the radical chemistry of multiple-bonded organophosphorus compounds came to fruition.

1.11. New adventures in low-valent organophosphorus chemistry

"Phosphorus Remains Exciting!"[38]

Recent studies of phosphorus compounds are focused on the synthesis and utilization of the low-valent P species.[40] P is a multifaceted element that mimics the chemistry of N or C according to the oxidation state it exists in. Low-oxidation states of organophosphorus compounds mimic the chemistry of their organic counterparts hence the expression "P the carbon copy" was coined.[40-42] We can illustrate the phosphorus–carbon analogy by replacing the CR_2 fragment with the isolobal P-R moiety. The most

common low-valent organophosphorus groups produced by replacing CR_2 by P-H groups are illustrated in figure 1-5.

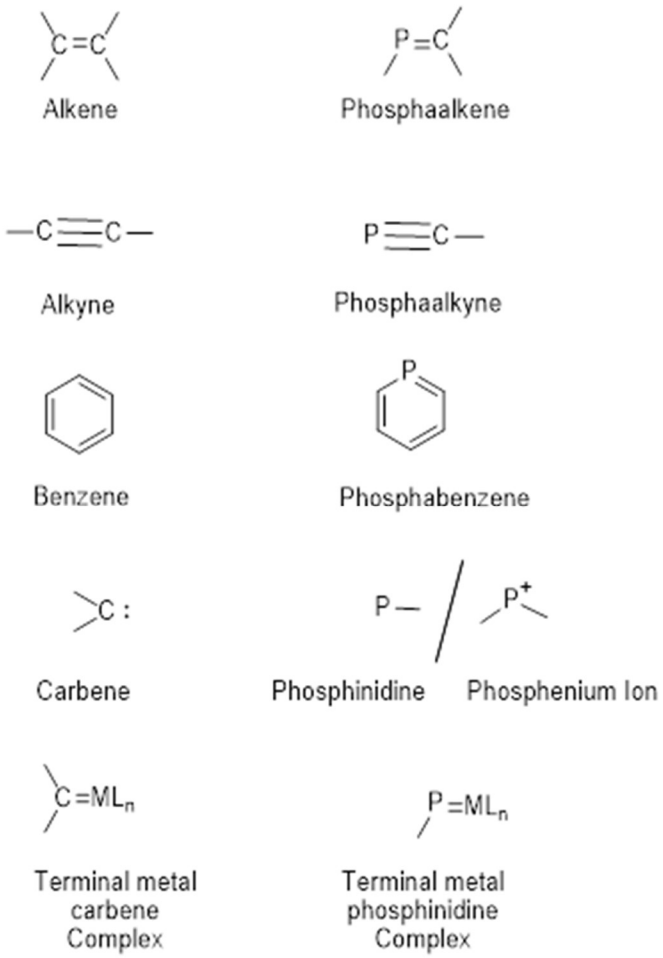

Figure 1-5: Organic compounds and their organophosphorus counterparts

Initially, just as the octet rule had hindered the discovery of inert gas compounds, the double bond rule (the principle that elements in the rows below carbon do not form multiple bonds with themselves or each other) has resulted in scientists overlooking many organo P and N compounds with multiple (p-p) π bonds. An experiment carried out by Gier in 1961,[43] where he pyrolyzed PH_3 gas on rotating graphite electrodes, led to the first synthesis of phosphaacetylene.[42] The compound is pyrophoric and readily decomposes in temperatures above -124 °C. Since then low-valent phospha-organic chemistry has been a dynamic field with the discovery of new compounds and applications ranging from polymers, ligands, diodes and biomedical devices.[40]

The most common low-valent P compounds have an oxidation state of (+3), and the most widely utilized compound groups are phosphines, phosphaalkenes, phosphaalkynes and aromatic phosphinines. These compound groups are also often referred to by their valence (λ) and coordination number (σ) hence it is useful to be familiar with the convention, as illustrated by the following:

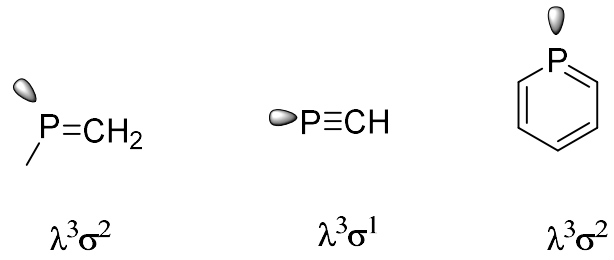

Figure 1-6: Low-valent organophosphorus nomenclature

For our investigation we focused on two groups of low-valent organophosphorus compounds: phosphaalkenes and phosphinines. In organic chemistry the C=C double bond has been one of the most common functional groups, with numerous applications in industrial settings. Similarly, the P=C double bond recently led to compounds with industrial applications and still presents the potential for exciting future endeavors.[40,41]

1.12. P=C bond the 'carbon's copy'

It is important to understand how a P=C double bond can have similar properties to a C=C bond. The P=C double bond is in the $\lambda^3\sigma^2$ state. However, the P atom is reluctant to undergo sp^2 or sp hybridization due to partial mixing of 3*s* and 3*p* orbitals. Therefore, unlike the sp^2 hybridized orbitals of C atoms which are 120° apart from each other, P sp^2 orbitals have an angle of 100° between them and the lone pair on the P atom features high *s* character (66%) compared to *p* character (34%).[40] Also, the lone pair orbital is not very high in energy; on the other hand in the imines N atom lone pair shows inverted orbital distribution and act as the HOMO in the molecule. Therefore, imines show reactions centered on the N lone pair, whereas in P=C bonded compounds the HOMO is the π system similar to C=C bonded systems. Accordingly it shows reactions centric to π bonds.[40]

The electronegativity of the P=C bond is the next key difference that leads to the P=C bond's behavior. According to the Pauling electronegativity scale a P atom is 2.1

and a C atom is 2.5 hence making P more electropositive. Consequently, the P=C bond acts as both a σ donor and a π acceptor, making the P=C bond essentially apolar.[42]

Even with these parallels between the P=C bond and the C=C bond, the P=C π bond strength is significantly lower compared to C=C bonds. Therefore, phosphaalkene species need significant kinetic or thermodynamic stabilization to exist at room temperature. Usually the stability of phosphaalkenes is achieved by encumbering the P atom with sterically bulky substituents such as mesityl (2,4,6-trimethylphenyl) or *mes** (2,4,6-tris-*t*-butyl-phenyl). In addition, the P=C bond can be thermodynamically stabilized by delocalizing the π system. For example, phosphabenzene, a phosphinine analog of benzene which has similar aromaticity[44] is air stable even as a liquid.

1.13. Importance of the study

The motivation for this study comes from the rapid advancement of organophosphorus chemistry. Structural and electromagnetic properties of low-valent organo-phosphorus compounds are used for there application as conductive polymers, catalytic polymer layers, in organometallic chemistry emmisive materials for OLEDs. The low-valent organo-phosphorus species such as phospholes are already thoroughly studied. However, studies on the P=C bond are still at the developing stage and there is only minor information available on P=C radical chemistry. The most important applications of P=C bonds thus far are in polymerization, their catalytic properties, and their use as ligands.[40]

Aromatic phosphinine compounds can act as ligands for many organometallic compounds, and recently some derivatives of phosphinines have been discovered to have the ability to cleave small molecules such as H_2 without transition metal catalysts.[44] Consequently, we need to study the radical chemistry of these molecules to fully understand their characteristics, to discover potential new reaction pathways, and to simply quench our scientific curiosity.

One of the most common modes of polymerization of phosphaalkenes is through radical initiation. However, with a complex mixture of starting materials EPR and NMR spectra are too complicated to discern the radical initiation step. A P=C double bond is

highly reactive and forms muoniated radicals. Therefore, the alternative of studying the radical chemistry of the P=C bond by μSR is both timely and essential.

In summary, in this thesis we are on a quest to understand the muoniated radical formation radical conformation, configuration, and novel reaction pathways involving muoniated radicals. Primarily we have focused on the P=C bond.

Chapter 2.

Methodology

2.1. Conducting μSR experiments at TRIUMF

TRIUMF (Tri-University Meson Facility) is the Canadian particle accelerator center. TRIUMF was founded in 1968 as a joint project by the University of British Columbia (UBC), Simon Fraser University (SFU) and University of Victoria. The University of Alberta soon joined, and today the TRIUMF consortium includes 20 member and associate member Canadian universities.[45]

The facility houses a large, six-sector, isochronous cyclotron which is fundamental to nuclear physics, particle-physics and material-science experiments. In the cyclotron H^- ions can be accelerated up to 520 MeV. In order to extract a high energy proton beam the H^- ions are directed through a carbon foil which strips off two electrons while the much heavier protons are passed through. TRIUMF is capable of simultaneous extraction of multiple high energy proton beam channels.[46]

Presently there are four proton beam lines, known as 1A, 1B, 2A and 2C. They deliver protons with different energies. The high energy beam line 1A supplies protons to targets known as T1 and T2. Target T1 is used for experimental channel M15 while T2 serves the M9B and M20 channels. Beamline 1B provides protons to the Proton Irradiation Facility (PIF) that is used for radiation testing of electronic circuits etc. These channels are used for fundamental research on materials chemistry and particle physics. Beamline 2A supplies beam to the Isotope Separator and Accelerator (ISAC) facility for the production of rare isotopes. Meanwhile, beamline 2C is used for proton therapy to treat choroidal melanomas (eye tumors) and to produce strontium isotopes.[47]

Currently, TRIUMF hosts a wide variety of research programs in nuclear physics, particle physics, materials science, and life sciences. Researchers use the facility for programs approved by a scientific evaluation committee in blocks of time. For our experiments, we used the M15 and M20 muon beams.

2.1.1. Muon beams

There are three types of muon beams produced by the production targets: forward muons, backward muons and surface muons.[9] The forward and backward muons are produced by pions that decay in flight. The forward muons are highest in energy, have a high stopping range, and are no longer used for μSR experiments.

Backward muons have momentum opposite in direction to the pion momentum. They are ideal for experiments that require penetration of a thick target, such as a pressure cell, e.g. the SFUMU group experiments on radical characterization in supercritical water.

In the M15 and M20 channels a third type of muon known as surface muons are produced. Surface muons are created from pions that decay on the surface of the pion production target, hence the name.[48] Since the pions decay on the surface muons are emitted isotropically with 29.8 MeV and 4.19 MeV kinetic energy. Because of the low kinetic energy surface muons have a stopping range approximately 160 mg/cm^2. Therefore, they can be used for the study of liquids and gases in cells with thin windows. In addition, surface muons have almost 100% spin polarization Most of the studies conducted for this project were done using surface muons from the M15 beamline.

2.1.2. M15 beam channel

The M15 beam channel is dedicated for surface muons produced at the T1 target. The T1 target is made of 1 cm thick graphite and once the proton beam hits the target pions are created and decay into muons. A quadrupole doublet located near the T1 target selects a narrow range of momentum before the beam reaches the spin rotators. Collected muons are then directed through the M15 beam line to dual spin rotators known as Wien filters which simultaneously filter out positrons in the beam and rotate the muon spin perpendicular to the beam direction.[49]

2.1.3. Sample cells and temperature control

The phosphaalkene samples and phosphinine samples were either solids or liquids. The solid samples were dissolved in organic solvents to concentrations between 0.1 M and 1.0 M. Except for the phosphinine samples, which were dissolved in hexane and 4,4ʻ-dihydroxybenzophenone which was dissolved in ethanol, all other samples in this study were dissolved in tetrahydrofuran (THF). The solvents were HPLC grade and double distilled to remove moisture and impurities. Phosphaorganic samples are oxygen sensitive, so samples were encapsulated in an inert environment in a glove box.

Samples were encapsulated in stainless-steel cells with a capacity of 1.5 ml. Small cylindrical disk-shaped sample cells were used. One side of the disk consists of a thin stainless-steel foil which allows the penetration of the surface muons. To the opposite side of the membrane at the center, there is an opening with a metal screw plug or glass tube, for introduction of the sample. Glass stem cells can be connected to a vacuum line so that the liquid sample can be subjected to several freeze pump thaw (FTP) cycles to remove dissolved air prior to flame sealing the glass stem.

The experiments in this research were done in a temperature-controlled environment with temperatures ranging from -5 °C to 50 °C and the temperature was controlled by a Thermo Haake circulator with a temperature range of -40 °C to 200 °C.

2.1.4. The μSR spectrometer

Our experiments are done using the Helios spectrometer at TRIUMF.[45] Helios contains a superconducting magnet that can provide fields up to 70 kG. For this project, μSR experiments were done in the 0 to 20 kG range.

Muons and positrons were detected by plastic scintillators. When a particle passes through a detector it produces a light pulse that falls on the photomultiplier tube which converts it into an electronic pulse. The signal is recorded by electronics in the counting room.

To calibrate the magnet, a series of short transverse field μSR runs were done covering the entire experimental magnetic range. The diamagnetic signal is measured for these varying fields. The diamagnetic frequency is related to the magnetic field by

$$\nu_D = \gamma_\mu B \qquad (2.1)$$

where ν_D is the diamagnetic frequency and γ_μ the gyromagnetic ratio. The muon precession frequency is determined for each magnetic field setting (magnet current) and the calculated field plotted against current setting to create a calibration curve.

2.1.5. Transverse field muon spin spectroscopy (TF-μSR)[7]

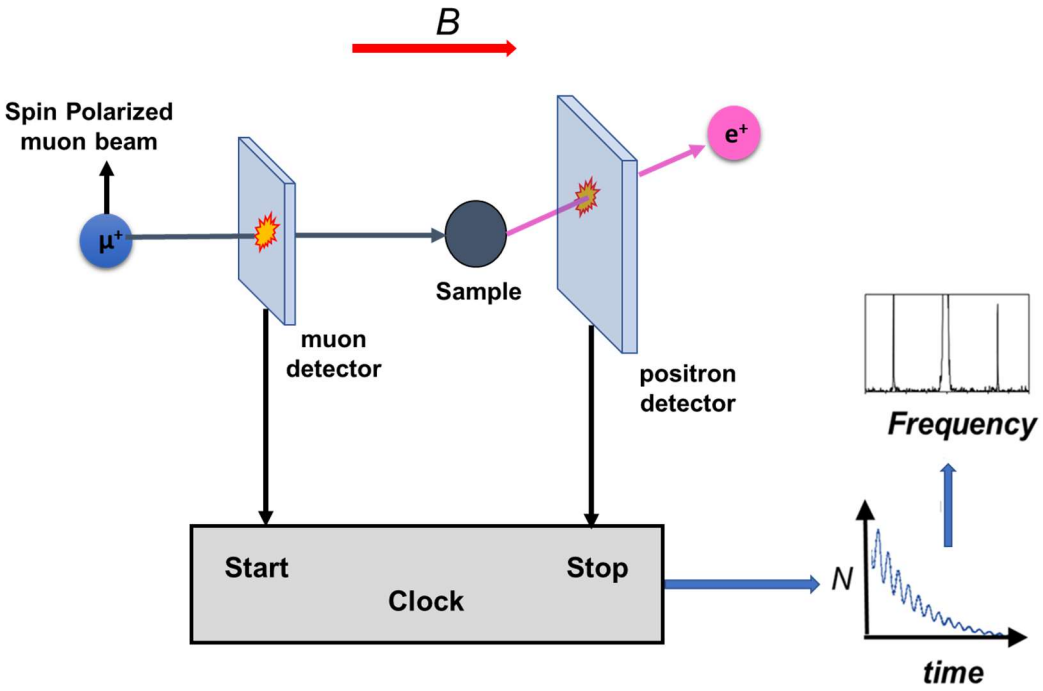

Figure 2-1: A Schematic diagram of a TF-μSR apparatus. Only one positron detector is shown. The direction of the magnetic field is perpendicular to the muon polarization and indicated by the red arrow.

The muon beam enters the TF-μSR spectrometer through a muon scintillator detector. This generates a signal that triggers the start of a digital clock (figure 2-1). The muons stop in the sample where they decay to give positrons. There are four positron detectors that are arranged in phase quadrature. They are known as, Left Up (LU), Right Up (RU), Right Down (RD) and Left Down (LD). When a decay positron is detected by one of the counters a signal is sent to the clock to end the data collection window (data gate). The elapsed time between the start and stop signals is recorded as an event and stored in a bin of a histogram for the corresponding counter. However, absolute correlation between the counted muon and the positron is necessary because

if another muon enters the system while the data gate is open the positron cannot be unambiguously assigned to a particular muon and the event has to be discarded. This occurrence is known as pileup. Multiple muons or multiple positrons within a data gate result in rejection of that event.

2.1.6. Avoided Level crossing muon spin spectroscopy (ALC-μSR)[7]

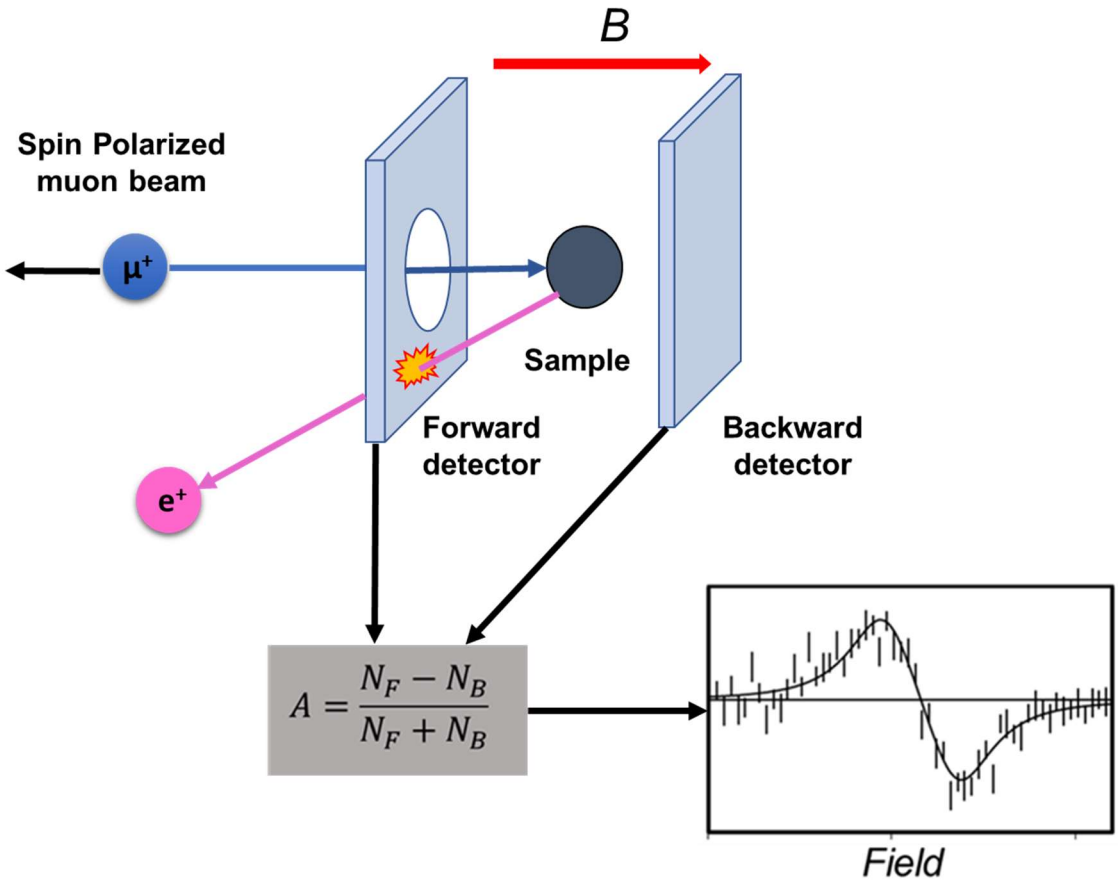

Figure 2-2: A schematic diagram of the ALC-μSR apparatus. In ALC-μSR the spin polarization of the muon beam is parallel to the applied magnetic field.

As shown in figure 2-2, the orientation and the number of positron counters is different for ALC-μSR. There are only two positron counters used in this arrangement, in the forward (F) and the backward (B) directions with respect to the muon beam. In ALC-μSR a single particle counting method is not applied and therefore pile up is not a concern. Unlike TF-μSR, where a histogram accumulates data as a function of time, in

ALC-μSR the total muon decay asymmetry is recorded as a function of the applied magnetic field. The magnetic field was changed in small increments ranging from 10 G to 50 G, according to the experiment. In this project field scans typically ranged from 0 kG to 20 kG in steps of 20 G.

The number of positron counts in the forward and backward detectors are given by

$$F(t) = N_0 e^{t/\tau_\mu}\left[1 + A(t)\right] + B_g \tag{2.2}$$

$$B(t) = N_0 e^{t/\tau_\mu}\left[1 - A(t)\right] + B_g \tag{2.3}$$

where t is time, τ_μ is the muon lifetime, B_g is a constant background, N_0 is the normalization constant, and $A(t)$ is the asymmetry of the spectrum. Under the approximation that B_g and N have equal values for the two detectors, equations (2.2) and (2.3) can be combined to calculate the asymmetry as

$$A(t) = \frac{F - B}{F + B} \tag{2.4}$$

The ALC-μSR spectrum comprises a plot of $A(t)$ versus magnetic field. As described in chapter 1, the simultaneous spin flip of the muon and another nucleus changes the asymmetry. However, the raw integrated asymmetry is prone to systematic error and makes it difficult to distinguish signals with smaller amplitudes. Therefore a small modulation field of 100 G is introduced to counteract systematic errors. The modulation field is applied parallel (+) and anti-parallel (-) to the external magnetic field at each step, and the data is plotted as the difference of two asymmetries.

$$A^+ - A^- = \frac{\left(F^+ - B^+\right)}{\left(F^+ + B^+\right)} - \frac{\left(F^- - B^-\right)}{\left(F^- - B^-\right)} \tag{2.5}$$

For best results, the applied modulation field needs to be smaller than the width of the resonance, and in this particular project ^{31}P and ^{1}H resonances have larger width than 100 G, hence the above-mentioned field modulation is used.

2.2. Data analysis

The data analysis of μSR is a process with several stages, where we retrieve the data and analyze it using various programs. All μSR data are archived at the TRIUMF server. The μSR data of interest are downloaded by accessing http://musr.org/mud/.

Field calibration data, TF-μSR data, and ALC-μSR data were analyzed using the muonfcn, WiMDA[50] and Excel programs respectively. The muonfcn program was used to fit the μSR histograms containing the diamagnetic signals used for field calibration. The four histograms of each run were fitted separately using a non-linear chi-squared minimization procedure (MINUIT)[51] and the weighted average of the frequencies taken.

The WiMDA program, developed by Francis Pratt at the ISIS facility in the UK, was used to fit μSR histograms containing multiple precession frequencies (radical signals). The software can be freely accessed at http://shadow.nd.rl.ac.uk/wimda/.

ALC-μSR runs were analyzed using Excel to fit Lorenzian curves to the data. Each resonance is characterized by a field position, amplitude and width.

2.3. Computational calculations

For most of the experiments discussed in this thesis computational calculations were done to support interpretation of the experimental data. Geometries of the parent molecules and muoniated radicals were optimized and hyperfine constants calculated. In addition, reaction pathways, rotational and vibrational motions were modeled to discern the behavior of the muoniated radicals.

In computational chemistry, electronic properties of a many-body system can be described by the time-independent non-relativistic Schrödinger equation.

$$\hat{H}\psi = E\psi \tag{2.6}$$

where $\hat{H}$ is the Hamiltonian and ψ is the many-body wave function. Within the Born-Oppenheimer approximation the nuclear part of the wave function and the electronic part are separated. The Hamiltonian operator can be expanded to

$$\hat{H} = \hat{T}_e + \hat{V}_{ee} + \hat{V}_{ne} + \hat{V}_{nn} \quad (2.7)$$

where $\hat{T}_e$, $\hat{V}_{ee}$, $\hat{V}_{ne}$ and $\hat{V}_{nn}$ are the kinetic energy, electron-electron repulsion, nuclear electron attraction, and nucleus-nucleus repulsion operators, respectively. The nuclear repulsion operator is independent of electron coordinates, and the electron kinetic energy and nuclear electron attraction operators depend on single electron coordinates. However, the electron-electron repulsion energy (electron correlation) operator depends on electron coordinates.

When considering many-electron systems, calculating electron correlation is difficult, hence the exact solution to the non-relativistic Schrödinger equation cannot be formulated. To address this complicated problem, many-body systems are simplified by introducing the independent particle approximation, where electron correlation is either completely ignored or only taken into account by taking all the interactions as an average.

In the ladder of methods trying to account for electron correlation the Hartree Fock (HF) theory can be considered as the first rung. HF theory assumes that the electronic wave function takes the form of a single Slater determinant consisting of one spin-orbital for each electron. In the HF method each electron moves independently in its spin-orbital space and experiences electron correlation as a Coulombic repulsion due to the overall electron density calculated by averaging all the other electrons in the space. According to the variational principle the HF method then determines the set of spin orbitals that gives the minimum energy to find the best Slater determinant. The HF electronic Schrödinger equation is as follows.[52]

$$\left(-\frac{1}{2}\nabla^2 + \frac{Z_A}{r_{Ai}} + V_{\text{eff}}^{\text{HF}}(r) \right) \psi_i(r) = \varepsilon_i \psi_i(r) \quad (2.8)$$

where ψ_i is the wave function, ∇^2 is the Laplacian operator, $\left(\frac{Z_A}{r_{Ai}} \right)$ the electron nuclear interaction, $V_{\text{eff}}^{\text{HF}}$ is the HF operator and ε_i is the eigenvalue of the i^{th} electron.

Even though the HF method can explain the majority of the total energy and the wave function of the molecule, it does not include electron correlation, which is vital in explaining the chemistry of the molecule. To answer this, post-HF methods were developed, e.g. Configuration Interaction methods (CI) such as CISD, MCSCF, and CASSCF. The CI methods include electron correlation, and combined with a large basis set can more accurately determine the energy. However, these methods are computationally expensive.

Density Functional Theory (DFT) is an alternative that can incorporate correlation more effectively with less computational power. DFT methods are based on an electron density operator. According to Hohenberg and Kohn ground state molecules can be described with density functions.[53,54] The DFT electronic density potential can be expressed as follows

$$\left(-\frac{1}{2}\nabla^2 + \frac{Z_A}{r_{Ai}} + V_{\text{eff}}^{\text{KS}}(r) \right) \psi_i(r) = \varepsilon_i \psi_i(r) \tag{2.9}$$

where the first term is the Laplacian operator and $\nu_{\text{eff}}^{\text{KS}}$ is the effective potential operator. The effective potential operator can be described as follows

$$V_{\text{eff}}^{\text{KS}} = V_{\text{ext}}(r) + V_{\text{HF}}(r) + V_{\text{XC}}^{\text{KS}}(r) \tag{2.10}$$

where V_{HF} is the HF potential, V_{ext} is the external potential and $V_{\text{XC}}^{\text{KS}}$ is the exchange correlation potential. The exchange correlation potential is

$$V_{\text{XC}}(r) = \frac{\partial E_{\text{XC}}[\rho(r)]}{\partial \rho(r)} \tag{2.11}$$

$$\rho(r) = \sum_{i=1}^{N} |\psi_i(r)|^2 \tag{2.12}$$

For this research a hybrid functional of the DFT method, B3LYP, has been used.[55] The B3LYP method is the most frequently used method in DFT calculations. Apart from the selection of methods, it is also important to use an appropriate basis set for the calculations.

In order to optimize the structures a trial wave function is built using a selected basis set. According to the variation principle, to optimize a trial wave function in each iteration of optimization coefficients are recalculated to reduce the energy of the trial wave functions. This process is carried out until two consecutives energies agree within a predetermined threshold value.

2.3.1. Basis sets[56,57]

A basis set is a linear combination of a set of mathematical functions (basis functions) that is used to describe molecular orbitals. The basis set can be constructed from Slater type orbitals and Gaussian orbitals. Even though the Slater orbitals can more accurately describe the shape of molecular orbitals they are more time consuming to compute. Gaussian orbitals are more easily calculated but do not accurately explain the molecular orbitals. Hence as a compromise a Slater type of orbital built by linearly combining Gaussian orbitals can be used. To describe a system at least one basis function should be assigned to each molecular orbital (MO). Frequently double-zeta, triple-zeta or quadruple-zeta (containing 2,3 and 4 basis functions for a MO respectively) basis sets are used for computational calculations, having multiple basis functions gives a greater flexibility to the MO orbitals behavior. In addition, adding polarization functions or diffuse functions can also increase the accuracy of the modeled orbitals.

It is vital to select a good basis set to describe the trial function. In principle, the true wave function can be obtained by applying an infinitely large basis set. However, in practice it is necessary to compromise between a basis set with small error and one with computational efficiency.

The basis sets EPRII and EPRIII developed by Barone et al. are tailored towards calculation of unpaired electron density.[58,59] However, they can only be applied to H and the B to F row of the periodic table. The calculations in this study used the 6-31G(d,p) and TZVP basis sets.[57] The accuracy and the selection of these basis sets are consistent with literature, where radicals modeled using these basis sets result in close agreement between experimental and theoretical results.

In our work we calculate the isotropic hyperfine coupling constants of muoniated radicals. Fermi contact interactions are directly proportional to the unpaired electron spin density at the nucleus.[52]

$$A_x = \frac{2\mu_0}{3h} g_e \beta_e g_N \beta_N \left|\psi_{(0)}\right|^2 \qquad (2.13)$$

where g_e and g_N are electron and nuclear gyromagnetic factors, β_e is the Bohr magneton, β_N is the nuclear magneton and h is the Planck constant.

In addition, muonium shows pronounced isotopic effects because of its light mass. These effects are included in the calculations by applying vibrational averaging (done with the Fermi keyword in Gaussian).

2.3.2. The software package

Calculations in this thesis were carried out using the Gaussian 09 package[57] on WestGrid and Compute Canada facilities.

Chapter 3.

Investigating the compatibility of PEEK polymer for the fabrication of sample cells for use in muon spin spectroscopy

*The content of this chapter has been published in modified form as Chandrasena et al., Journal of Physics: Conference Series **551** (2014) 012038; doi:10.1088/1742-6596/551/1/012038. Reproduced material is included here under the Creative Commons Attribution 3.0 licence.*

3.1. Introduction

Materials used for μSR sample cell construction should have a number of important properties. They should be chemically inert and non-magnetic, be able to withstand high pressure and temperature conditions, yet allow the fabrication of thin enough entrance windows to allow muon penetration with minimum stops and scattering in the window itself, to optimize muon stops inside the cell cavity containing the target material. In addition, for radio-frequency experiments, the sample cell should be electrically non-conducting to prevent the RF cavity from interacting with the cell material. In this context polyether ether ketone (PEEK) was considered as an ideal material for sample fabrication, particularly for the inert gas experiments done using radio frequency spectroscopy.[60]

PEEK has a wide range of applications due to its thermoplastic properties and chemical inertness. Muons that are stopped inside the PEEK polymer have only 0.1% diamagnetic polarization and 90% missing fraction[61] (a fraction that undergoes depolarization). Thus, it appeared to be a good material for sample cell fabrication.[60]

However, in a study done by Johnson et al.[60] on muon implantation in inert gases, TF-μSR experiments of Ne and He encapsulated in PEEK cells revealed a marked increase in Mu signal compared to previous experiments. It was suggested this might be due to an impurity outgassing from the PEEK polymer creating a neutralization reaction.

$$NeMu^{+} + X \rightarrow Mu + NeX^{+} \qquad (3.1)$$

The objective of our study was to whether PEEK polymer forms muoniated radicals, which would make it an unsuitable material for sample cell fabrication for experiments studying Mu and muoniated radicals and to identify the structures of the resulting radicals. PEEK is a polymer with an alternating aromatic ring structures where a 4,4′-substituted benzophenone and a para-substituted benzene are connected with each other via ester linkages. It is established that Mu adds to benzene rings forming muoniated cyclohexadienyl radicals and in addition, Mu also adds to ketone groups to form muoniated radicals. The structure of the PEEK polymer repeating unit and the corresponding monomers as given below

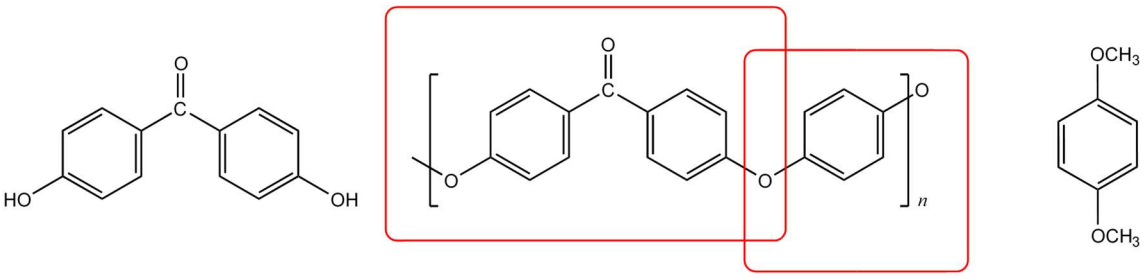

Figure 3-1: The structure of the polyether ether ketone (PEEK) repeating unit (centre) and the sub-units of 4,4-dihydroxybenzophenone (left) and para-dimethoxybenzene (right).

3.2. Results and discussion

In an experiment performed at ISIS by Cottrell and McKenzie the ALC-μSR spectrum of PEEK at 360 K was found to exhibit a broad signal between 14 kG and 23 kG.[62] There is a broad feature that is super imposed on the on the non-linear background. The background can be attributed to the effects of magnetic field on the muon beam spot and the positron trajectories in the spectrometer. The background-subtracted signal is on the right (figure 3-2). We propose that this signal is due to the overlap of multiple cyclohexadienyl radicals with restricted rotations. In order to confirm the formation of cyclohexadienyl radicals, we studied the PEEK monomers.

(a) (b)

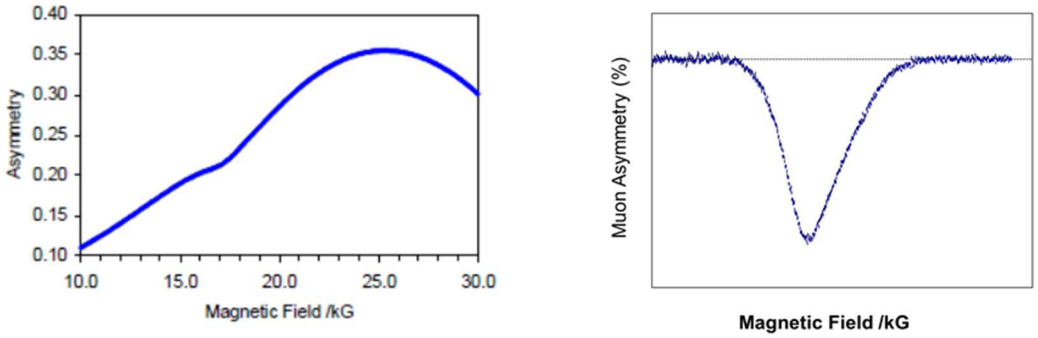

Figure 3-2: The ALC-μCR spectrum of PEEK polymer at 360 K (a) The signal before background subtraction. (b) The signal after the background subtraction.

4,4'-dihydroxybenzene and para-dimethoxybenzene were dissolved in dry and degassed ethanol and THF to have 1.43 M and 1.05 M concentration respectively. The TF-μSR spectra of both compounds were recorded at 25 °C. In both spectra, the large peak at 131 MHz is due to the muons in diamagnetic environments.

Figure 3-3 (a) shows two pairs of signals symmetrically placed on either side of the diamagnetic signal hence two muoniated radicals are formed in 4,4′ dihydroxy-benzophenone solution. As mentioned earlier, since detectors are set in phase quadrature it allows us to distinguish between different directions of muon spin rotation of radicals. The negative region of the spectrum shows frequencies of the muon that spin opposite to the direction of the diamagnetic rotation.

A single radical was detected from para-dimethoxybenzene (figure 3-3 (b)). The muon hfc constants of the radicals are given in table 3-1 below. The hfc constants were determined from the separation of the signal pair or calculated from equation (3.2) by using the stronger radical signal (ν_{R1}) and the diamagnetic signal (ν_{μ}) frequency (3.2).

$$A_{\mu} = 2\frac{(\nu_e + \nu_{R1})(\nu_{\mu} - \nu_{R1})}{(\nu_e - \nu_{\mu} + 2\nu_{R1})} \qquad (3.2)$$

(a)

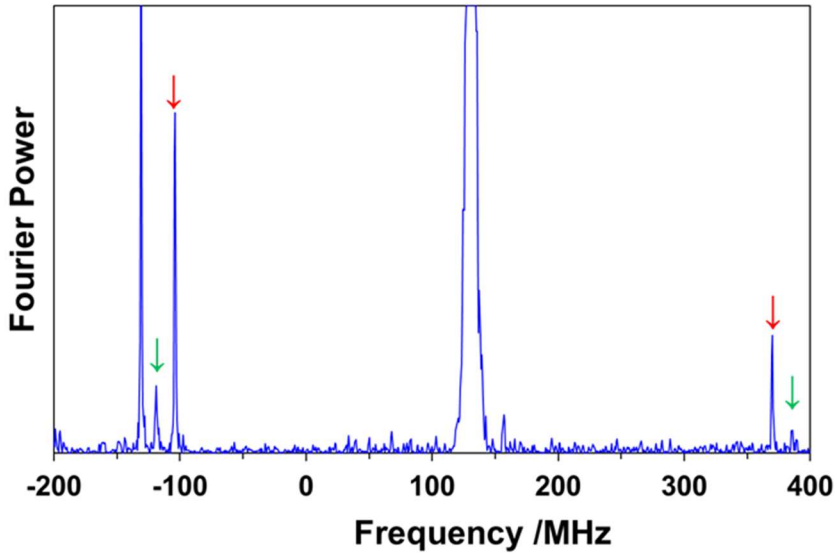

(b)

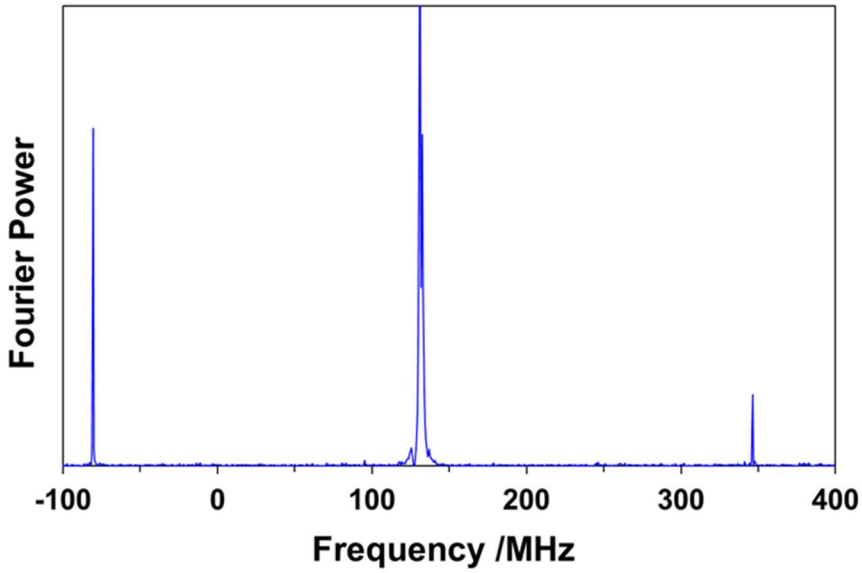

Figure 3-3: **Fourier transformed TF-μSR of (a) 4,4'-dihydroxybenzophenone solution at 25 °C. The precession signals of two different radicals are marked in with different colours. The strong signal at -131 MHz is and artifact, a ghost refection of the strong diamagnetic signal. (b) para-dimethoxybenzene solution at 25 °C.**

Table 3-1: Muon hyperfine coupling constant (A_μ) from TF-μSR spectra at 25 °C and the predicted magnetic fields ranges for the ALC-μSR signals of methylene protons

Parent Molecule	A_μ/MHz	Calculated B_{LCR} / kG
para-dimethoxybenzene	426.8(1)	15.668(4)
4,4ˈ-dihydroxybenzophenone	473.8(1)	17.394(4)
4,4ˈ dihydroxybenzophenone	504.2(3)	18.510(11)

The muon hfcs observed for both compounds are in the range 400–550 MHz and are compatible with muon hfcs of muoniated cyclohexadienyl radicals.[14,27] There is no evidence showing ketyl radical formation in 4,4ˈ-dihydroxybenzophenone. To obtain a more detailed comparison of hyperfine constants ALC-μSR studies were carried out. In the muoniated radicals, only the magnetic moments are different between muon hfcs and corresponding methylene proton hfcs (vibrational effects on the hfcs are not considered). Considering only the difference in magnetic moments of μ and proton we estimate that the methylene hfc is about one third of the muon hfc. Therefore, we can predict the magnetic field regions in the ALC-μSR spectrum where we can expect methylene proton signals.

The ALC-μSR signals were detected in the ranges expected for methylene proton signals. For 4,4′ dihydroxybenzophenone, two signals are observed. In theory, there is an ambiguity in assigning ALC-μSR resonances to the corresponding TF-μSR signals because there are multiple radicals present. However, TF-μSR signal intensities compared with ALC μSR signal intensities aid in assigning them in to corresponding TF-μSR signal.

(a)

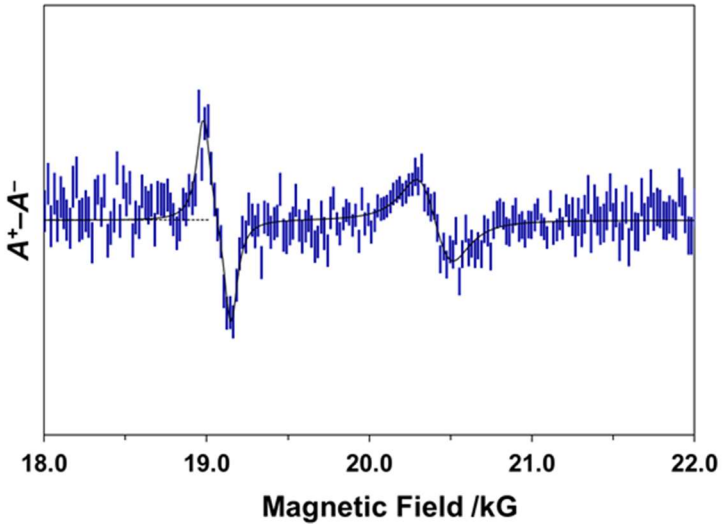

(b)

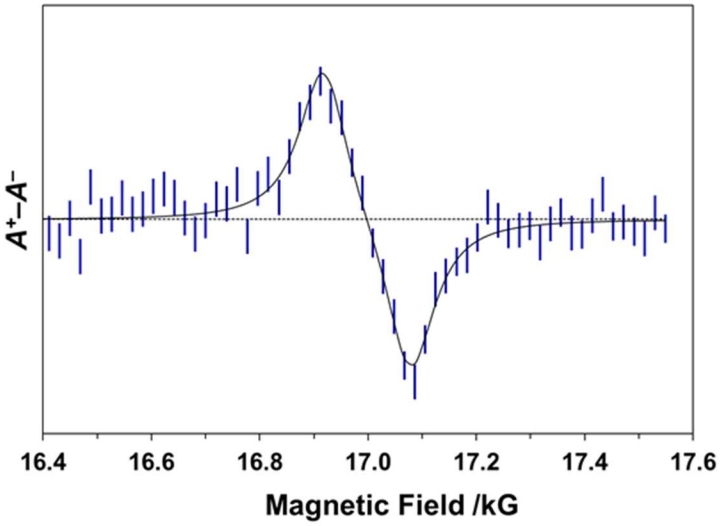

Figure 3-4: Segments of ALC-μSR spectra recorded at 25 ºC for (a) 4,4′ dihydroxybenzophenone solution (b) para-dimethoxybenzene. Both spectra segments display narrow signals with high intensity that are characteristic for cyclohexadienyl protons.

Table 3-2 shows the ratio of the reduced muon hfc and the methylene proton hfc. The difference in reduced muon hfc and the methylene proton hfc is due to the vibrational isotopic effect. DFT calculations were carried out to help assign structures to the three radicals detected experimentally. We have not considered the C centers where substituent groups are already attached, due to the steric effects. The proposed muoniated radical structures are shown in figure 3-5.

Table 3-2: Experimental muon and proton hfcs and the residual vibrational isotope effect

Parent Molecule	A_μ / MHz	A_p / MHz	0.31413 A_μ / A_p
para-dimethoxybenzene	426.8(1)	109.1(1)	1.23
4,4′-dihydroxybenzophenone	473.8(1)	117.4(1)	1.27
4,4′ dihydroxybenzophenone	504.2(3)	122.8(4)	1.29

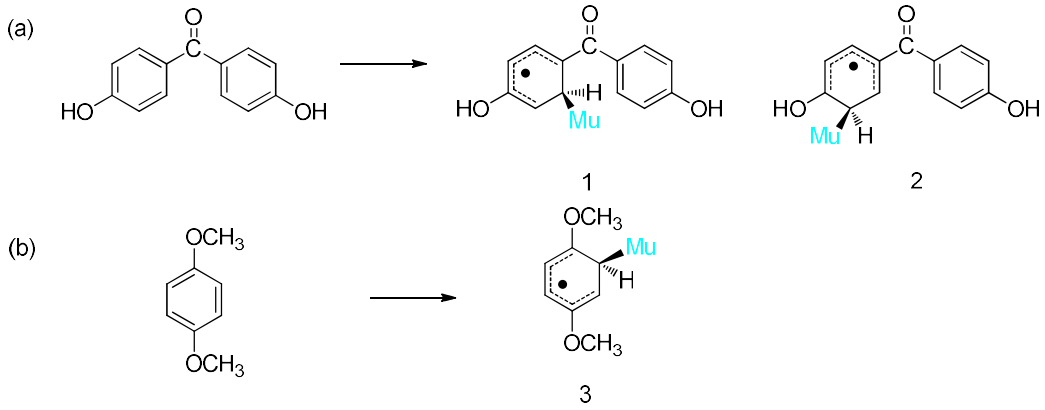

Figure 3-5: Muonium addition to PEEK polymer monomers to form muoniated cyclohexadienyl radicals (a) 4,4′ dihydroxybenzophenone (b) para-dimethoxybenzene.

The G09 suite of programs was used to optimize molecular geometries of potential muoniated radicals and compute their isotropic hyperfine constants, using the UB3LYP hybrid density functional and the 6-31G basis set. The muonium atom was explicitly included in the calculations as an isotope of H with mass 0.113429 u and magnetic moment 8.6578226 μ_N.[63] The symmetric nature of para-dimethoxybenzene means only one muoniated cyclohexadienyl radical can be formed, while 4,4′-dihydroxy-benzophenone can form both ortho and meta muoniated radicals. Hyperfine coupling constants were calculated for both reference geometries and the vibrationally averaged geometries at 25 °C and are recorded in table 3-3.

Table 3-3: Muon and proton hyperfine constants calculated for the reference geometry (A_0) and as vibrationally averaged at 298 K (A_{298})

Parent Molecule	Radical	Nucleus	A_0/MHz	A_{298}/MHz
4,4′-dihydroxybenzophenone	1	μ	425.5	538.7
4,4′-dihydroxybenzophenone	1	H	138.1	133.1
4,4′-dihydroxybenzophenone	2	μ	448.5	510.7
4,4′-dihydroxybenzophenone	2	H	154.9	139.3
para-dimethoxybenzene	3	μ	425.6	520.9
para-dimethoxybenzene	3	H	138.0	132.3

The calculated hfc values for the reference geometry closely match the experimental hfcs for muon and methylene protons for proposed radical structures **1, 2** and **3**. Vibrational averaging in this case overestimates the muon hfc constants. For 4,4′-dihydroxybenzophenone, we do not see evidence of ketyl radical formation. Typically, muoniated ketyl radicals produce small signal pairs close to diamagnetic peaks with hfc approximating 32 MHz. However, we do not observe similar signals in our current spectrum. The Mu addition rate to benzene is higher than to carbonyl groups and the cyclohexadienyl radicals are more stable compared to ketyl radicals due to electron delocalization on the ring. These effects are further amplified by 4,4′-dihydroxy-benzophenone having electron-donating and electron-accepting substituent groups that give additional stability to cyclohexadienyl radicals. In figure 3-3(a) the high intensity signal is due to **2** where Mu addition is ortho to the electron donating OH group and meta to the electron withdrawing carbonyl group. Combination of these effects enhances the electron density at the C center. However radical **1** is formed at the C center where it is ortho to the electron-withdrawing group and meta to the electron donating group where the combine effects reduce the electron density. This results in the less intense outer signal pair.

3.3. Conclusion

Extrapolating the results of this investigation of the monomer subunits of PEEK, it is clear that overlapping resonances from radicals formed by Mu addition to benzene

rings in the polymer can account for the broad ALC-μSR signal observed in PEEK. It is therefore concluded that PEEK sample cells are unsuitable for many types of μSR experiment, in particular those involving muonium or muoniated free radicals, because the PEEK polymer can produce signals which could interfere with those of the sample under study.

Chapter 4.

Free Radical Reactivity of a Phosphaalkene Explored Through Studies of Radical Isotopologues

*The content of this chapter has been published in modified form as Chandrasena et al., Angewandte Chemie **58** (2019) 297-301; doi:10.1002/anie.201810967.*

4.1. Introduction

In recent years, phosphorus compounds displaying multiple bonding and/or low-coordination numbers have emerged from their purely fundamental roots to become attractive building blocks and synthons with applications ranging from catalysis to polymer and materials science.[40,42,64,65] Of particular interest to us are phosphaalkenes (often touted as P=C analogues of olefins)[42,66] which we have shown to be suitable monomers for radical-initiated homo- and co-polymerization.[67,68] Despite the discovery of an unexpected microstructure for the polymer derived from mesP=CPh_2,[69,70] the details of the simple free radical initiation remain unclear. Presumably, initiation involves the addition of neutral radicals to the P=C bond but such short-lived radical intermediates are extremely difficult to generate and characterize.

As an alternative to EPR, we have turned to muon spin spectroscopy (μSR) to detect muoniated radicals, e.g. free radicals containing a muonium atom (Mu) in place of an H atom. Mu is a single-electron atom, with a positive muon (μ^+) as nucleus, that may be envisaged as a light isotope of H (mass = 0.11 u). Thus, reacting low-coordinate compounds with Mu provides a rare opportunity to generate, and elucidate the structure of, radicals that could not otherwise be detected.[33-37,71-73] μSR offers several advantages over conventional methods: (i) muons can be injected into any sample; (ii) the muons arrive with almost 100% spin polarization, so very low quantities of muoniated species can be detected; (iii) very short-lived muoniated radicals can be detected; and (iv) unlike conventional EPR or NMR, μSR does not require an external electromagnetic field to stimulate spin level transitions. Perhaps the most significant advantage of μSR is its

high selectivity of detection which minimizes complications from radiation damage and secondary radical species.

Despite the utility of Mu to probe novel radicals, there is no report of its reaction with low-coordinate phosphorus. The only muoniated P-radical was derived from tricoordinate phosphorus.[74] This is particularly striking given the longstanding interest in development and applications of divalent phosphorus-based radicals.[75-84] Also, there is growing interest in anionic and cationic radicals derived from phosphaalkenes[85-92] but there is a dearth of information on the addition of neutral radicals to P=C bonds. Most pertinent to the present study is the EPR detection of a mixture of neutral P- and C-centered radical and cationic phosphoniumyl radicals detected when single crystals of mes*P=CHPh (mes* = 2,4,6-tri-tert-butylphenyl) were irradiated with X-rays,[93,94] presumably reacting with adventitious H sources.

4.2. Results and discussion

Herein, we report two unprecedented radicals derived from the addition of Mu, a "light H isotope", to phosphaalkene mesP=CMe_2 in solution at ambient temperature. The simple addition of Mu to the P=C bond of **4a** is expected to result in the formation of up to two unique muoniated radicals, **4a-P-Mu** or **4a-C-Mu** (figure 4-1). Employing phosphaalkene **4a** provides an advantage in elucidating the structures of these addition products since it exists in equilibrium with its alkene tautomer mesPH($CMe{=}CH_2$)$_2$ (**4b**),[95]

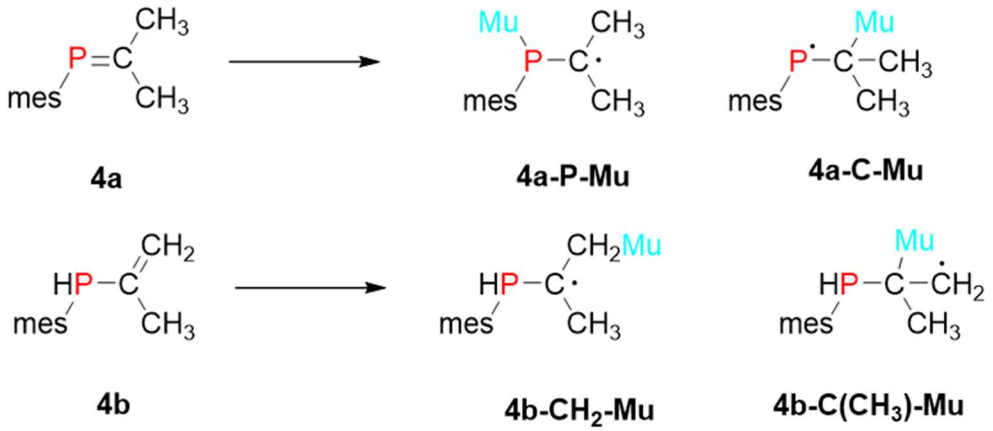

Figure 4-1: Muoniated radicals expected from Mu addition to a phosphaalkene 4a and isomeric alkene 4b.

which can be independently studied in its pure form. In agreement with past studies of terminal alkenes,[24] addition of Mu to the carbon-carbon double bond of **4b** is expected to give the tertiary radical **4b-CH_2-Mu** rather than the primary radical **4b-C(CH_3)-Mu** (figure 4-1). The Mu adduct of **4b-CH_2-Mu** is an isotopologue of **4a-P-Mu** with the only difference being the site of Mu substitution. Thus, **4a-P-Mu** and **4b-CH_2-Mu** should have the same unpaired spin density at the carbon radical center, leading to hyperfine coupling constants (hfcs) that differ only as a result of the isotopic substitution.[96]

As a starting point, we exposed a THF solution of pure alkene **4b** to a beam of positive muons ($\mu^+ + e^-$ gives Mu). The transverse-field muon spin rotation (TF-μSR) spectrum (figure 4-2) shows two radical precession signals (ν_1 and ν_2) in addition to the diamagnetic signal (ν_D). This observation suggests that the reaction of **4a** with Mu affords a single radical product. The muon hyperfine constant (A_μ) of this product is given by the difference between the two radical precession frequencies. At 25 °C, the value of A_μ is 254 MHz but it varies with temperature (Appendix A figure A1).

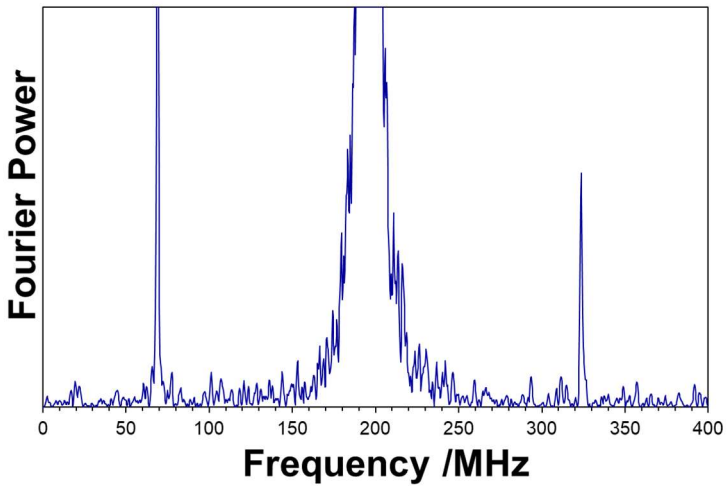

Figure 4-2: Transverse field μSR (TF-μSR) spectrum at 14.45 kG obtained from a solution of 4b in tetrahydrofuran at 25 °C.

A different form of muon spin spectroscopy, muon avoided level-crossing resonance (ALCR-μSR), provides the means to determine other nuclear hyperfine constants, as explained in previous chapters. The ALCR-μSR spectrum obtained from the reaction of **4b** with Mu is displayed in figure 4-3. A total of four resonances are expected from **4b-CH_2-Mu**, one due to ^{31}P (I = ½) and three associated with the

inequivalent protons: PH, CH_2, and CH_3. The signal at 4.8 kG (figure 4-3) is readily assigned to phosphorus with hfc A_P = 140 MHz. The alternative assignment to one of the protons is unfeasible, because it would give A_H = 164 MHz, a value too high for the proposed radical structure for **4b-CH_2-Mu**. In contrast, the assigned phosphorus hfc is in the range typically found for phosphinyl radicals (see below).

(a)

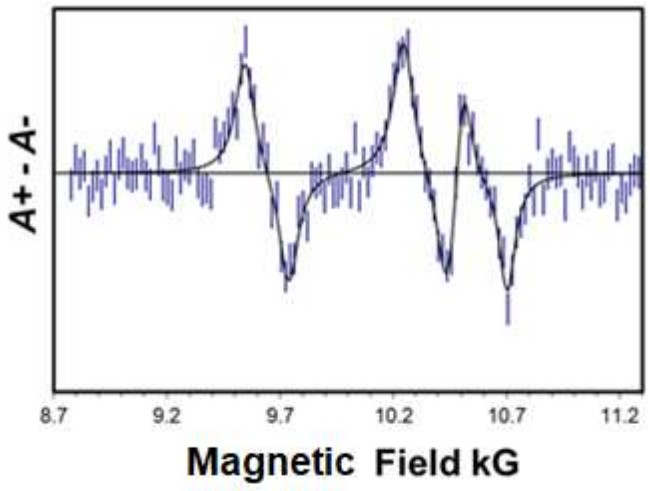

(b)

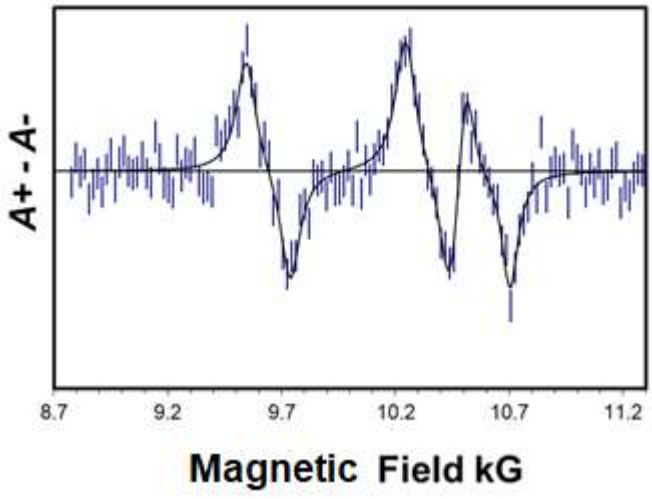

Figure 4-3: Segments of the muon avoided level-crossing spectrum (ALCR-μSR) of the radical formed from a pure sample of 2 in tetrahydrofuran at 25 °C and subsequently identified as 2a. The two field regions are consistent with assignments to (a) ^{31}P; (b) three unique ^{1}H environments (i.e. CH_2, CH_3 and PH).

Individual assignment of the three resonances attributed to protons is more complicated, and ultimately relies on comparison with computational prediction of the hfcs. However, some qualitative arguments can be made on the basis of isotope effects in the $–CH_2Mu$ group and the observed temperature dependence of the hfcs. A freely rotating $–CH_3$ group has three equivalent protons and averaging of the dihedral angles Φ results in $\langle\cos^2\Phi\rangle = 0.5$ and a proton hfc which is essentially temperature independent. In contrast, the preference of Mu for small dihedral angles in the muoniated methyl group $-CH_2Mu$ results in well-established temperature dependence: the muon hfc falls with temperature and the proton hfc increases with temperature.[26] Additional details of the temperature dependence are given in Appendix A. Based on the above, the four resonance field positions and the corresponding hfcs are assigned as shown in table 4-1 and are fully consistent with the structure of **4b-CH_2-Mu**. In particular, it was established that the H attached to phosphorus has A_H = 71.4 MHz. This is relevant to consideration of the isotopologue **4a-P-Mu**, which has Mu in this position. Scaling by the ratio of magnetic moments leads to a predicted muon hfc of about 230 MHz.

Table 4-1: Analysis of the muon avoided level-crossing (ALC-μSR) spectrum obtained from 4b in tetrahydrofuran at 25 °C and subsequently identified as 4b-CH_2-Mu

Assignment	Hyperfine constant / MHz	Resonance field/ kG
P-H	139.55 (0.09)	4.779(0.004)
P-***H***	71.4 (0.08)	9.778(0.004)
C***H₃***	58.37(0.04)	10.481(0.002)
C***H₂***Mu	52.98(0.04)	10.772(0.002)

It is evident from the TF-μSR spectrum shown in figure 4-4 that two different radicals ensue from the reaction of Mu with the phosphaalkene **4a**. The more intense radical signal has A_μ = 304 MHz at 299 K. This is 34% higher than the value estimated for **4b-CH_2-Mu** above but this could be due to an isotope effect, which will be discussed later in the context of our computational investigation.

The less intense signal (henceforth referred to as the minor radical) has a smaller muon hfc (A_μ = 135 MHz). Moreover, the Fourier transform signal intensity varies if the μSR histogram time window is delayed with respect to the muon arrival

time. This curious behaviour has been observed in other systems and, while not fully understood, it seems to indicate delayed formation of a radical.[97]

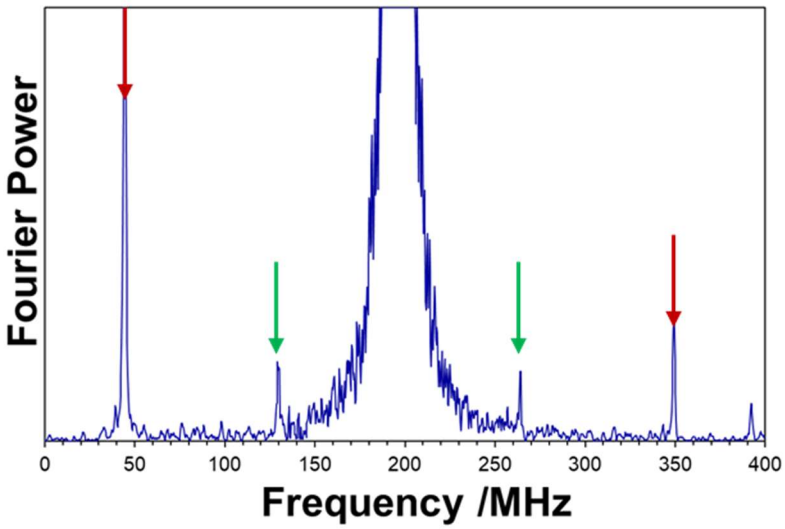

Figure 4-4: Transverse field μSR spectrum at 14.45 kG obtained from a solution of 4a in THF at 3 °C. The signals of two radicals are evident. The signal pairs are color coded. The small signal at 312 MHz is an artefact, an overtone of the intense diamagnetic signal.

The ALCR μSR spectrum obtained from the reaction of **4a** with Mu shows two resonances consistent with phosphorus (figure 4-5(a)) and only one signal in the region where protons would give a resonance (figure 4-5(b)). A single proton resonance is just what is expected for radical **4a-P-Mu**, which has six equivalent protons in the methyl groups attached to the carbon radical center. Assignment of the two ^{31}P signals is not so straightforward. This part of the spectrum is markedly temperature-dependent, as shown in figure A2 in the Appendix. The gradual broadening and disappearance of the resonance near 6.4 kG as the temperature was reduced suggests some temperature-mediated dynamic effect. Since radical **4b-CH_2-Mu** did not show this effect we may suppose that this unusual behavior is associated with the minor radical observed in the TF-μSR spectrum, namely the phosphinyl **4a-C-Mu**.

(a)

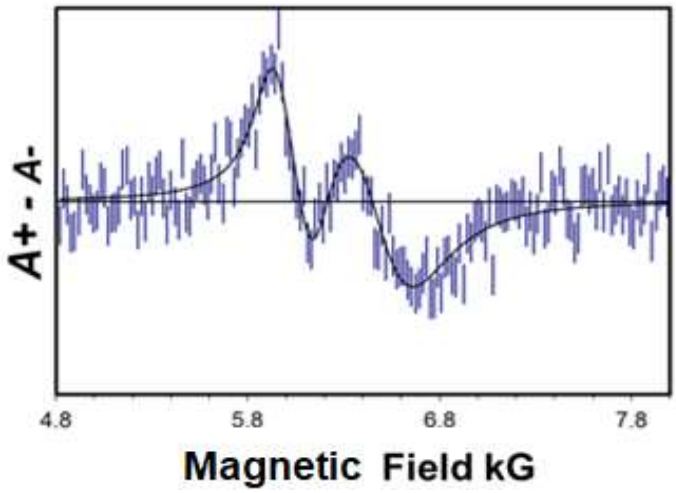

(b)

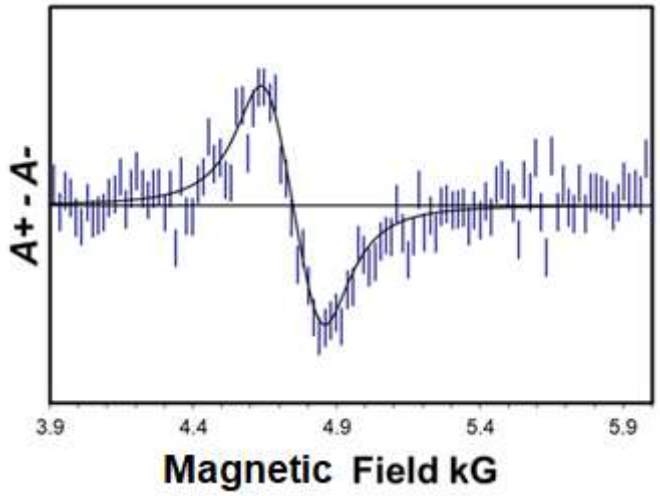

Figure 4-5: Segments of the ALCR μSR spectrum of the radicals formed from a solution of 4a in tetrahydrofuran at 26 °C. The two field regions are consistent with assignments to (a) ^{31}P (one signal each from 4a-P-Mu and 4a-C-Mu); (b) six equivalent protons in 4a-P-Mu (i.e. two CH_3 groups).

In principle there is ambiguity in the translation of ALCR-μSR resonance fields to hfcs because the field position depends (equation 2.5) on an absolute value, $|A_\mu - A_k|$, where k represents the relevant nucleus. In most cases it can safely be assumed that $A_\mu > A_k$, but this is not the case here. If the major radical (A_μ = 304 MHz) is assigned to **1b**, and $A_\mu > A_P$, then the 6.0 kG resonance translates to A_P = 160 MHz, a value close to that of its isotopologue **4b-CH_2-Mu** (A_μ = 254 MHz, A_P = 140 MHz). It then follows that $A_\mu < A_P$ for the 6.4 kG resonance, which translates to A_P = 285 MHz for the minor

radical, postulated to be **4a-C-Mu**. The near coincidence of the two phosphorus resonances is a consequence of the accidental degeneracy of (A_μ-A_P) and (A_P-A_μ) for the two radicals. As far as we are aware, this is the first report of such a situation.

Table 4-2 summarizes the analysis of the ALC-μSR spectrum shown in figure 4-5. The resonance at 13.2 kG is attributed to the methyl protons of **4a-P-Mu** (A_H = 58 MHz), and is supported by the fact that isotopologue **4b-CH_2-Mu** displays the same hfc. Furthermore, the unpaired electron in **4a-C-Mu** is too far from any proton to give a significant hfc. Thus, both the phosphorus and proton hfcs lead to the conclusion that the major radical formed from the reaction of **4a** with Mu is **4a-P-Mu**. Literature data on comparable ^{31}P hfcs of phosphinoalkyl radicals is sparse. Baban et al. reported a value of 178 MHz for the Et_2P-ĊHCH_2CMe_3 radical in solution at 300 K.[98] This is close to our value for **4a-P-Mu**. In contrast, the hfc reported by Begum et al. for Et_2P-ĊHCH_3 and similar radicals in irradiated solids at 77 K is only half this amount.[99]

Table 4-2: Analysis of the muon avoided level-crossing (ALCR-μSR) spectrum obtained from the reaction of 4a with Mu in tetrahydrofuran at 26 °C

Assignment	Hyperfine constant / MHz	Resonance field/ kG
P-Mu	160.3 (0.2)	5.986(0.005)
P-CMu	285.1 (0.6)	6.407(0.008)
C(C***H*****$_3$**$)_2$	57.8(0.1)	13.173(0.002)

Having identified the major radical as **4a-P-Mu**, the minor radical can then be assigned to the phosphorus-centered radical **4a-C-Mu** (A_μ 135 MHz, A_P = 285 MHz). The large phosphorus hfc is consistent with EPR studies of similar phosphinyl radicals. For instance, Fullam et al. found a ^{31}P isotropic hfc of 271 MHz for $(Me_2CH)_2P$ in an irradiated solid at 77 K,[76] and Bhat et al. reported a ^{31}P isotropic hfc of 333 MHz for Ar-P-CH_2Ph (Ar =2,4,6-tri(tert-butylphenyl) in an X-irradiated crystal at room temperature.[94]

To gain additional support for our assignments, density functional theory was employed to compute optimum geometries, vibrational frequencies and hyperfine constants of the radicals **4a-C-Mu**, **4a-P-Mu** and **4b-CH_2-Mu**. The “reference” geometries of isotopologues **4a-P-Mu** and **4a-C-Mu** are identical within the Born-Oppenheimer Approximation, since they represent the minimum-energy nuclear

configuration on the electronic potential surface. However, the vibrationally-averaged structures differ. Not only is there a small increase in bond length for the lighter isotope (P–Mu in **4a-P-Mu**; C–Mu in **4a-C-Mu**), there is also an effect on the dihedral angle about the P–C bond. Such effects are well-established for hydrocarbon radicals,[26] but this is the first time that they have been explored for organophosphorus radicals. The key hfcs are reported in table 4-3, where they are compared with the experimental results.

Table 4-3: Comparison of experimental and computed hyperfine constants (MHz)

Radical	Site	Exp / MHz	Calc / MHz
4a-CH_2-Mu	CH_2***Mu***	254	391
	C***H_2***Mu	53	35
	C***H_3***	58	57
	P***H***	71	58
	PH	140	136
4a-P-Mu	C***H_3***	58	58
	PMu	160	159
	P***Mu***	304	241
4a-P-Mu	***P***CMu	285	220
	PC***Mu***	135	141

In general, there is good agreement between the calculated hfcs and those determined by experiment. The apparent discrepancy for $-CH_2Mu$ in the first two rows of table 4-3 is explained by temperature dependence, as described in Appendix A. One can define an average value for the group:

$$\overline{A}(\mathrm{CH_2Mu}) = \left[\, 2A_{\mathrm{H}} + A'_{\mu} \,\right] \Big/ 3 \qquad (4.1)$$

where A'_{μ} is the muon hfc corrected by a factor (γ_p/γ_μ) to account for the different gyromagnetic ratios of the proton and the muon. The average value is then 62 MHz for the experimental data, and 64 MHz for the calculated value, both slightly higher than the proton hfc for the unsubstituted methyl (58 MHz) found for **4a-P-Mu**.

Conformational effects also affect the hfcs of PH (**4b-CH_2-Mu**) and PMu (**4a-P-Mu**). The vibrationally-averaged bond length is slightly longer (1.4%) for the lighter isotope at 0 K, but more significantly there is also a 4.6° change in the dihedral angle, Me-C-P-Mu (**4a-P-Mu**) vs. Me-C-P-H (**4b-CH_2-Mu**), resulting in an overall isotope effect of 36% on the calculated values of $A_{\mu'}/A_H$. A similar situation arises when Mu is attached to the carbon (**4a-C-Mu**). In this case, we calculate a 1.9% increase in bond length and a 4.6° change in dihedral angle mes-P-C-Mu, resulting in a 33% hyperfine effect compared to its C–H isotopologue. These zero-point vibrational effects involve high frequency vibrations: almost 7000 cm^{-1} for the P-Mu stretch, and 2600 cm^{-1} and 2200 cm^{-1} for the P-Mu wagging motions. In contrast, it is the lowest frequency vibrations that have the largest effect on the temperature dependence of the hfcs. Of particular relevance here is torsional motion about the P-C bond. This is only 35 cm^{-1} for PMu–C in **4a-P-Mu** and 33 cm^{-1} for P–CMu in **4a-C-Mu**. The floppiness of the radicals suggested by these low values results in significant uncertainty in the calculations. Nevertheless, we are satisfied that our computational results support our spectroscopic assignments. We will further discuss the effects of these low-frequency vibrational motions in larger phosphaalkene molecules in our next chapter.

4.3. Conclusion

We have explored the reaction of the P=C bond of a phosphaalkene with a light isotope of a hydrogen atom, namely, muonium. For the first time, the products of radical addition at either the P- or the C-atom of the P=C bond have been detected, with the C-centered radical (**4a-P-Mu**) being the major species. This work is consistent with the proposed mechanism for the polymerization of mesP=CPh_2, where the first step appears to involve highly selective addition of radicals to the P atom of the P=C bond to afford a C-centered radical intermediate.[69] In the next chapter we aim to use μSR spectroscopy to gain additional insight into the initiation mechanism for polymerization of different phosphaalkenes.

Chapter 5.

Muoniated radicals formed from phosphaalkenes

5.1. Introduction

As discussed in chapter 4, current interest in phosphaalkenes is due to their unique physical, chemical and electronic properties compared to their organic counterparts.[40] In polymer chemistry, phosphorus within the backbone can introduce new oxidation states, geometries, and bonding environments to the polymer, expanding their applications. The HOMO orbitals are the π orbitals of the P=C bonds. Different substituents connected to the P=C bond can alter the electron distribution.

With the discovery of mes-P=C(Ph)$_2$ and phosphaalkene polymerization by Gates and co-workers there has been growing interest in synthesizing functional polymers containing phosphaalkene monomers.[67,68] One of the most common methods for polymerization of alkenes is through radical initiation, and the same goes for their phosphaalkene counterparts. In radical polymerization, the initiation step has a large influence on the polymer structure and properties, especially whether the polymer structure is linear, branched, hyperbranched or cyclic, and optimization of polymer properties such as resistance to weathering, thermal and photochemical degradation.[100]

The polymer initiation process is typically kinetically controlled; hence the less thermodynamically favoured paths may be significant, even favoured, and multiple potential initiation radicals are possible. Understanding and controlling the polymer initiation step is thus crucial to predict and control the polymer structure and properties. Formation of the primary radical in an initiation process depends on the HOMO electron density, substituent effects and steric effects. Therefore, this chapter concerns the systematically investigation of several phosphaalkenes using muon spin spectroscopy to verify some key concepts:

1. What is the effect of electronegativity of substituent groups on radical formation at P=C bonds?
2. What is the possibility of manipulating radical initiation to selectively enhance the desired product?

5.2. Use of local mode vibrational method

Most of the phosphaalkenes are complex and flexible molecules with multiple potential sites for Mu addition. Typically, as shown in chapter 4, the Mu addition site can be confirmed using computational calculations. However, as the size and complexity of the molecules studied in this chapter increased, calculations using vibrational averaging keywords (Anharmonic, Readanharm) became extremely time consuming and underestimated muon hfcs. Therefore, computationally less expensive but reliable methods for hfc calculations are required.

Accordingly, in this chapter we employ local mode vibrational corrections and empirical methods to assign the radical structures. The local mode vibrational correction method selectively uses the specific vibrational modes that involve the Mu nucleus to calculate the Boltzmann-averaged hfc constants of the populated vibrational levels of the molecule.[29]

This is the first study of phosphalkenes using μSR. Therefore, we modeled the vibrational modes of the muoniated radicals of phosphaalkenes to identify the modes that involve the muon nucleus. It is noted that for the Mu-C and Mu-P bonds stretching and torsional motions are the most prominent vibrational motions that involve Mu. These vibrational modes are similar to the vibrational modes in muoniated radicals formed from alkenes. Details can be found in studies done by Percival et al.[26] on muoniated tertiary butyl radicals and studies done by Fleming et al.[101,102] on various butyl radicals.

The stretching vibrations for P-Mu and C-Mu radicals of phosphaalkenes are larger than 3000 cm^{-1}, hence only the $v = 0$ vibrational level is populated at room temperature. The torsional motion around the P-C bond has a significant effect on the movement of the muon nucleus. These motions have low frequencies (below 100 cm^{-1}) hence at room temperature multiple vibrational levels are populated. In this study potential energy surfaces for P-Mu and C-Mu rotation around the P-C axis were calculated in 5° increments. The Boltzmann average of rotamers with significant population was calculated according to the following equation

$$A = A_i \frac{e^{-\Delta E_i/kT}}{\sum e^{-\Delta E_i/kT}} \qquad (5.1)$$

where A_i is the vibrationally averaged hfc in vibrational state *i*. We have used this approach for the hfc calculation of muoniated radicals in this chapter with the exception of mes-P=C(Ph)$_2$ which is discussed separately in section 5.5.

5.3. Effects of substituent electronegativity on radical formation at the P=C bond

5.3.1. Experimental studies of $(CF_3)_2$-mes-P=C$(CH_3)_2$

There are only two studies available on the radical reactivity of phosphaalkenes with electronegative groups attached.[89,90] Both studies were carried out on cationic radicals and no information is available on neutral radicals. The studies done by Pan et al.[89] and Rosa et al.[90] employed phosphaalkenes with an amino group attached to the carbon atom of the P=C bond. They concluded that electronegative substituents cause inversion of electron densities, making P negatively charged. Therefore, it was evident that by controlling substituent groups, one can significantly alter the electronic properties of the P=C bond. Hence, to understand the effects of electronegativity of the substituent groups on neutral radicals we expanded our study based on compound **4a** (mes-P=C(CH3)$_2$) from chapter 4 to derivatives with electronegative groups attached. Compound **5a** has CF_3 groups attached to the phenyl group altering its electronegativity (figure 5-1).

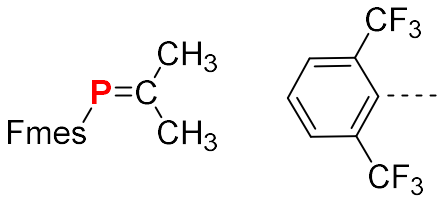

5a **Fmes**

Figure 5-1: Structure of $(CF_3)_2$-mes-P=C$(CH_3)_2$ [5a].

We hypothesized that similar to **4a,** compound **5a** would also form two muoniated radicals, with Mu attached to P or C of the central P=C bond. Potential radical structures are as follows:

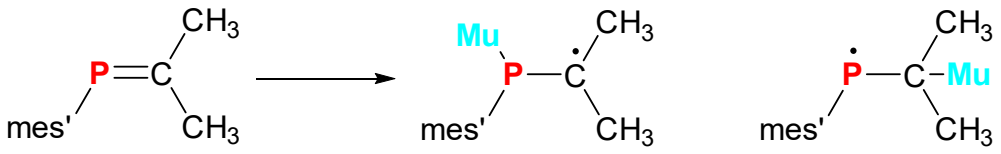

5a **5a-P-Mu** **5a-C-Mu**

Figure 5-2: Potential muoniated radicals formed from 5a.

TF-μSR spectra were collected at 273 K, 298 K and 320 K in 14.45 kG field. Three pairs of signals were detected in the spectrum (figure 5-3). The corresponding muon hfcs are listed in table 5-1.

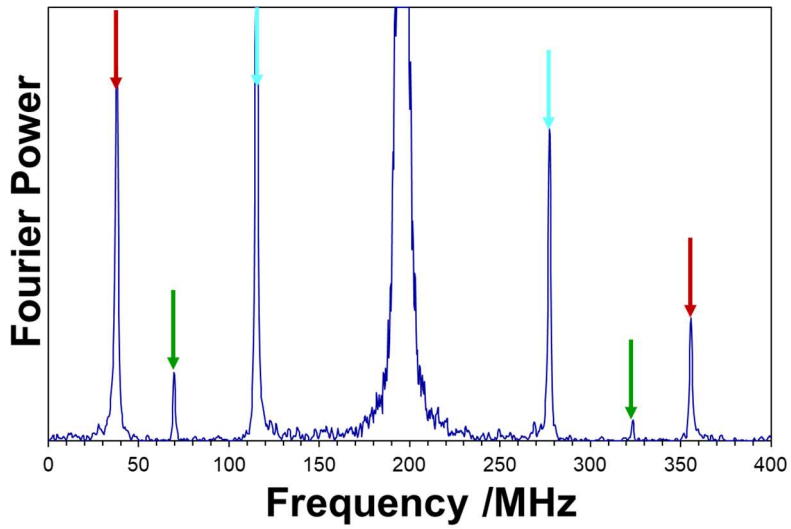

Figure 5-3: TF-μSR spectrum of muoniated radicals from compound 5a at 298 K. Pairs of signals from each radical are located equidistant from the central signal and are marked with colour coded arrows.

Table 5-1: Experimental muon hfcs (A_μ/MHz) of the muoniated radicals formed from 5a

Radical	273 K	298 K	320 K
1	321.7 (0.3)	317.8 (0.4)	315.6 (0.3)
2	165.0 (0.1)	162.2 (0.1)	160.2 (0.2)
3	257.0 (0.3)	253.4 (0.4)	251.0 (0.2)

Two pairs of signals have high amplitude. The outer signal pair with muon hfc 317.8 MHz is in the range of typical P-muoniated radicals, similar to the chapter 4 radical **4a-P-Mu**. The signal pair with hfc 162.2 MHz is in a similar range to the **4a-C-Mu** radical (135 MHz) and could be hypothesized to be from the **5a-C-Mu** radical. To give further insight into the muoniated radicals, ALC-μSR experiments were also conducted on the liquid sample of **5a**. The magnetic field was swept from 0.1 kG to 20 kG to search for resonances.

In the ALC-μSR experiments signals were observed in two regions spanning 5.5 kG–8 kG and 13 kG–14.5 kG (figure 5-4). The number and the shapes of the observed resonance signals for **5a** appear to be similar to the spectral data obtained for compound **4a**. The two signals at lower field are consistent with the ^{31}P signal we observed for the muoniated radicals formed from compound **4a**. Similar to chapter 4, assuming $A_\mu > A_{k,}$ we assigned the signal at 6.5 kG to the TF-μSR signal with muon hfc 321.7 MHz and the ^{31}P hfc obtained is 167.5 MHz at 298 K. This value is in close agreement with the ^{31}P hfc of the **4a-P-Mu**. This further implies the observed radical could be **5a-P-Mu.** The single resonance at 13.7 kG is similar to the proton signal of **4a-P-Mu** and can be attributed to the freely rotating CH_3 group protons of the **5a-P-Mu** radical.

Assigning the second ^{31}P resonance to the TF-μSR signal with muon hfc 162.2 MHz, we deduce that the ^{31}P hfc is 326.9 MHz. This large hfc is similar to those of phosphinyl radicals. Hence, we postulate this muoniated radical could be due to Mu addition to the C center where it produces a phosphinyl radical. The table 5-2 summarizes the hfc data obtained by ALC-μSR.

Table 5-2: Hyperfine constants (MHz) determined from ALC-μSR data of muoniated radicals formed from 5a

Radical	Site	A_μ	A_k		
		273 K	273 K	298 K	320 K
5a-P-Mu	***P***Mu	321.7(0.3)	163.5(0.1)	167.5(0.1)	163.9(0.1)
5a-P-Mu	C***H₃***	321.7(0.3)	58.9(0.1)	59.2(0.1)	58.8(0.1)
5a-C-Mu	***P***Mu	165.0(0.1)	326.9(0.1)	317.6(0.1)	317.6(0.1)

(a)

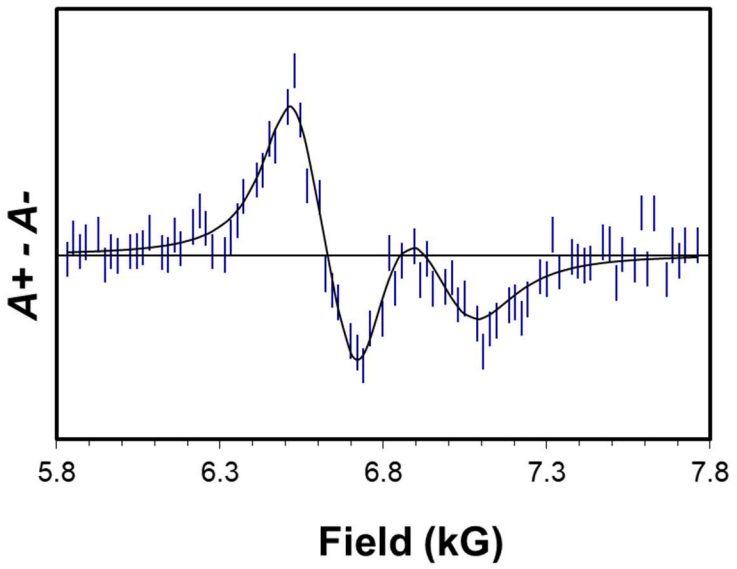

(b)

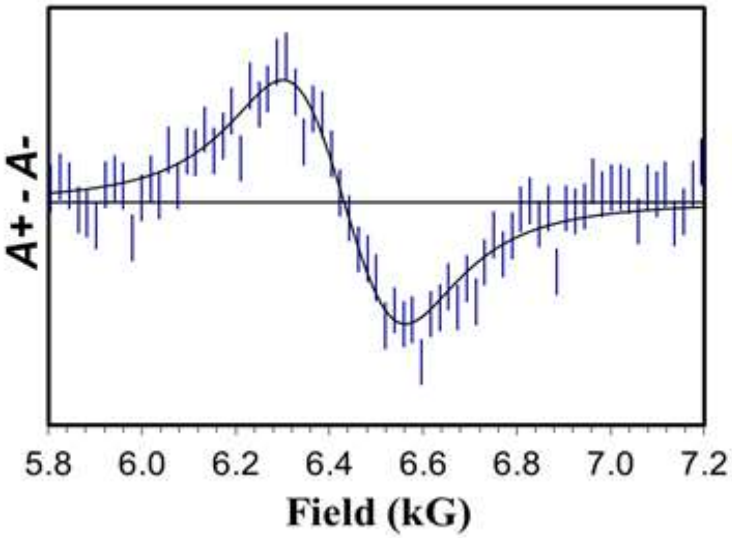

Figure 5-4: ALC-μSR spectra of muoniated radicals formed from 5a. (a) Two ^{31}P signals (b) Proton signal due to the 5a-P-Mu radical.

Considering the similarity to the hfc constants of the muoniated radicals formed from **4a** we can tentatively assign the radical with 321.7 MHz to **5a-P-Mu** and the radical with muon hfc 165.0 MHz to **5a-C-Mu**. For both radicals the hfcs are larger in comparison to the corresponding radicals formed from **4a**. This may be due to the electron withdrawing $(CF_3)_2$-mes groups reducing electron spin density towards the methyl groups attached to the C atom. These effects increase the unpaired electron

density on the muon in both **5a-P-Mu** and **5a-C-Mu radicals**. The small amplitude signal has a muon hfc of 253.7 MHz, which is similar to the muon hfc of **4b-CH_2-Mu** reported in chapter 4. The starting material for the synthesis of **5a** is the isomeric phosphaalkane **5a′**. We hypothesize that the final **5a** sample may be in equilibrium with its phosphaalkene isomer and the small intensity signal is due to **5a-CH_2-Mu.**

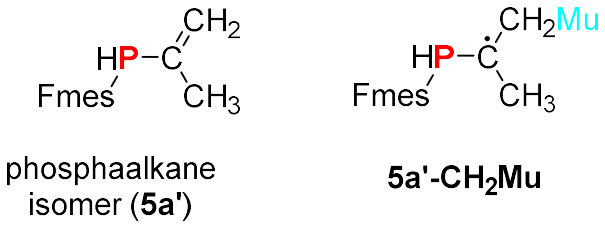

phosphaalkane isomer (**5a'**)

5a'-CH_2Mu

In chapter 4 we noted that the muon hfc of **4a-P-Mu** falls with temperature. The same trend has been observed for **5a-P-Mu** radical as well. A study was done by Roduner et al.,[13] on the temperature dependence of the muon hfc in the tert-butyl radical. In the most stable conformation the C-Mu bond eclipses the orbital containing the unpaired electron. With increase in temperature, increased vibrational motion results in an average conformation with reduced overlap. A similar effect has been observed for the P-Mu radical.[103]

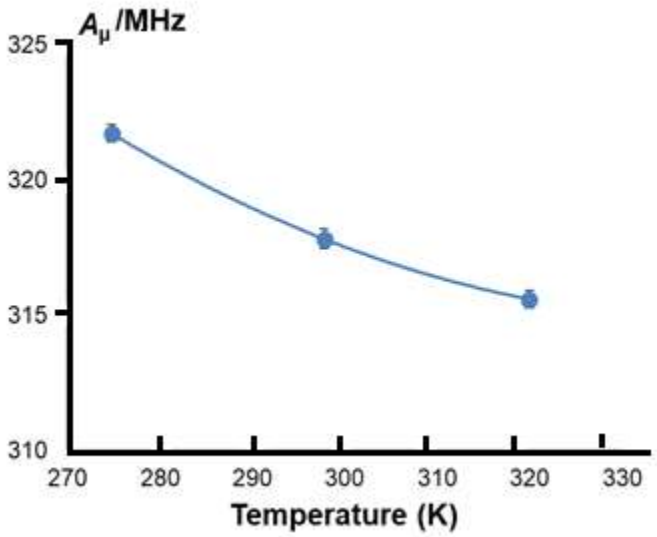

Figure 5-5: Temperature dependence of the muon hfc for 5a-P-Mu. The line through the points is to guide the eye only.

5.3.2. Computational results

To further support radical assignment, we carried out computational calculations. These were conducted using the UB3LYP method and 6-31G(2d,p) basis set. Calculating the vibrational average for all the vibrational modes using the **Anharmonic** keyword proved to be increasingly time-consuming as the complexity of the molecule increased and the job would often give unreasonable results or fail outright. The stretching vibrational frequency for P-Mu is 9407 cm^{-1}, sufficiently high to allow only the ground state to be populated. However, the torsional motion of P-Mu and C-Mu is primarily due to low-frequency vibrations at 162 cm^{-1} and 109.2 cm^{-1} respectively. Therefore, the Boltzmann-weighted average of the hfc of the rotamer around the P-C bond was calculated for both P-Mu and C-Mu radicals.

Table 5-3: Experimental and calculated hfcs (MHz) of 5a muoniated radicals

Radical	Site	Exp. (298 K)	Calc. (298K)
5a-P-Mu	P***Mu***	317.8	318
	PMu	167.5	216
5a-C-Mu	C***Mu***	165.0	181
	PH	324.9	213
5a'-CH_2Mu	CH_2***Mu***	253.4	230
	PH	–	136

The most exciting observation in this experiment is the drastic change in the ratio of the **5a-P-Mu** and **5a-C-Mu** radical yield. We have compared the relative energies of the optimized radical structures to explain this phenomenon. They are shown below.

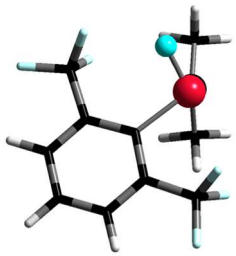

Δ*E* =0 kJ/mol

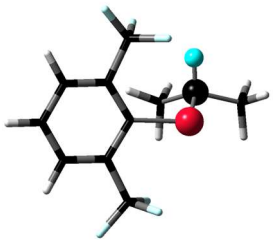

Δ*E* =-65 kJ/mol

Figure 5-6: Optimized structures and relative energies of (a) 5a-P-Mu (b) 5a-C-Mu. The Mu atoms are marked in cyan, P red, C black and H white.

(a)

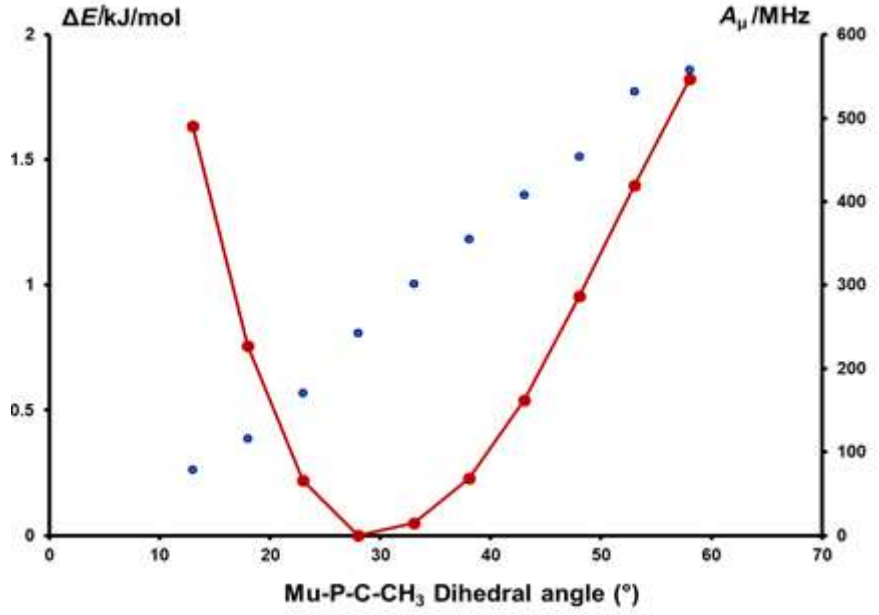

(b)

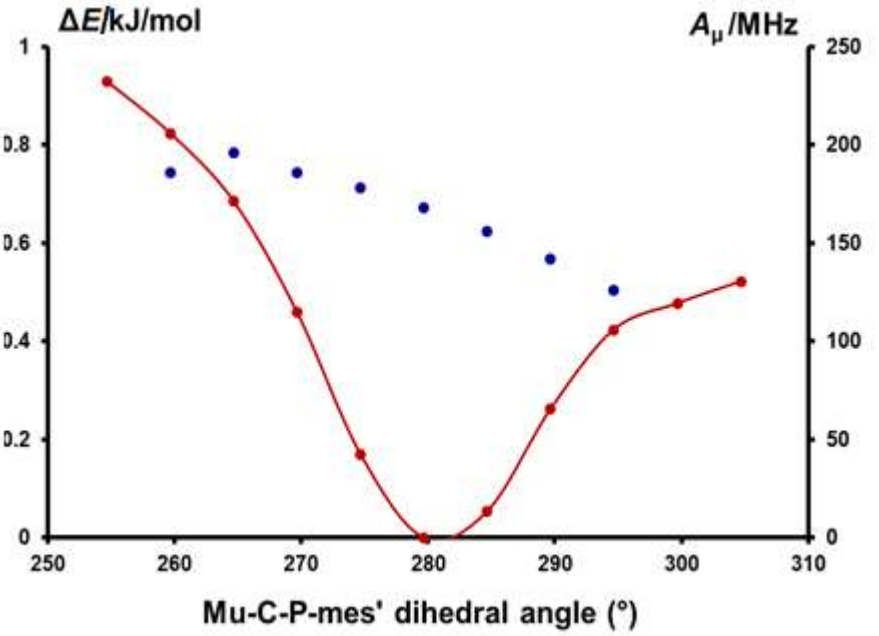

Figure 5-7: Potential energy curves (red, left-hand axis) for rotation around the P-C axis and corresponding hfc constants for each rotamer (blue, with scale on right-hand axis). (a) Mu-P-C-CH$_3$ (b) Mu-C-P-C.

The increase in **5a-C-Mu** radical formation can be attributed to the stability of the formed radicals and the polarity of the parent **5a** molecule. As shown in figure 5-6 the **5a-C-Mu** radical is significantly more stable than the **5a-P-Mu** radical. The stability of **5a-C-Mu** increases due to increased delocalization of the unpaired electron to the phenyl ring due to CF_3 groups being attached to the phenyl ring to stabilize the radical. Transition state calculations using the QST3 method show both radicals being formed through barrierless reaction pathways, and therefore increased formation of the more stable product **5a-C-Mu** was observed. The non-polar nature of P=C double bonds with alkyl or aromatic substituent groups has been attributed to opposing forces, namely the difference in electronegativity between P and C atoms, and the lone-pair back bonding.[40] However, attachment of the electron-withdrawing substituent (CF_3-Ar) to the P=C bond results in increased polarity. This was indicated by an increase of negative charge on the P atom **5a** compared to **4a**. Therefore, Mu addition to the C center is more favored. We can predict that phosphaalkene polymerization *via* a radical initiation route can be completely altered by the electronegativity of the substituent group. Therefore, looking back at the questions we formulated at the beginning of the chapter, we can conclude that electronegativity of substituent groups significantly affects the radical initiation process. Introducing electronegative substituent groups leads to multiple sites of addition which can result in a decrease of the efficiency of overall polymerization. However, it also opens up new potential paths of polymerization by formation of phosphinyl radicals.

5.4. What about selective muoniation of the P center?

Addition of electronegative groups increases muoniation of the C center, but how about the possibility of selectively muoniating the P center? Controlling the initiation product is a means to control the overall polymerization process and to increase its efficiency. It has been found that in certain cases of polymerized phosphaalkenes, where a mesityl group is attached to the P atom, propagation occurs a *via* methyl group in the mes group rather than directly to the P-C backbone.[104] This can result in the generation of branched polymers. Therefore, it would be interesting to investigate monomer routes that can avoid methyl activation and can directly propagate through the P=C backbone.

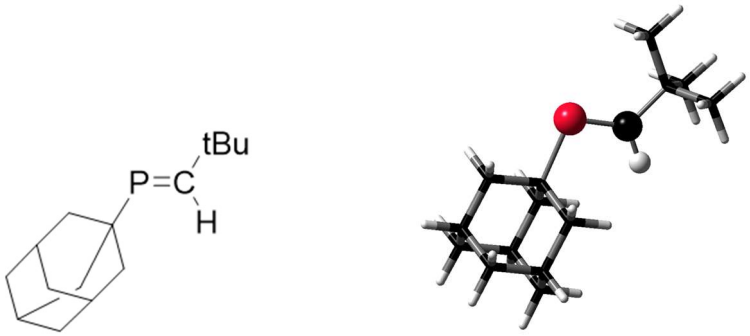

Figure 5-8: The structure of Ad-P=CHtBu (5b). The 3D structure was optimized with the UB3LYP/6-31(2d,p) basis set.

5b is a good candidate for this study as the adamantyl ring cannot undergo CH_3 group activation unlike mes groups. In addition, the bulky adamantyl group has minimal effect on the polarization of the P=C double bond.

5.4.1. μSR results

The TF-μSR experiments were conducted for temperatures 298 K (figure 5-9) and 320 K at 14.45 kG magnetic field.

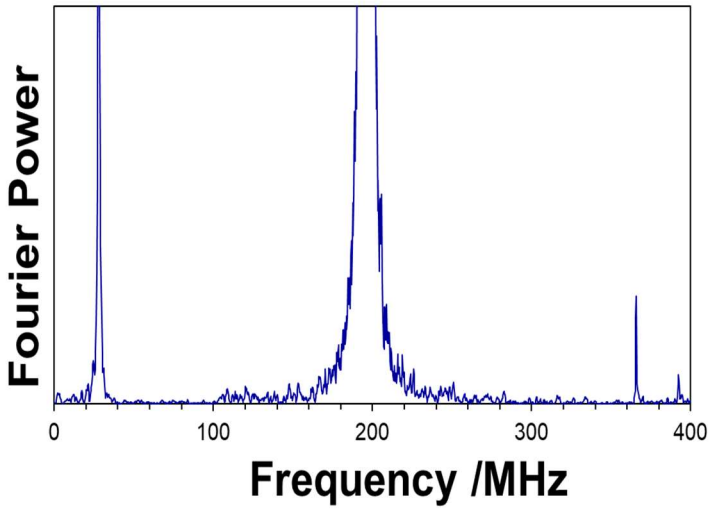

Figure 5-9: TF-μSR spectrum of 5b at 298 K and 14.45 kG. The central diamagnetic peak is at 196.5 MHz with an overtone at 393 MHz.

The muon hfc constant is in the same range as previously observed for P-muoniated radicals. ALC-μSR studies were conducted at 298 K and 320 K ranging from

0.1 kG to 24 kG. Only a single signal was observed. The spectrum is displayed in figure 5-10.

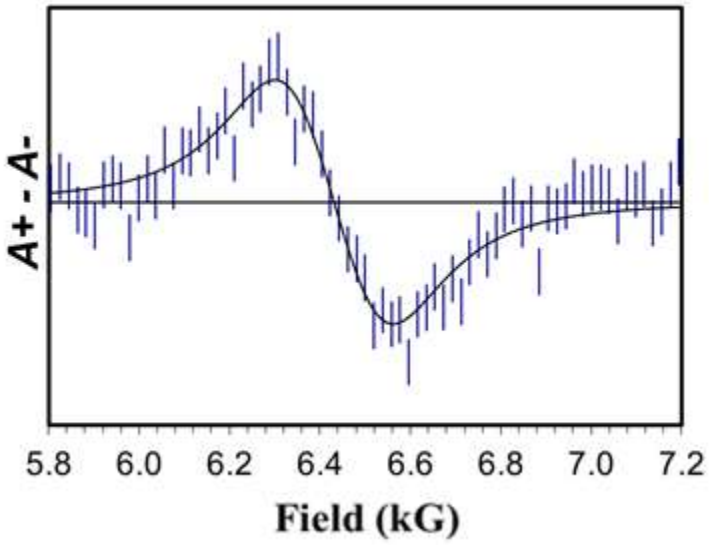

Figure 5-10: ALC-μSR spectrum of 5b muoniated radical at 298 K.

The resonance at 6.5 kG can be readily assigned to ^{31}P as the alternative assignment to proton gives an unreasonable value. In addition, the width of the signal is compatible with the ^{31}P signals previously observed. However, no proton resonance was observed.

5.4.2. Computational calculations

In order to unambiguously identify the muoniated radical formed, computational calculations were carried out, where structures of **5b**, **5b-P-Mu** and **5b-C-Mu** were optimized using the UB3LYP method and the 6-31G(2d,p) basis set. The torsional motion of the P-Mu bond of **5b-P-Mu** and the C-Mu torsional vibration of the **5b-C-Mu** radical are 158 cm^{-1} and 67 cm^{-1} respectively. The hfc constants of both radicals were calculated by taking the Boltzmann average of rotamers around the P-C axis. The Boltzmann weighted average of populated energy levels were considered for vibrational averaging.

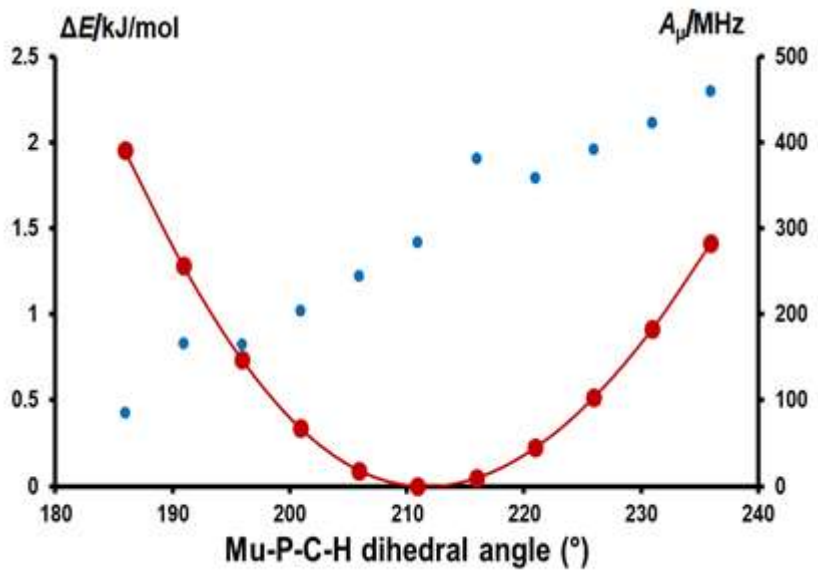

Figure 5-11: Potential energy curve (red) for rotation about the central P-C axis of Mu-P-C-H and the corresponding hfc constants for each rotamer (blue).

The computed hfc constants of the **5b-P-Mu** radical agreed with the observed experimental results, supporting the assignment of Mu addition to the P center.

Table 5-4: Experimental and calculated hfcs (MHz) of 5b muoniated radicals

		exp. hfc at 298 K	exp. hfc at 320 K	calc. hfc at 298 K
5b-P-Mu	P***Mu***	341.60(0.16)	337.80(0.10)	320
	PMu	183.20(0.04)	184.80(0.04)	190
	C***H***	–	–	-40
5b-C-Mu	C***Mu***	–	–	147
	CMu	–	–	142

Unlike the previous phosphaalkenes, no Mu addition was observed on the C center. In generally Mu behaves like H in addition across double bonds. In phosphaalkenes with aromatic groups attached to the P atom such as **4a** and **5a,** the HOMO electron cloud is evenly distributed over the P=C bond. In contrast, the optimized structure of **5b** shows (figure 5-12) that the HOMO electron density is more localized on the P atom compared to compounds **5a** and **4a**. According to our calculations using the UB3LYP method, Mu addition to both the C and P centers appears to be barrierless. However a study done by Kobayashi et al.[105] on Mu addition to C=S showed similar

results at the UB3LYP level but employing the more accurate CCSD(T) theory and multi-reference second-order perturbation theory (CASPT2) showed a small activation barrier for addition to the C center and the barrier height varied with the substituent groups attached to the C=S. Macrae et al.[106] also studied Mu addition to C=S and confirmed Kobayashi's results. We postulate that a similar phenomenon also occurs for Mu addition to **5b**.

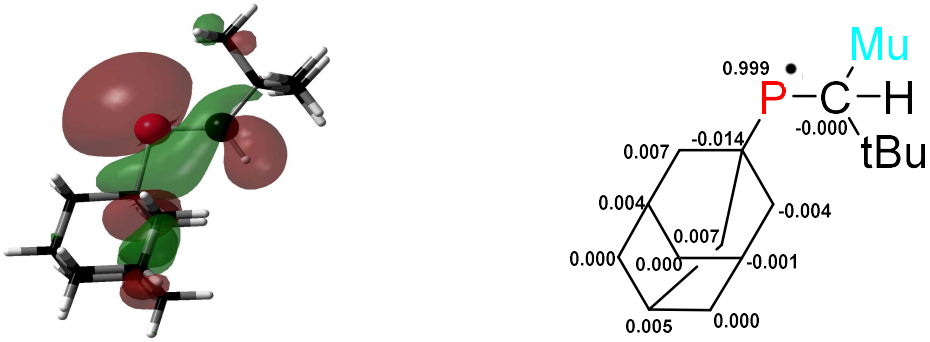

Figure 5-12: Iso surface of the HOMO of the 5b-C-Mu radical.

In addition, unlike the case of aromatic substituents, the unpaired electron delocalization to the adamantyl group is minimal. For **5b-C-Mu** the Mulliken spin density on the β-C of the adamantly group is -0.014, compared to 0.118 for the β-C of the phenyl ring in **5a-C-Mu**, i.e. approximately 10 times larger, thus increasing the stability of the C-muoniated radical. When an aromatic ring is attached to P.

5.5. mesP=CPh$_2$

5.5.1. Introduction

Gates and co-workers have studied the addition polymerization of P=C double bonds.[67,68,107] mesP=CPh$_2$ (**5c**) was the first compound with a P=C double bond to be successfully polymerized *via* a radical addition route. It has an ideal balance of kinetic and thermodynamic stability. The compound readily produces polymeric material from cationic, anionic and radical initiators. The radical route was found to be quite effective at producing polymers with chain length averaging 6200 subunits. However, cationic initiators only provided molecular and oligomeric species.[40]

As the radical route was found to be highly effective in polymerization, numerous **5c** based copolymers and homopolymers were synthesized, such as styrene phosphaalkene copolymer, which can be used as a catalytic layer for Suzuki cross coupling,[68] and an isoprene and **5c** block copolymer that acts as a template for gold nano-particle synthesis.[107]

A mechanistic study of the polymer initiation step is required to better understand and control the reaction. ^{31}P NMR and EPR studies of the radical initiation step suggested formation of multiple products, but to date these products could not be isolated or unambiguously identified.[67] The microstructure of the polymer propagation step has been studied using ^{13}C NMR, and the results suggest that the chain elongation occurs through the *ortho*-CH_3 group in the mes substituent rather than directly through the P=C bond. This observation raises questions regarding the mechanism of the initiation step.

I. Does it occur when a radical initiator extracts an H atom from orho-CH_3?

II. Or is there radical addition to the P=C bond followed by rearrangement?

5.5.2. Results and discussion

We anticipated that Mu addition to **5c** at the P=C bond would result in generation of P- and C-muoniated radicals as described for the previous phosphaalkene species. Unlike previous phosphaalkenes where there is evidence for polymer chain elongation through the *ortho*-CH_3 group, there is potential for radical formation by Mu addition to the phenyl ring. Therefore, two questions draw our attention:

I. Confirming the site of Mu addition from the two possible sites – phenyl ring and P=C bond

II. If Mu adds to P=C bonds does it form P-centered or C-centered radicals?

The structures of potential muoniated radicals of **5c** are shown in figure 5-13.

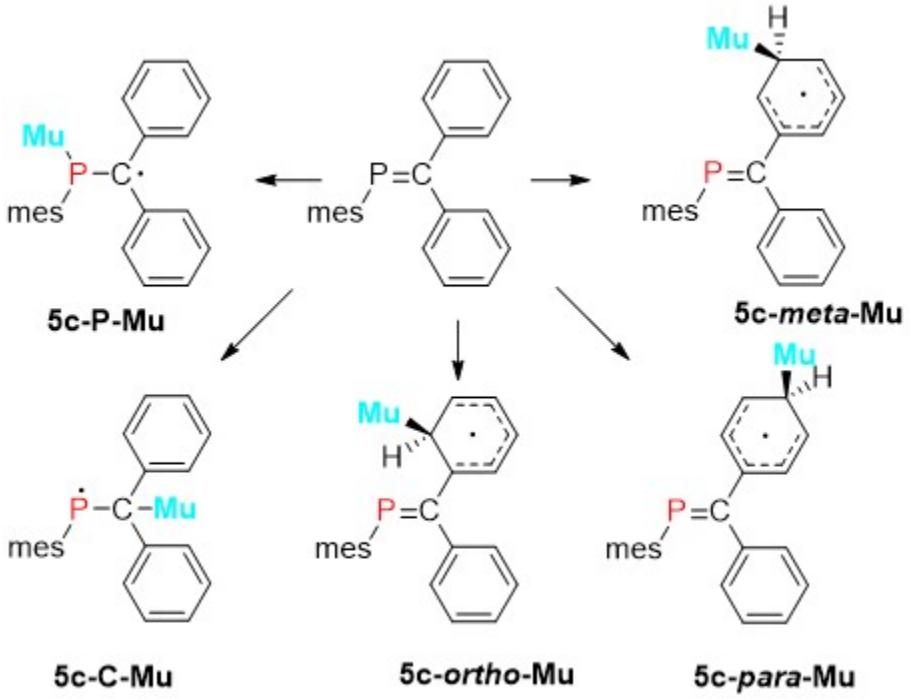

Figure 5-13: The potential muoniated radical structures of 5c.

The TF-μSR spectrum (figure 5-14) shows two signal pairs indicating formation of two muoniated radicals.

Table 5-5: Muon hfcs of two radicals formed from 5c as a function of temperature. Radical 1 is indicated by red arrows and radical 2 by green arrows in figure 5-14

Temperature (K)	A_μ/ MHz	
	Radical 1	Radical 2
277.4	173.6 (0.02)	97.3 (0.03)
298.5	174.0 (0.04)	96.4 (0.02)
320.0	175.8 (0.07	98.2 (0.04)

The relative intensity and the formation of two pairs of radicals are similar to what we observed for muoniation of the P=C bond of compounds **4a** and **5a**, and the ratio between the hfc constants is close to 2:1, similar to the P- and C-muoniated radicals formed from the other phosphaalkenes. However, the hfcs are markedly lower than those of the muoniated radicals of **4a** and **5a**.

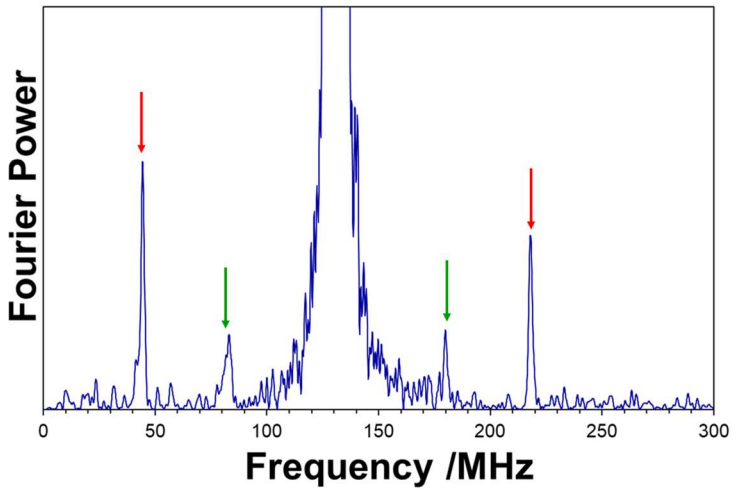

Figure 5-14: TF-μSR spectrum of 5c with 1.2 M concentration in THF solution at 10 kG magnetic field. The signal pairs located equidistant from the diamagnetic signal are marked with colour-coded arrows.

To answer the first question, we carried out a series of TF-μSR experiments. The hfc depends on the local spin density, which is highly sensitive to any changes in the local spin environment such as changes in substituent groups or changes in conformation. Considering these factors, we proposed studies of **5c** derivatives with electronegative groups attached to the phenyl rings. We supposed that addition of electronegative groups to the substituents would significantly alter the local spin density at the muon, and if Mu added to the phenyl rings, we would observe a significant change in muon hfcs. Compounds **5c-F** and **5c-OMe** were synthesized and purified at the Gates Lab in UBC. Their structures are shown in figure 5-15.

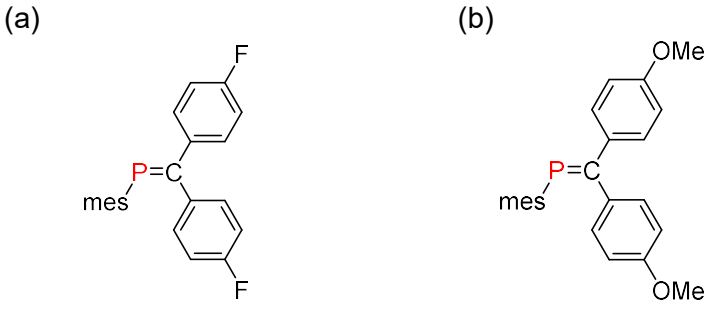

Figure 5-15: The structures of 5c derivatives with electronegative substituent groups attach to the phenyl rings: (a) 5c-F (b) 5c-OMe.

TF-μSR studies of both compounds were carried out in 14.45 kG magnetic field at 298 K The spectra obtained are shown in figure 5-16.

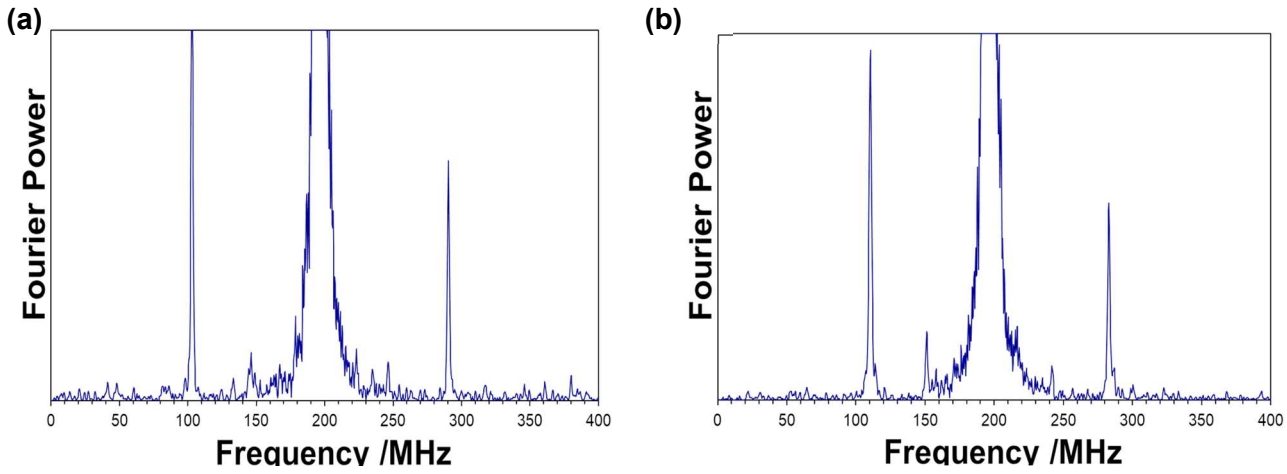

Figure 5-16: TF-μSR spectra recorded at 15 kG (a) 5c-F 0.5 M in THF at 298 K (b) 5c-OMe 0.4 M solution in THF at 298 K.

Table 5-6: Muon hfcs of 5c and its electronegative derivatives at 298 K

Compound	Radical	A_μ / MHz
5c	1	174.0 (0.02)
	2	95.4 (0.02)
5c-F	1	180.2 (0.07)
	2	98.2 (0.72)
5c-OMe	1	172.3 (0.10)
	2	101.5 (0.04)

There was no significant difference in the muon hfcs with the addition of electronegative groups at the para position in the phenyl ring. This indicates that the Mu atom does not add to ring C atoms. If Mu adds to the phenyl ring the effect of the electron-withdrawing groups OMe or F would significantly alter the muon hfcs. Since we have ascertained that the Mu does not add to the phenyl ring, we can safely assume Mu does add to the P=C bond.

To further investigate **5c** muoniated radicals, the hfcs of spin-active nuclei were investigated by ALC-μSR spectroscopy. Two samples of **5c** were used; the first sample was the original sample used for TF-μSR studies, and the second was one where the P=C carbon atom was enriched with ^{13}C. In the isotopically enriched sample ^{31}P and ^{13}C

are both expected to produce signals. Using an isotopically substituted sample provided additional information on the muoniated radical. In particular, if Mu adds to the P=C bond, ^{13}C would generate a strong signal in the ALC-μSR spectrum and the resulting hfc constant would provide additional information on the local spin density. Comparison of the ALC-μSR spectra of regular and isotopically-substituted samples allowed immediate identification of the ^{13}C signal, as the presence of any additional signal can be immediately attributed to the ^{13}C spin. ALC-μSR spectra of both samples are shown in figure 5-17. The ALC-μSR spectra of both samples were taken at 298 K, and the isotopically enriched sample was also studied at temperatures of 275 K and 320 K.

The broad signal around 2.2 kG in the original sample is attributed to ^{31}P The additional signal at about 4.1 kG in the isotopically substituted-sample corresponds to ^{13}C. In some circumstances the presence of two muoniated radicals makes it hard to assign a corresponding TF signal to an ALC-μSR resonance. However, in this case considering the signal amplitudes we can assign the observed resonance signal to the strong TF signal pair with muon hfc 174 MHz at 298 K. The hfcs of spin-active nuclei are recorded in table 5-7.

We performed ALC-μSR studies up to a magnetic field of 24 kG to look for additional signals, but none were found. The absence of any proton signals is additional evidence that Mu does not add to the phenyl groups, since cyclohexadienyl radical formation would have produced strong methylene proton signals.[27]

Table 5-7: ^{31}P and ^{13}C hfcs determined for the more abundant radical formed from 5c

Temperature	Nuclei	A / MHz
277.5	**Mu*P***	122.4
	P*C*	73.8
298.0	**Mu*P***	121.0
	P*C*	73.7
320.0	**Mu*P***	120.2
	P*C*	74.2

(a)

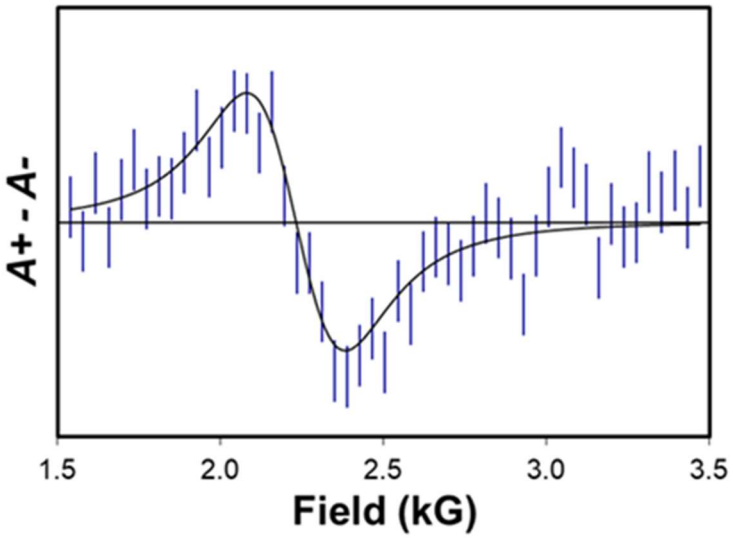

(b)

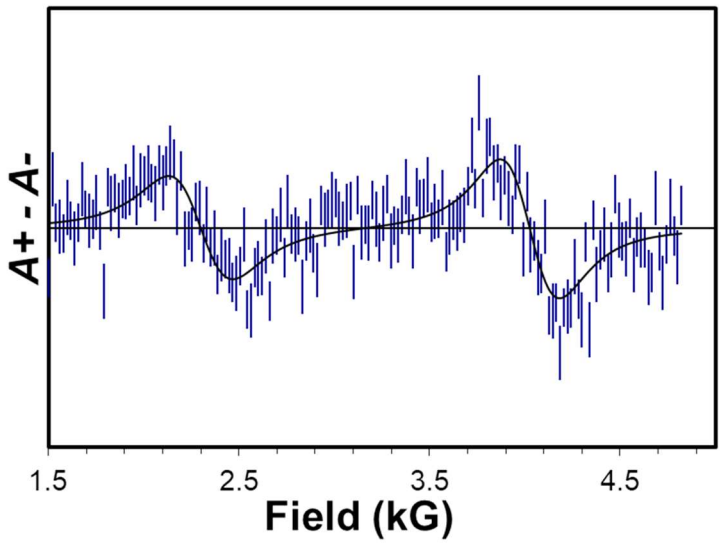

Figure 5-17: ALC-μSR spectra recorded at 298 K: (a) Original 5c 1.2 M solution in THF; (b) ^{13}C isotopically substituted sample 0.33 M solution in THF.

To confirm the identity of the muoniated radicals, computational calculations were done using the UB3LYP method and 6-31G(2d,p) basis set. Hfcs for **5c-P-Mu** and **5c-C-Mu** were calculated using Boltzmann averaging of rotamers around the P-C bond axis. The muon addition to the double bonds was calculated using the Boltzmann averaging method and the results are recorded in table 5-8.

Table 5-8: Calculated hfcs (MHz) of potential muoniated radicals formed from 5c

	μ	^{31}P	^{13}C
5c-P-Mu	50	70	92
5c-C-Mu	110	220	-80
5c-ortho-Mu	320	130	-35
5c-para-Mu	250	125	-34
5c-meta-Mu	34.7	135	76

The value of the smallest hfc of 96.4 MHz matches the calculated muon hfc of 92 MHz for the **5c-C-Mu** radical. It is evident that none of the calculated hfcs matches the experimental data for the outer signal pair. This was not unexpected as the increase in complexity of the molecule reduces the reliability of the hfc calculation. Two phenyl groups in a flapping motion make it difficult to successfully model the rotation around the P-C bond. More detailed study using the more accurate CCSD(T) theory could be carried out. However, with the size of the molecule this approach is computationally very expensive and extremely time consuming. In addition to the complexity of the molecule, calculations involving a Mu atom using methods developed for conventional atoms present their own problems. For example, the work by Goli et al.[108,109] indicates discrepancies of experimental and calculated hfcs of small atoms using the usual adiabatic framework.[52] In some cases there is a variation of up to 30-40% between experimental and calculated hfcs of muoniated species, such as in the Yamada et al.[110] work.

Since the calculated hfcs do not help in assigning the radical that produced the outer signal pair of the TF-μSR spectrum, we tried to deduce the identity of the radical empirically and determine if this radical is formed by Mu addition to the P atom.

One way to achieve this is by blocking the reaction center, in this case the P atom, using a bulky group. For this purpose, we employed phosphaalkene **5d** which has 1,3,5-tri-tert butylbenzene (mes*) as the substituent group attached to the P center. The bulkiness of the mes* group acts essentially as a shield blocking the P atom.

Figure 5-18: Structure of mes*-PCH_2 (5d) and the geometrically optimized structure at the 6-31G(2d,p) level.

We recorded the TF-μSR spectrum of **5d** at room temperature in 14.45 kG magnetic field. Only one pair of signals was observed; it appears similar to the C-muoniated radical signals observed in the previous compounds. For the first time in all the phosphaalkenes we studied, the other signal pair is absent. The loss of this strong signal by blocking the P center suggests that it is due to Mu addition to the P center. With these key observations we can conclude that the missing signal corresponds to P-Mu addition.

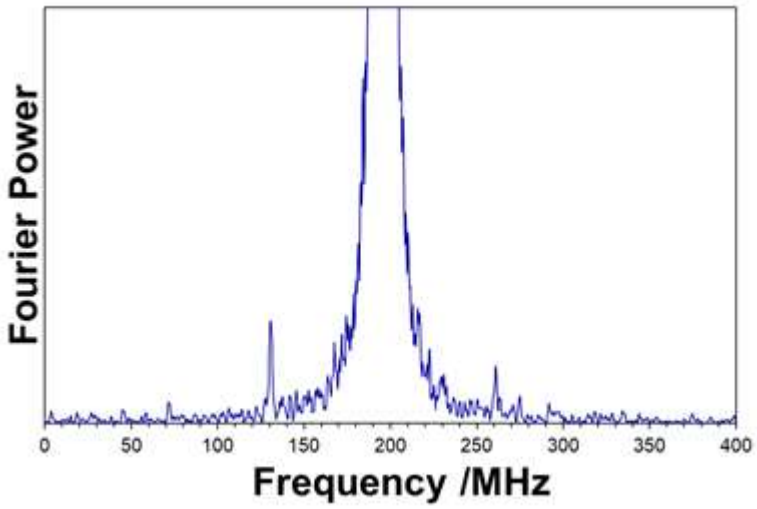

Figure 5-19: TF-μSR spectrum obtained from 5d with 1.2 M concentration in THF solution at 260 K.

Even though hfcs of the **5c-P-Mu** radical cannot be predicted with confidence, computational calculations can give an insight into the muoniated radical's structure and energetics. The structures of **5c-P-Mu** and **5c-C-Mu** radicals are shown in figure 5-20.

(a) **(b)**

Figure 5-20: Structures of (a) 5c-P-Mu (b) 5c-C-Mu radicals optimized at the 6-31G(2d,p) level.

It is worth noting that the orientation of the P-Mu bond in **5c-P-Mu** differs from that of the previous P-Mu radicals. Unlike in previous P-Mu radicals where P-Mu is eclipsed in this radical P-Mu shows a staggered conformation. This is due to steric effects of the phenyl substituents.

5.5.3. Temperature dependence of the 5c-P-Mu radical hfc

The temperature dependence of the muon hfc of the **5c-P-Mu** radical is shown in figure 5-21. It shows the opposite trend to the P-Mu hfcs observed in previous radicals. This can be explained by the **5c-P-Mu** equilibrium structure. In the **5c-P-Mu** optimized structure, unlike previous P-Mu radical structures the muon nucleus does not overlap the SOMO in the minimum energy structure. This could be due to steric hindrance of the phenyl groups and mes group. The bulkiness of the phenyl rings forces the bulky mes group to move further away and be in a staggered conformation from the phenyl rings. As the temperature is increased the muon hfc increases consistent with increased overlap of the P-Mu bond with the SOMO.

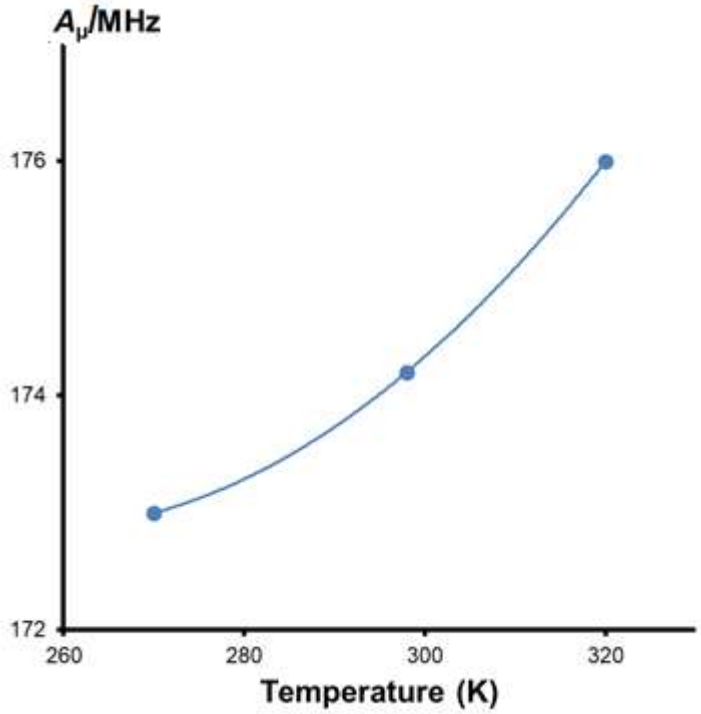

Figure 5-21: Temperature dependence of radical 5c-P-Mu of 5c. The curve through the points is to display the trend only. The error bars are smaller than the shapes representing the data points.

5.6. Conclusion

The results detailed in this chapter indicate that Mu addition to a P=C double bond is strongly influenced by altering the substituent groups attached to the P=C bond. Phosphaalkene's HOMO is highly susceptible to the substituent groups' electron withdrawing effects. We have empirically studied radical formation from **5c** which indicates that the neutral radical initiator Mu forms a P-Mu radical. This supports the hypothesis that the radical initiation step of the mesP=CPh_2 polymerization happens by a radical initiator adding to the P center. The primary radical can undergo rearrangement by proton migration from a methyl in the mes group. Subsequent polymer propagation steps can ensue through this secondary radical. This polymer propagation of mesPCPh_2 via methyl activation in the mesityl group was deduced by Tsang et al.[67] In addition, we have successfully investigated the role that substituent groups play in radical formation in P=C bond opening and explored an avenue to manipulate them to enhance the desired radical formation.

Chapter 6.

Triphosphabenzene radical chemistry – H atom reactions

6.1. Introduction

The mission to find low-valent analogues of multiple-bonded organic compounds has been a topic of interest in inorganic chemistry in the last few decades.[111] Low-valent organophosphorus compounds play a vital role in this new exciting area of study since low-valent P compounds present us with new oxidation states, electronic environments and ligand properties which are not available in their organic counterparts. The compound 2,4,6-tri-tert-butyl-1,3,5-triphosphabenzene (TPB) is in the family of phosphinines which are aromatic heterocycles (figure 6-1).

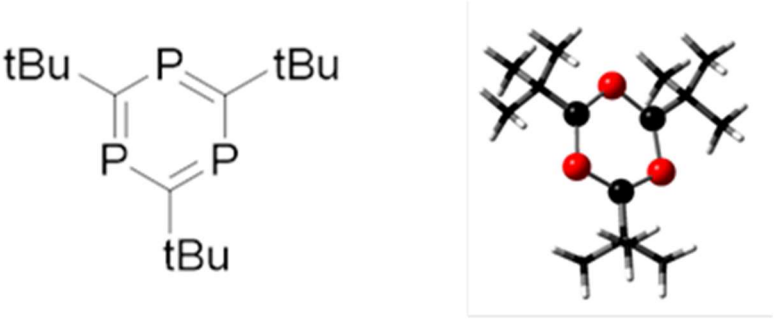

Figure 6-1: Structure of 2,4,6-tri-tert-butyl-1,3,5-triphosphophosphabenzene (left). The 3D structure of 2,4,6-tri-tert-butyl-1,3,5-triphosphophosphabenzene, as optimized using DFT calculations (right).

In the last decade, the study of TPB has gained momentum. TPB was first reported by Barron and Cowley as a TPB molybdenum complex.[113] With the discovery of a more convenient synthesis route by Tabellion et al.,[114] TPB became more available for detailed studies. The X-ray crystallographic studies conducted by Gleiter et al.[115] showed that the C_3P_3 central core of TPB is planar and the P-C bond lengths are equal, suggesting that TPB has aromatic properties. This was confirmed by ^{13}C NMR chemical shifts of TPB giving values which are typical for aromatic rings. It was deduced that TPB shows considerable aromaticity, on par with benzene and pyridine.

However, detailed studies on TPB show a far more diverse reactivity compared to species such as benzene or pyridine.[111,112] TPB shows high versatility in its reactivity, ranging from ring contractions to acting as a catalytic agent in small molecule reactions. TPB's η_6 ligand reactivity resembles other organic analogues such as benzene and pyridine. However, the inclusion of three P atoms in the ring provides ligand activity through directly binding to P atoms as a η_1 ligand. TPB forms metal-ligand complexes with metals such as gold and rhodium, to form complexes with catalytic applications in the hydroformylation of olefins. In addition, η_1 coordination has been observed in methylation, silylation, and protonation. TPB also exhibits ring contractions, which are quite rare in organic chemistry. These types of reactions are important for conversion of a highly stabilized aromatic ring system to a five-membered ring.

The most exciting part of TPB reactivity is its reactivity towards small molecules, which resembles the chemistry of transition metals, especially the reactions with H_2 and CH_4.[111] Hydrogenations are among the most important reactions involved in many industrial processes, such as crude oil refining and ammonia fertilizer production.[116] Currently, these processes use heavy metal catalysts, which are environmentally hazardous. However, realizing the potential of TPB to cleave molecular H_2 can provide a better alternative for these industrially relevant reactions.[117]

A paper by Longobardi et al. describes the direct uncatalyzed hydrogenation of TPB under mild conditions.[117] The reaction was monitored using NMR and it progressed through a 1,4-addition mechanism. Using isotopically labelled H_2 confirmed that both H atoms came from the same molecule, and that H_2 adds to TPB by a 1,4-addition mechanism. The most important aspect of this reaction is its reversibility. The addition reaction involves TPB ring distortion to a boat conformation (figure 6-2), which allows the H_2 molecule to approach TPB and align above it. The boat conformation of TPB increases the donor and acceptor capacity of the molecule, facilitating its addition across the TPB molecule. The reaction proceeds through a concerted mechanism to form bicyclic final products. The final products are a mixture of cis and trans products of triphosphabicyclo[3.1.0]hexadienyl.

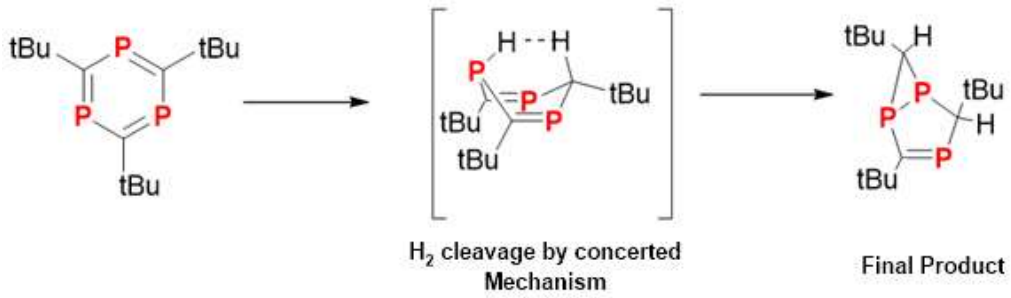

Figure 6-2: Proposed mechanism for hydrogenation of TPB via an addition route (Longobardi et al.)[117]

In view of the concerted mechanism of the hydrogenation, we hypothesized the possibility that a radical route for hydrogenation can also exist. Production of H· atoms and observation of TPB's reaction would be the ideal way to observe the reactivity. However, generating H atoms without side products has proven to be difficult. An alternative is to use muonium.

There is no information on potential radicals of TPB or their conformations, configurations and reactivity. We aim to address this void of information on the radical reactivity of this fascinating compound and investigate a potential radical route for the hydrogenation.

6.2. Results and discussion

6.2.1. Experimental studies

The muon irradiation of TPB dissolved in hexane yielded the TF-μSR spectrum in figure 6-3. Two pairs of radical signals can be seen symmetrically placed on either side of the diamagnetic signal. The presence of two signal pairs indicates the formation of two muoniated radicals having muon hfcs of 306.1 MHz and 35.6 MHz. The diamagnetic signal is observed at 196 MHz and is much stronger than the radical signals and hence is truncated in this display. The muon hyperfine coupling constants are significantly lower than the value observed for Mu addition to benzene.

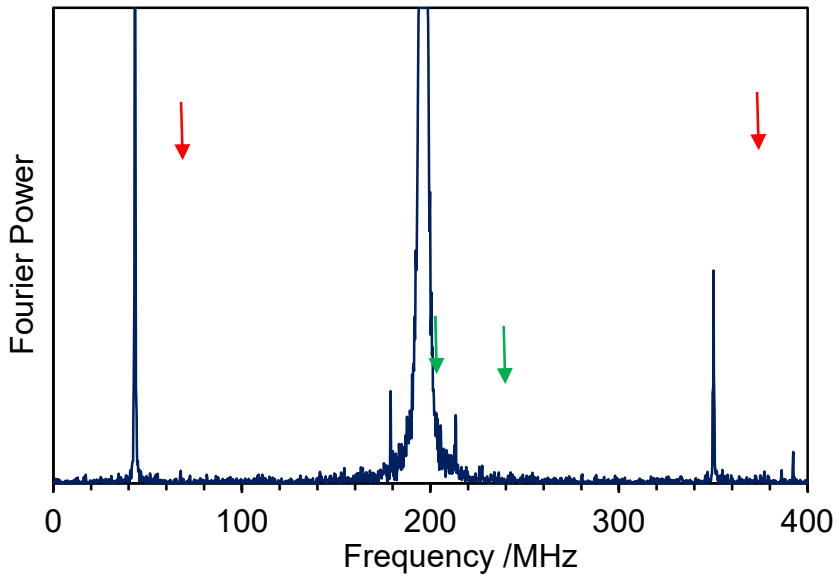

Figure 6-3: TF-μSR spectrum of muoniated radicals formed from TPB at 298 K. Each radical exhibits a pair of precession frequencies, as shown by the colour coded arrows. The signal located at 392 MHz is the overtone of the diamagnetic signal.

The outer pair of peaks is higher in intensity and the signal is long-lived and does not oscillate in amplitude. This indicates that the corresponding radical is formed quickly and is relatively stable. The amplitude of the weaker signal pair oscillates with the delay time of the Fourier transformation. This is an unusual feature compared to the majority of TF-μSR signals we have observed in the past. The delayed formation and the low intensity of the radical could be due to a secondary step in radical formation. However, in order to explain the curious feature of the oscillation of the signal intensity requires further studies. The muon hfcs of both radicals are recorded in table 6-1. The muon hfcs of the radicals show opposing temperature dependence. This will be explained later in this chapter.

Table 6-1: Experimental muon hfcs (MHz) of the muoniated radicals formed from TPB

Temperature (K)	1	2
273	302.8(0.3)	38.7(0.3)
298	306.1 (0.1)	35.6(0.1)
320	309.1 (0.1)	34.4(0.1

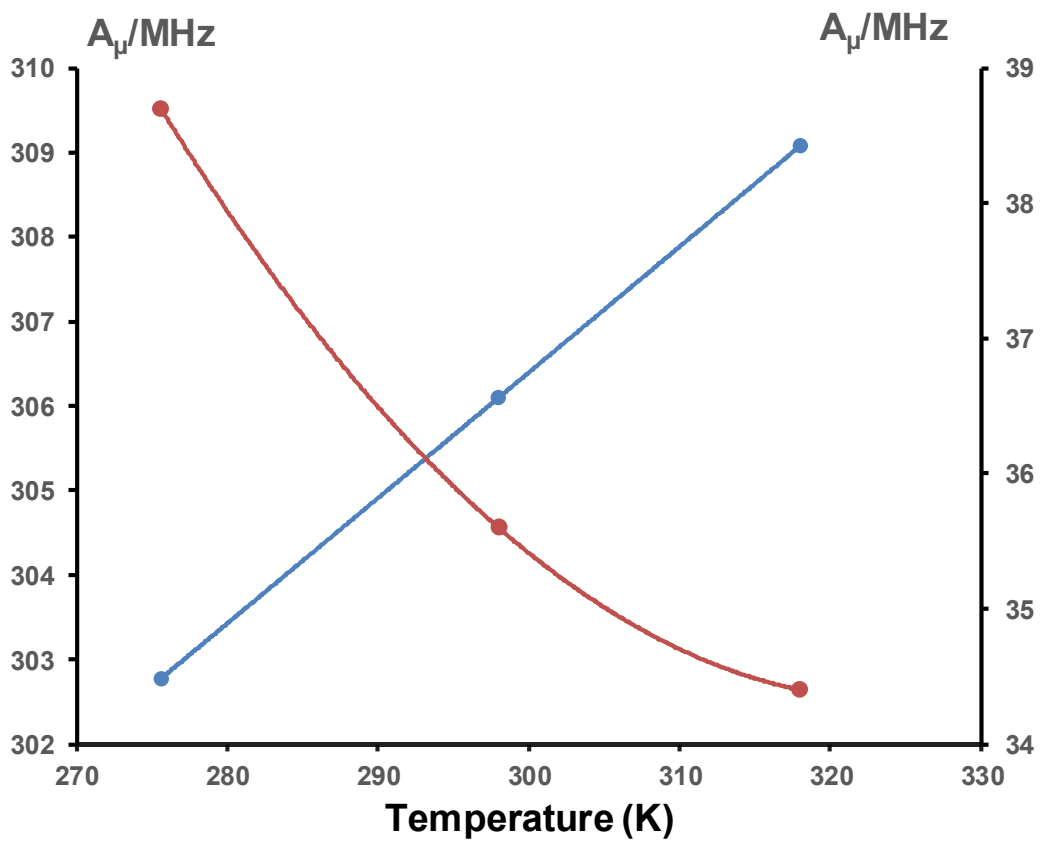

Figure 6-4: Temperature dependence of the TPB muoniated radicals: radical 1 (blue) radical 2 (red). The lines are guides for the eye only. The error bars are smaller than the shapes representing the data points.

The ALC-μSR technique was applied to determine the hfcs of other spin-active nuclei. There are multiple ^{1}H and ^{31}P spin-active nuclei present in the muoniated radicals formed by TPB, and they can all give rise to ALC resonances. However, the core of the TPB does not have any protons attached. Therefore, in the case of Mu reacting with the ring, no proton signals are expected. The ALC-μSR spectrum of TPB consists of two resonances in the range 1.2 kG to 2.9 kG (figure 6-5). These signals are similar to previously observed signals for ^{31}P nuclei.

In principle, there is an ambiguity of ascertaining which ^{31}P signals correlate to which signal pair in the TF-μSR spectrum. But in practice, the relative TF signal amplitude compared with ALC-μSR signal amplitude and the ratio of muon hfcs assist in this assignment. The stronger signal is assigned to the strong TF-μSR signal pair and the ^{31}P hfc obtained is 237.5 MHz. The smaller ALC-μSR signal at 1.2 kG resonance field is assigned to the smaller TF-μSR signal and the hfc calculated is -65 MHz.

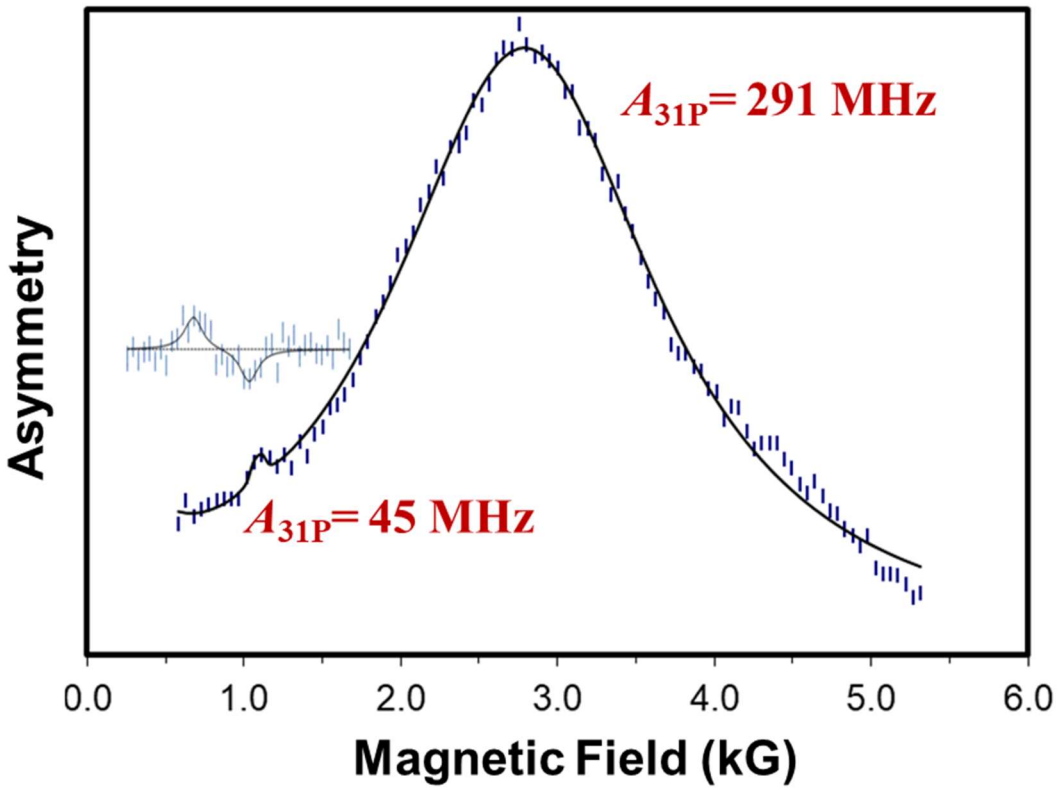

Figure 6-5: ALC-μSR spectrum without field modulation obtained from 2,4,6-tri-tert-butyl-1,3,5-triphosphabenzene at 298 K. The inset shows a scan of the small signal using field modulation.

6.2.2. Computational studies

Inspection of the TPB structure shows two potential muonium addition sites leading to a P-muoniated radical **TPB-P-Mu** and a C-muoniated radical **TPB-C-Mu**, In order to assign the hfc constant to potential radical structures, theoretical calculations were carried out using the UB3LYP method and the 6-31G (2d,p) basis set. The TPB structure was optimized and the result was tested by comparing bond lengths and bond angles with the existing crystallographic data by Gleiter et al.[115] The optimized structure has equal C-P lengths of 1.737 Å and bond angles P-C-P = 129.6°, C-P-C = 109.9° (cf crystallography data 1.727 Å, 129.4°, and 109.6°, respectively).

(a) (b)

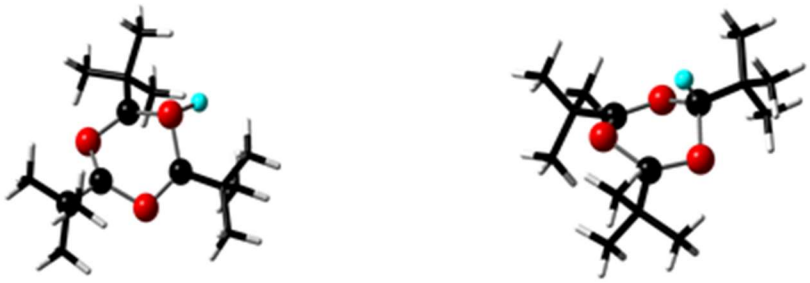

Figure 6-6: Optimized structures of TPB muoniated radicals (a) TPB-P-Mu (b) TPB-C-Mu.

The **TPB-P-Mu** and **TPB-C-Mu** structures were optimized, and vibrationally-averaged hyperfine coupling constants at 298 K were calculated over an anharmonic potential surface, as reported in table 6-2.

Table 6-2: Experimental and calculated hfcs (MHz) for the possible Mu adducts of TPB at 298 K

Radical	Nucleus	*Exp.*	*Calc.*
1	P*Mu*	306.1 (0. 1)	291
	*P*Mu	237.5(0.5)	254
2	C*Mu*	-	178
	C*P*	-	45
3	C*Mu*	35.6(0.0)	
	*P*C	9.6(0.0)	

The predicted value of 291 MHz roughly matches the radical **1** with hfc of 306.1 MHz. The optimized structure of **TPB-P-Mu** has a boat conformation with P-Mu protruding out of the ring plane. NBO calculations of **TPB-P-Mu** indicate that the unpaired spin density is located primarily at the C atoms adjacent to the P-Mu. Incorporating vibrational averaging into the calculation significantly increased the hyperfine coupling constant of the muon in **TPB-P-Mu**. This can be correlated to the wagging and stretching vibrational modes of P-Mu bonds, which bring the muon nucleus closer to the unpaired spin density, thereby increasing the muon hfc.

There is no agreement between the predicted hfc for **2** and the experimental values. Intrigued by this discrepancy we explored possible rearrangements of radical

TPB-C-Mu. The small hfc of (-)35.6 MHz and possible delayed formation of this radical suggests a rearrangement that results in the unpaired electron density further from the muon nucleus. As mentioned earlier, Longobardi et al.[117] suggested a mechanism for TPB activation of H_2 that results in fused three and five-membered rings. We propose that **TPB-C-Mu** can undergo rearrangement to a similar bicyclic structure as shown in figure 6-7.

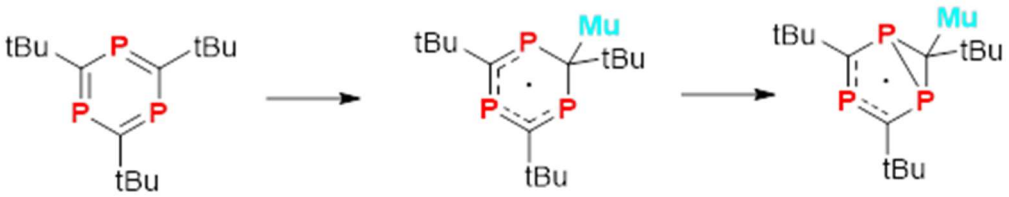

TPB **TPB-C-Mu** **3**

Figure 6-7: Proposed formation and rearrangement of TPB-C-Mu.

The bicyclic secondary muoniated radical structure is the first of its kind observed by muon spectroscopy. Structure **3** can be used to explain the temperature dependence observed for the radical **3** signals, as displayed in figure 6-4. The optimized structure **3** shows the muon nucleus at the axial position of the bicyclic structure. EPR studies on bicyclo radicals showed a decrease in long-range hfc interactions such as in hfcs of γ protons.[120] For structure **3** increased temperature results in increased wagging of the C-Mu substituent, and this leads to flattening of the overall ring structure so that on average the muon nucleus has less overlap with the SOMO.[27]

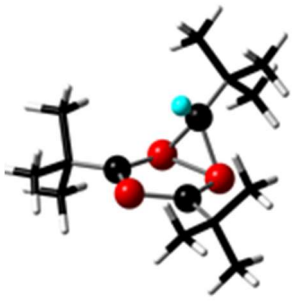

Figure 6-8: Optimized structure of 3.

To provide insight into the underlying mechanism of muoniated radical formation we modeled the reaction pathway, utilizing 2,4,6-tri-methyl-1,3,5-triphosphabenzene (TPB′). For these calculations, a more economical 6-31G(d,p) basis set was used.

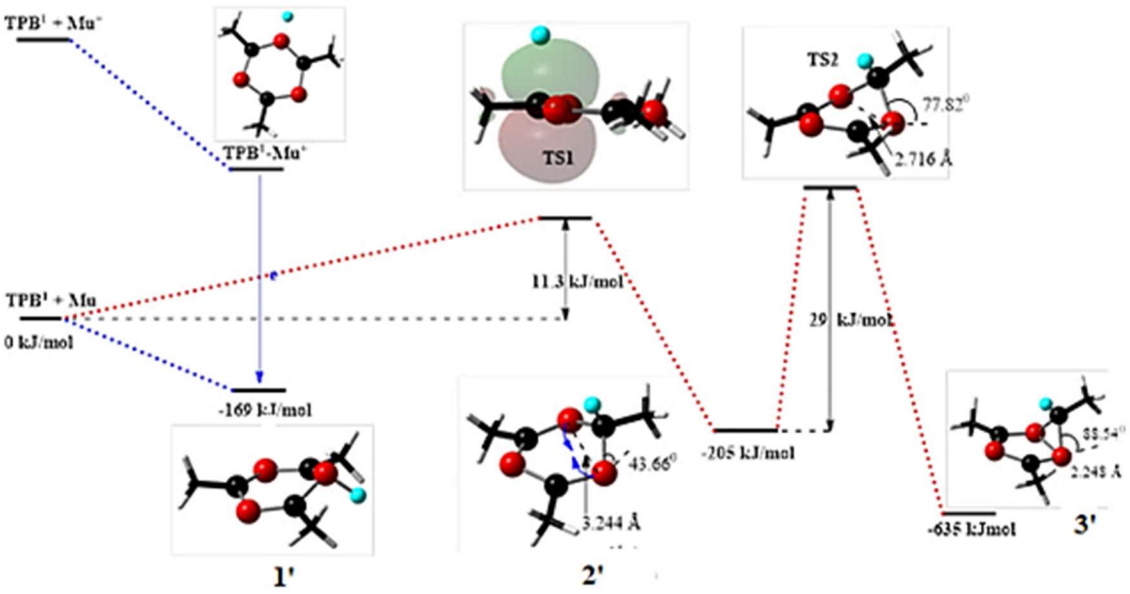

Figure 6-9: Potential energy surface of 1' and 2' radical formation, via two pathways (blue), while the formation of 3' occurs in a two-step reaction (red).

In work done by Zhang et al.[118] it was determined that the TPB molecule protonates at the P atom forming a planar cation, hence we hypothesize that both Mu and Mu^+ can react with TPB. When Mu^+ reacts with TPB the ion can also acquire an electron from the solution to undergo charge neutralization producing a neutral radical. Thus, there could be two different reaction paths to produce the final muoniated radical. We can predict Mu^+ addition at the P atom and disregard addition to the C atom. In previous studies by Zielinski et al.[119] for a wide range of phosphinines, it was determined through calculation that the protonation occurs through a proton capture mechanism without an activation energy barrier. The paths to produce the final muoniated radical are as follows.

$$TPB' + Mu \longrightarrow TPB'\text{-}Mu \qquad (6.1)$$

$$TPB' + Mu^+ \longrightarrow TPB\text{-}Mu^+ \xrightarrow{e^-} TPB'\text{-}Mu \qquad (6.2)$$

TPB' exhibits a similar barrierless fast proton capture and produces a planar **TPB'-Mu$^+$** ring. **TPB'-Mu$^+$** retains a planar structure that indicates that aromaticity of the ring structure is retained, but **TPB'-Mu$^+$** is less stable than **1'**. Subsequently, **TPB'-Mu$^+$**

abstracts an electron to form a stable P-muoniated radical. Mu addition at the P-center of **TPB'** also proceeds via a barrierless addition pathway. The lack of an activation barrier in the two routes results in fast formation of the radical and high-intensity of the TF signal. It is notable that the P-muoniated radical is less stable than the C-muoniated radical and yet it gives a higher intensity signal in the TF-μSR spectrum.

As shown in figure 6-10 Mu atoms approach the **TPB'** ring from an out-of-plane direction and attach to the C center to form the C-muoniated radical. The transition state (TS1) consists of a loosely bound **TPB'-Mu** complex. IRC calculations were done to confirm the transition state. In TS1 the **TPB'** ring does not show significant distortion and the P-C bonds of the ring are slightly elongated. The intermediate **2'** is in a boat conformation and Mu is in an axial position. Wagging (209 cm^{-1}) of the two P centers that are adjacent to the muoniated C brings them closer to each other. The closer proximity of two P atoms leads to TS2. At TS2 the ring is further distorted out of the plane, bringing the two P atoms even closer (2.716 Å). Moreover, C_2P_3 forms a planar unit while C-Mu maintains an out-of-plane configuration. The **2'** intermediate forms a stable bicyclic final product. The potential energy pathway is consistent with assignment of the low-intensity radical signal pair (-33 MHz) to the muoniated radical **3**.

Mu^+ addition at a C atom has not been investigated for C-muoniated radical formation because it is known that a proton predominantly adds to a P atom. The trajectory of Mu attack on the sterically crowded C-center was studied via a 2D scan of the C-Mu bond length and the Mu-C-CH_3 bond angle. Interestingly, we observed a competition between Mu addition to the C-center and H atom abstraction from a terminal CH_3 group to produce a diamagnetic HMu molecule. Mu atoms with trajectories in the plane of the **TPB'** ring showed an abstraction mechanism instead of addition. The signal due to diamagnetic species contributes to the large central peak but cannot be resolved as separate signals.

It is evident that the barrierless Mu addition and the proton abstraction competes with the C muoniation. Furthermore, the reaction pathway with an activation energy barrier contributes to the delayed formation of the radical. Slow formation of the radical results in spin dephasing of the muon, reducing the intensity of the observed TF-μSR signal.

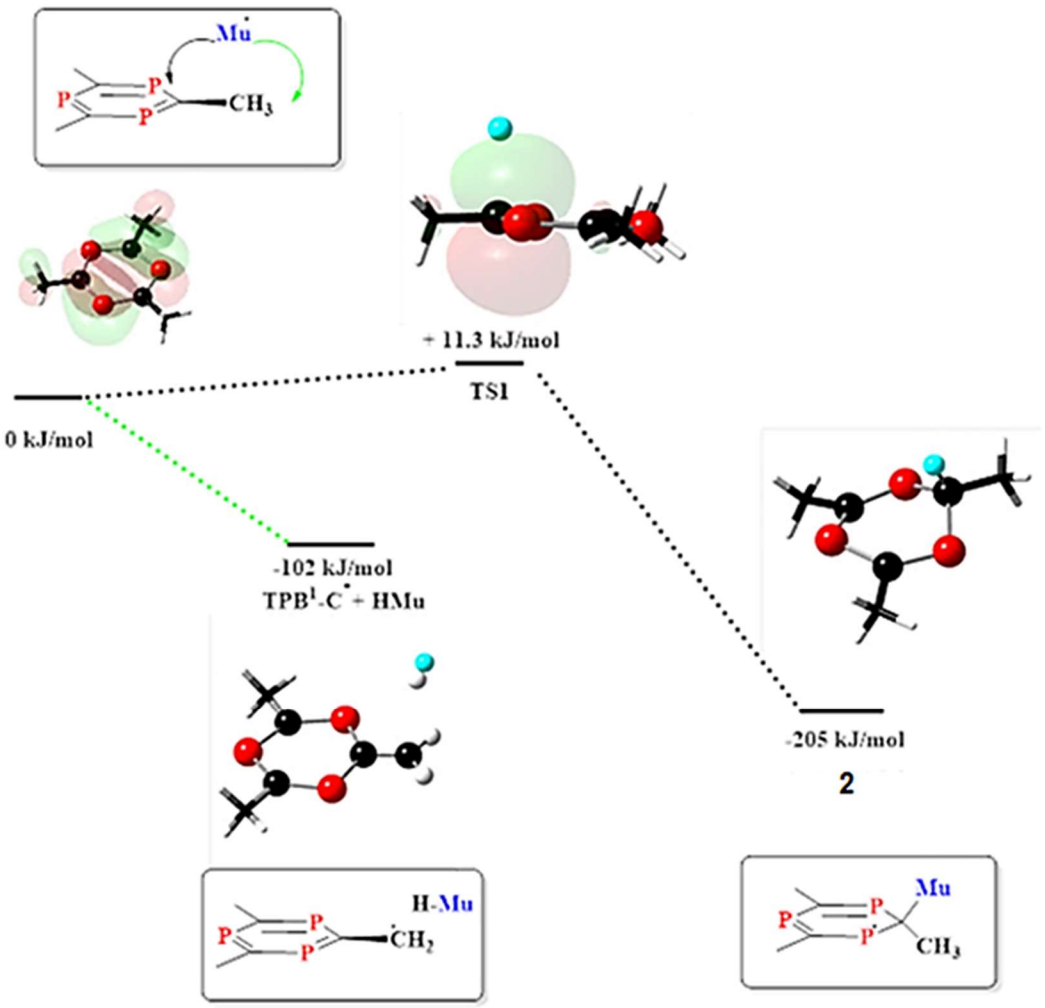

Figure 6-10: Direct H abstraction pathway (green) and the 2' formation pathway with loosely bound transition state (black).

6.3. Conclusion

In conclusion, we offer insights into the mechanism by which neutral radicals are formed from TPB, and details of their structures and dynamics. Formation of the higher energy P-muoniated radical is preferred over the lower energy C-muoniated radical due to multiple reaction pathways with barrierless transition states. However, it is possible that Mu addition to C competes with the H abstraction from terminal alkyl groups of the TPB molecule. Also, we propose that bicyclic ring formation occurs via a radical addition route.

Chapter 7.

Summary and future work

7.1. Summary

In this thesis research I have applied μSR for two reasons: To answer scientific problems that cannot easily be resolved by other techniques and to specifically characterize and study muoniated radicals formed by phospha-organic compounds. The study of phospha-organic compounds is an extension to the work of the SFUMU group on exploring muoniated radical formation from other main group compounds.

Chapter 3 details the investigation of monomers of PEEK polymer to determine the suitability of the polymer for sample cell fabrication for μSR. Multiple muoniated radicals were formed indicating the unsuitability of the PEEK for sample cell fabrication.

Chapters 4 and 5 are based on a systematic study of muoniated radical formation from phosphaalkenes. Phosphaalkene structures used for polymerization often have bulky substituent groups and the radicals formed cannot be unambiguously determined by EPR in the initiation step of the polymerization. We studied radicals formed from- the phosphaalkene mes-P=C-$(CH_3)_2$ and its alkene isomer mes-HP-C(CH_3)=CH_2. Two radical isotopologues mes(Mu)-P-Ċ$(CH_3)_2$ and mes(H)-P-Ċ-CH_2Mu(CH_3) were formed from the two compounds. The hfc of the proton (H-P) in phosphaalkane radical is comparable to the reduced muon hfc of the radical formed from phosphaalkene. This is consistent with our proposal of Mu addition to the P=C bond, forming a C-centered radical. In chapter 5 we further investigated Mu addition to the P=C bond, where we observed effects of different substituent groups on Mu addition. Effects of the electronegativity of the substituents were investigated for Mu addition to (CF_3)-Ar-P=C$(Me)_2$. In this case the ratio of Mu addition to P or C was altered by introduction of electronegative substituents. In the case of Mu addition to the compound Ad-P=CHtBu, addition resulted in selective formation of P-muoniated radicals. Most importantly the study of mes-P=CPh_2 confirmed selective addition of Mu to P to form a P-Mu radical, indicating polymerization occurs via the P-H radical.

Chapter 6 describes the study of the radical chemistry of TPB that led to the exciting discovery of a rearrangement mechanism forming secondary muoniated radicals. This complements the reaction mechanism where H_2 is cleaved by TPB via an ionic mechanism.

7.2. Future work

In terms of phosphaalkenes we have only started the systematic study of radical formation by Mu addition. From the current study it is apparent that substituents play a crucial role in controlling the radical products. Further expansion of this study to different substituent groups would give additional insight to the phosphaalkene radical polymer initiation process.

The TF-μSR signal amplitude of the **TPB-C-Mu** signal shows oscillation with time. This behavior needs further exploration. Preliminary work shows similar behavior in several other hetero-organic compounds. We propose that muoniated radical formation occurs in two pathways: The Mu atom directly reacts with the parent molecule; or the Mu^+ cation reacts with the parent molecule followed by electron acquisition from the solution to form the neutral radical. We propose further investigation of this by using compounds with polar double bonds to increase the Mu^+ selectivity for the C atom. Also, another approach is to study TPB dissolved in different solvents ranging from non-polar to polar, and observe the effect of solvents on the signal oscillation. With the nonpolar solvents the Mu^+ pathway is expected to be prominent, while with polar solvents the muonium atom pathway would be favored.

Initial studies of N containing heterocyclic compounds have been promising. The TF-μSR spectrum of muoniated radicals of triazine showed C-Mu radical formation. Organonitrogen compounds are more commercially available and have a range of applications as ligands to starting materials of polymerization. Therefore, systematic study of the radical chemistry of organonitrogen compounds would be a good complement to this work.

References

1. Nonhebel, D. C., Walton, J. C., (1974). *Free-radical chemistry: structure and mechanism*. CUP Archive.

2. American Chemical Society National Historic Chemical Landmarks. *Moses Gomberg and Organic Free Radicals.* http://www.acs.org/content/acs/en/education/whatischemistry/landmarks/freeradicals.html (accessed 11, 22, 2019).

3. Walling, C. (1986). *J. Chem. Edu.,* 63(2), 99.

4. Neta P. (1972). Reactions of hydrogen atoms in aqueous solutions. *Chem. Rev.,* 72(5), 533-543.

5. Weil, J. A., Bolton, J. R. (2007). *Electron paramagnetic resonance: elementary theory and practical applications*. Wiley.

6. Symons, M. (1978). *Chemical and biochemical aspects of electron Spin Resonance Spectroscopy*. Wiley.

7. Yaouanc, A., Delmas de Reotier, P. (2011). *Muon Spin Rotation, Relaxation and Resonance. Applications to Condensed Matter*, Oxford University Press.

8. Neddermeyer, S. H., Anderson, C. D. (1937). *Phys. Rev.*, 51, 884-886.

9. Nagamine K. (2003). *Introductory Muon Science*; Cambridge University Press, chapter 4.

10. Hughes, V. W., McColm, D. W., Ziock, K., Prepost, R. (1960). *Phys. Rev. Lett*., 5, 63-65.

11. Brodskii, A. M. (1963). *Soviet Physics JETP*, 17, 1085-1088.

12. Walker, D. C. (1983). *Muon and Muonium Chemistry*, Cambridge University Press.

13. Roduner, E., Percival, P. W., Fleming, D. G., Hochmann, J., Fischer, H. (1978). *Chem. Phys. Lett.,* 57(1), 37-40.

14. Roduner E. (1988). *The positive muon as a probe in free radical chemistry: potential and limitations of the μSR techniques.* Lecture Notes in Chemistry No. 49; Springer-Verlag.

15. Fleming D. G., Manz J., Sato K., Takayanagi T. (2014). *Angew. Chem. Int. Ed.*, *53*(50), 13706-13709.

16. Patterson, B.D. (1988). *Rev. Mod. Phys*., 60, 69-159.

17. Roduner, E., Fischer, H. (1981). *Chem. Phys*., 54, 261-276.

18. Abragam, A. (1984). *Comptes Rendus Acad. Sci. II*, 299, 95-99.

19. Kiefl, R. F., Kreitzman, S., Celio, M., Keitel, R., Luke, G.M., Brewer, J. H., Noakes, D. R., Percival, P. W., Matsuzaki, T., Nishiyama, K. (1986). *Phys. Rev. A*, 34, 681-684.

20. Heming, M., Roduner, E., Patterson, B. D., Odermatt, W., Schneider, J., Baumeler, H., Keller, H., Savic, I.M. (1986). *Chem. Phys. Lett*., 128, 100-106.

21. Kreitzman, S. R., Roduner, E. (1995). *Chem. Phys*., 192, 189-230.

22. Percival, P. W., Kiefl, R. F., Kreitzman, S. R., Garner, D. M., Cox, S. F. J., Luke, G. M., Brewer, J. H., Nishiyama, K., Venkateswaran, K. (1987). *Chem. Phys. Lett*., 133, 465-470.

23. McKenzie I. Roduner E. (2009). *Naturwissenschaften*, *96*(8), 873-887.

24. Roduner E., Strub W., Burkhard P., Hochmann J., Percival P.W., Fischer H., Ramos M., Webster B. C. (1982). *Chem. Phys.*, 67(3), 275-285.

25. Ramos M. J., Mckenna D., Webster B. C., Roduner E. (1983). *J. Chem. Soc., Faraday Trans.1,* (80), 267-274.

26. Percival, P.W., Brodovitch, J.C., Leung, S.K., Yu, D., Kiefl, R.F., Luke, G.M., Venkateswaran, K., Cox, S.F.J. (1988). *Chem. Phys*. 127(3), 137-147.

27. Yu D., Percival P. W., Brodovitch J. C., Leung S. K, Kiefl R. F., Venkateswaran K., Cox S. F. (1990). *J. Chem. Phys.*, *142*(2), 229-236.

28. McKenzie, I., Brodovitch, J. C., Ghandi, K., Kecman, S., Percival, P. W. (2003). *Physica B*, 326, 76-80.

29. McKenzie I., Brodovitch J. C., Ghandi K., McCollum B. M., Percival P. W. (2007). *J. Phys. Chem. A*, 111(42), 10625-10634.

30. McKenzie I., Brodovitch J. C., Percival P. W., Ramnial T., Clyburne J. A. (2003). *J. Am. Chem. Soc.*, 125(38), 11565-11570.

31. Arduengo A. J. (1999). *Acc. Chem. Res.*, 32(11), 913-921.

32. West R., Percival P. W. (2010). *J. Chem. Soc., Dalton Trans.,* 39, 9209-9216.

33. West R., Samedov K., Percival P. W. (2014). *Chem. Eur. J.*, 20(30), 9184-9190.

34. West R., Samedov K., Mitra A., Percival P. W., Brodovitch J. C., Langille G., Li J. (2014). *Can. J. Chem.*, 92(6), 508-513.

35. McCollum B. M., Brodovitch J. C., Clyburne J. A., Mitra A., Percival P. W., Tomasik A., West R., (2009). *Chem. Eur. J.,* 15(34), 8409-8412.

36. McCollum B. M., Brodovitch J. C., Clyburne J. A., Percival P. W., West R. (2009). *Physica B.,* 404(5-7), 940-942.

37. McCollum B. M., Abe T., Brodovitch J. C., Clyburne J. A., Iwamoto T., Kira M., West R. (2008). *Angew. Chem. Int. Ed.*, 47(50), 9772-9774.

38. Percival P. W., Brodovitch J. C., Ghandi K., McCollum B. M., McKenzie I. (2005). *J. Am. Chem. Soc.*, 127(39), 13714-13719.

39. Akiya, N.; Savage, P. E. (2002). *Chem. Rev.*, 102, 2725-2750.

40. Gates D. P. (2005). In *New Aspects in Phosphorus Chemistry V*, Springer, Berlin, Heidelberg, 107-126.

41. Bates J. I., Dugal-Tessier J., Gates D. P. (2010). *J. Chem. Soc., Dalton Trans.*, 39(13), 3151-3159.

42. Mathey, F., Nixon, J. F., Dillon, K. (1998). *Phosphorus: the carbon copy.* Wiley.

43. T. E. Gier (1961). *J. Am. Chem. Soc*., 83, 1769.

44. Townsend N. S., Green M., Russell C. A. (2012). *Organometallics.,* 31(7), 13453-13457.

45. TRIUMF: Canada's National Laboratory for Particle and Nuclear Physics http://www.triumf.ca/home/about-triumf/history (accessed Nov 15, 2019).

46. Main Cyclotron & Beam Lines, TRIUMF: Canada's National Laboratory for Particle and Nuclear Physics http://www.triumf.ca/research-program/research-facilities/main-cyclotron-beam-lines (accessed Nov 15, 2019).

47. TRIUMF Canada's Particle accelerator center. https://www.triumf.ca/pif-nif (accessed Nov 15, 2019).

48. Pifer A. E., Bowen T., Kendall K. R. (1976) *Nucl. Instrum. Meth.,* 135(1), 39-46.

49. Beveridge J. L., Reid I. D., Doornbos J., Garner D. M., Arseneau, D. J., Senba M. (1985). *Nucl. Instrum. Meth. Phys*. *Res*., 240(2), 316-322.

50. Pratt, F. L. (2000). WIMDA: *Physica B: Condensed Matt.*, 289, 710-714.

51. James, F. (1998). MINUIT – Function Minimization and Error Analysis, CERN Program Library entry D506. https://web.archive.org/web/20080526130742/ http://wwwasdoc.web.cern.ch/wwwasdoc/minuit/minmain.html (accessed Nov 15, 2019).

52. Jensen, F. (2017). *Introduction to computational chemistry*. Wiley.

53. Kohn W., Sham L., (1965). *Phys. Rev*., 140 (4A), A1133.

54. Koch W., Holthausen M. C. (2015). A Chemist's Guide to Density Functional Theory. Wiley.

55. Becke, A. D. (1993). *J. Chem. Phys*., 98(2), 1372-1377.

56. Frisch A. E., Foresman J. B. (1996). Exploring Chemistry with Electronic Structure Methods; Gaussian Inc. Pittsburgh, PA.

57. Frisch M. J., Trucks G. W., Schlegel H. B., Scuseria G. E., Robb, M. A., Cheeseman J. R., Scalmani G., Barone V., Mennucci, B., Petersson G. A., Nakatsuji H., Caricato M., Li X., Hratchian H. P., Izmaylov A. F., Bloino, J., Zheng G., Sonnenberg J. L., Hada, M., Ehara M., Toyota K., Kiefl R. F., Hasegawa J., Ishida M., Nakajima T., Honda, Y., Kitao O., Nakai H., Vreven T., Montgomery J., Peralta J. E., Ogliaro F., Bearpark M., Heyd J. J., Brothers E., Kudin K. N., Staroverov V. N., Kobayashi R., Normand, J., Raghavachari K., Rendell A., Burant, J. C., Iyengar S. S., Tomasi J., Cossi, M., Rega N., Millam J. M., Klene M., Knox J. E., Cross J. B., Bakken V., Adamo C., Jaramillo J., Gomperts R., Stratmann R. E., Yazyev O., Austin, A. J., Cammi R., Pomelli C., Ochterski J. W., Martin R. L., Morokuma K., Zakrzewski V. G., Voth G. A., Salvador P., Dannenberg J. J., Dapprich S., Daniels A. D., Farkas Ö., Foresman J. B., Ortiz J. V., Cioslowski J., Fox D. J., Gaussian 09, Revision D.01; Gaussian Inc.: Wallingford, CT, 2009.

58. Barone V. (1996.). *Chem. Phys. Lett.,* 262(3-4), 201-206.

59. Barone V. (1995). *Theoret. Chim. Acta.*, 91(3-4).

60. Johnson C, Cottrell S. P., Ghandi K, Fleming D G (2005) *J. Phys. B: At. Mol. Opt. Phys.* 38 119.

61. Patel P., Hull T. R., McCabe R. W., Flath D., Grasmeder J., Percy M. (2010). *Polymer Degradation and Stability,* 95(5), 709-718.

62. Chandrasena L., McKenzie I., Brodovitch J.-C., Mozafari M., Cottrell S.P., Percival P.W. (2014). *J. Phys. Conf. Ser.*, 551, 012038.

63. CODATA Value: muon magnetic moment to nuclear magneton ratio http://physics.nist.gov/cgi-bin/cuu/Value?mumumsmun (accessed May 5, 2016).

64. Mathey, F. (2003). *Angew. Chem. Int. Ed*. 42, 1578-1604.

65. Bates J. I., Dugal-Tessier J., Gates D. P. (2010). *Dalton Trans.,* 39(13), 3151-3159.

66. Simpson M. C., Protasiewicz J. D. (2013). *Pure Appl. Chem.*, 85(4), 801-815.

67. Tsang C. W., Yam M., Gates D. P. (2003). *J. Am. Chem. Soc.*, 125(6), 1480-1481.

68. Tsang C. W., Baharloo B., Riendl D., Yam M., Gates D. P. (2004). *Angew. Chem. Int. Ed.,* 116(42), 5682-5685.

69. Siu, P.W., Serin, S.C., Krummenacher, I., Hey, T.W., Gates, D.P. (2013). *Angew. Chem. Int. Ed*. 52, 6967-6970.

70. Rawe, B.W., Priegert, A.M., Wang, S., Schiller, C., Gerke, S., Gates, D.P. (2018). *Macromolecules* 51, 2621-2629.

71. Percival P. W., McCollum B. M., Brodovitch, J. C., Driess M., Mitra A., Mozafari M., West R., Yun X., Yao S. (2012). *Organometallics*, *31*(7), 2709-2714.

72. Percival P. W., Brodovitch J. C., Mozafari M., Mitra A., West R., Ghadwal R. S., Askar R., Roesky H. W. (2011). *Chem. Eur. J.*, *17*(43), 11970-11973.

73. Mitra, A., Brodovitch, J.-C., Krempner, C., Percival, P.W., Vyas, P., West, R. (2010). *Angew. Chem. Int. Ed.* 49, 2893-2895.

74. Ito, S., Ueta, Y., Koshino, K., Kojima, K.M., McKenzie, I., Mikami, K. (2018). Angew. Chem. Int. Ed. 57, 8608-8613.

75. Armstrong, A., Chivers, T., Boeré, R.T. (2005). In *Modern Aspects of Main Group Chemistry*. ACS Symposium Series Vol. 917 (Eds.: Lattman M., Kemp R. A.), American Chemical Society, pp. 66-80.

76. Fullam B. W., Mishra S. P., Symons M. C. R. (1974). *J. Chem. Soc., Dalton Trans.,* 45, 2145-2148.

77. Gynane M. J. S., Hudson A., Lappert M. F., Power P. P., Goldwhite H. (1980). *J. Chem. Soc., Dalton Trans.,* 2428-2433.

78. Russu A. N., Gamba A., Cariati F., Bart J., Symons M. (1982). *Spectrochim. Acta.,* 38(6), 637-639.

79. Hinchley, S. L., Morrison C. A., Rankin D. W. H, Macdonald C. L. B, Wiacek R. J, Cowley A. H., Lappert M. F., Gundersen G., Clyburne J. A. C., Power P. P. (2001). *Chem. Commun.* 123(37), 9045-9053.

80. Armstrong A., Chivers T., Parvez M., Boere R. T. (2004). *Angew. Chem. Int. Ed.*, 43(4), 502-505.

81. Ndiaye B., Bhat S., Jouaiti A., Berclaz T., Bernardinelli G., Geoffroy M. (2006). *J. Phys. Chem. A.*, 110(31), 9736-9742.

82. Back O., Donnadieu B., Hopffgarten M., Klein S., Tonner R. G., Frenking, G., Bertrand G. (2011). *Chem. Sci.*, 2(5), 858-861.

83. Giffin N. A., Hendsbee A. D., Masuda J. D. (2016). *Dalton Trans*., 45, 12636-12639.

84. Fischbach U., Trincado M., Grützmacher H. (2017). *Dalton Trans*., 46, 3443-3448.

85. Wang W., Xu C.-Q., Fang Y., Zhao Y., Li J., Wang X. (2018) *Angew. Chem. Int. Ed.*, 57(30), 9419-9424.

86. Tan, G., Li, J., Zhang, L., Chen, C., Zhao, Y., Wang, X., Song, Y., Zhang, Y.-Q., Driess, M. (2017). *Angew. Chem. Int. Ed.*, 56, 12741-12745.

87. Tan, G., Li, S., Chen, S., Sui, Y., Zhao, Y., Wang, X. (2016). *J. Am. Chem. Soc*. 138, 6735-6738.

88. Pan X., Wang X., Zhang Z., Wang X. (2015). Dalton Trans., 44, 15099-15102.

89. Pan X., Wang X., Zhao Y., Sui Y., Wang X. (2014). *J. Am. Chem. Soc.,* 136(28), 9834-9837.

90. Rosa P., Gouverd C., Bernardinelli G., Berclaz T., Geoffroy M. (2003). *J. Phys. Chem. A*, 107(24), 4883-4892.

91. Badri A., Jouaiti A., Geoffroy M. (1999). *Magn. Reson. Chem.,* 37(10), 735-742.

92. Jouaiti A. A., Badri A., Geoffroy M., Bernardinelli G. (1997). *Organomet. Chem*., 529(1-2), 143-149.

93. Bhat S. N., Berclaz T., Jouaiti A., Geoffroy M. (1994), *Helv. Chim. Acta.* 77(1), 372-382.

94. Bhat S. N., Berciaz T., Geoffroy M., Jouaiti A. (1995). *J. Phys. Chem.,* 99(43), 15864-15869.

95. Mercier F., Hugel-Le Goff C., Mathey F. (1989), *Tetrahedron Lett*., 30, 2397-2398.

96. Roduner E. (2005), in *Isotope Effects in Chemistry and Biology* (Eds.: Kohen A., Limbach H.-H.), CRC Press, pp. 433-450.

97. Roduner E. (1986). *Radiat. Phys. Chem*., 28, 75-84.

98. Baban, J.A., Cooksey, C.J., Roberts, B.P. (1979). *J. Chem. Soc. Perkin Trans. 2*, 781-787.

99. Begum, A., Lyons, A.R., Symons, M.C.R. (1971). *J. Chem. Soc. A*, 2388-2392.

100. Misra, G. S. (1993). *Introductory polymer chemistry*. New Age International.

101. Fleming D. G., Bridges M. D., Arseneau D. J., Chen Y. K., Wang Y. A. (2011). *J. Phys. Chem. A*, *115*(13), 2778-2793.

102. Fleming D. G., Arseneau D. J., Bridge M. D., Che Y. K., Wang Y. A. (2013). *J. Phys. Chem. C*, 117(32), 16523-16539.

103. Chandrasena L., Samedov K., McKenzie I., Mozafari M., West R., Gates D. P., Percival P. W. (2019). *Angew. Chem. Int. Ed.,* 131(1), 303-307.

104. Wright V. A., Patrick B. O., Schneider C., Gates D. P. (2006). *J. Am. Chem. Soc.*, 128(27), 8836-8844.

105. Kobayashi T., Seki K., Tanaka T., Takayanagi T. (2011). *Comput. Theo. Chem.*, 963(2-3), 256-262.

106. Macrae R. M., Carmichael I. (2003). *Physica B*, 326(1-4), 81-84.

107. Noonan K. J., Gillon B. H., Cappello V., Gates D. P. (2008). *J. Am. Chem. Soc.*, 130(39), 12876-12877.

108. Goli M., Shahbazian S. (2018). *Phys. Chem. Chem. Phys.,* 24, 10140-10152.

109. Goli M., Shahbazian S. (2014). *Phys. Chem. Chem. Phys.*, 16(14), 6602-6613.

110. Yamada K, Kawashima Y., Tachikawa M. (2014*). J. Chem. Theory Comput.,* 10(5), 2005-2015.

111. Le Floch P. (2006). *Coord. Chem. Rev.*, 250(5-6), 627-6Pfitzner A. (2006). *Angew. Chem. Int. Ed.*, 45(5), 699-700.

112. Pfitzner, A. (2006). *Angew. Chem. Int. Ed*., 45(5), 699-700.

113. Barron A. R., Cowley A. H. (1987). *Angew. Chem. Int*. *Ed.*, 26(9) 907-908.

114. Tabellion F., Nachbauer A., Leininger S., Peters C., Preuss F., Regitz M. (1998). *Angew. Chem. Int. Ed.*, 37(9), 1233-1235.

115. Gleiter, R., Lange, H., Binger, P., Stannek, J., Krüger, C., Bruckmann, J., Zenneck, U., Kummer, S. (1998). *Eur. J. Inorg. Chem.,*1619-1621.

116. Speight J. G. (2016). *Introduction to enhanced recovery methods for heavy oil and tar sands.* Gulf Professional Publishing.

117. Longobardi L. E., Russell C. A., Green M., Townsend N. S., Wang K., Holmes A. J., Duckett S. J., McGrady J. E., Stephan D. W. (2014). *J. Am. Chem. Soc*., 136(38), 13453-13457.

118. Zhang Y., Tham F. S., Nixon J. F., Taylor C., Green J. C., Reed, C. A. (2008). *Angew. Chem. Int. Ed.,* 47(20), 3801-3804.

119. Zielinski F., Tognetti V., Joubert L., (2013). *J. Mol. Model.*, 19(9), 4049-4058.

120. Gerson F., Huber W. (2003). *Electron spin resonance spectroscopy of organic radicals.* John Wiley & Sons.

Appendix

Temperature-dependent hyperfine constants for the muoniated methyl group.

Temperature dependence is typical for a muoniated methyl group attached to a radical center, e.g. in the β-muoniated ethyl and tert-butyl radicals. It arises from averaging over the vibrational mode corresponding to internal rotation of the methyl about the carbon–carbon bond. At low temperature the preferred conformation has maximum overlap between Cβ–Mu and the p_z-orbital containing the unpaired electron on the α-carbon. Since β-hyperfine constants depend on dihedral angle,

$$A_\beta = A_0 + B\cos^2\phi$$

the muon hfc falls with temperature as a larger range of angles is accessed. The line through the points in figure A1 is the best fit of the empirical equation

$$A_\mu = A_{T=0}\left[1 - \exp\left(-E_a / RT\right)\right]$$

and gives an approximate barrier height for rotation of E_a = 760 J mol^{-1}

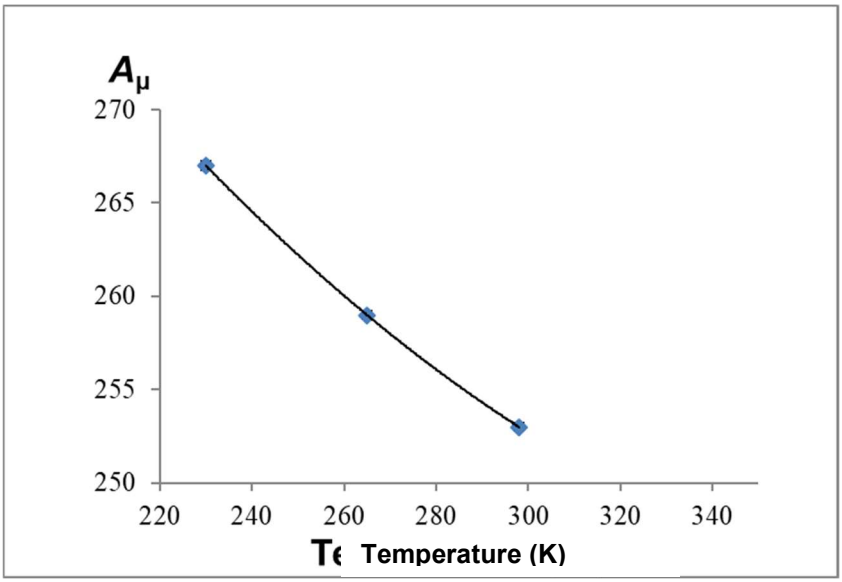

Figure A-1: Temperature dependence of the muon hyperfine constant for the radical formed from 4b, subsequently identified as 4b-CH_2-Mu.

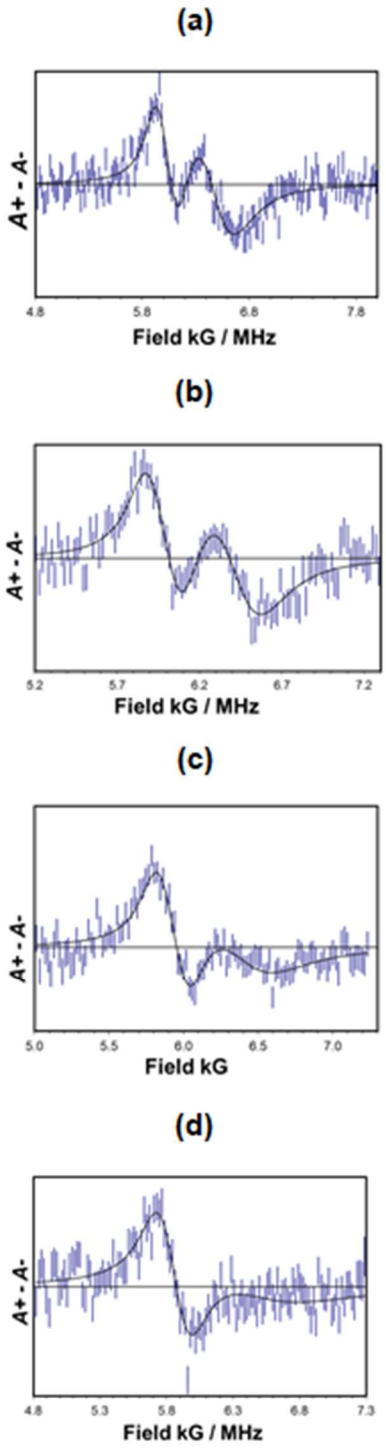

Figure A-2: **Temperature variation of the phosphorus resonances in the muon avoided level-crossing spectrum of the radicals formed from 4a in tetrahydrofuran at temperatures (top to bottom) 320 K, 299 K, 265 K and 230 K.**